Durham E-Theses

Investigating magnetisation dynamics in magnetic thin films and micro-structures

JAISWAL, SAMRIDH

How to cite:

Use policy

Investigating magnetisation dynamics in magnetic thin films and micro-structures

Samridh Jaiswal

A thesis submitted in the fulfilment of the requirements for the degree of

Master of Science by Research

University of Durham

2016

Table of Contents:

Abstract

Data storage is the fulcrum on which technology advances. As the rate of consumption of data increases there is growing demand from the storage industry for faster, more efficient storage solutions which is capable of storing more information per unit area. Non-volatile magnetic memory based on spin-electronics is one of the key proponents for addressing this demand. In order to develop such a memory it is necessary to attain a better understanding of the magnetic properties on which this is based.

This thesis aims to develop a tool to study the magnetisation dynamics of the free layer in a Pseudo Spin-Valve (PSV) of the form Co/Cu/NiFe utilising both the Giant Magneto-Resistance (GMR) and the Anisotropic Magneto-Resistance (AMR) effects. The key difference in the resistance responses of each of these effects is exploited here to showcase a proof of concept device which can be used as another method to aid in the study of magnetisation dynamics. GMR's resistance response is dependent on the relative orientations of magnetisation between the free layer and the pinned layer. The AMR's resistance response however, depends on the relative orientations of the magnetisation and the current direction. However, the resistance response of AMR is independent of magnetisation parallel or anti-parallel to current. This independence and the dependence of GMR on the relative magnetisations in each layer are used in combination to study the evolution of the magnetisation in a free layer PSV.

The magneto-resistance of the Co/Cu/NiFe spin-valve was measured in as deposited samples and samples deposited in the presence of an in-plane field. The magneto-resistance was compared to a PSV with an insertion of a Co layer at the Cu/NiFe interface. An L-shaped device was designed and patterned which could be used to study the magnetisation reversal in the NiFe free layer. This was done by tuning the RKKY coupling between the Co and NiFe, shape anisotropy of the patterned micro-wire and the Anisotropic Magneto-Resistance ratio of the NiFe in the pseudo-spin-valve.

Acknowledgements

|Chapter 1

Introduction

1.1Introduction and background

Over the past few decades there has been immense interest in developing new devices using novel materials and designs to improve magnetic data storage [1]. The non-volatile nature of such memory devices is a clear advantage over traditional storage media [2]. In addition to conventional hard disk storage various new kinds of spintronics based magnetic memories have been proposed [3] and understanding the underlying physics is important for such applications. There are four main factors driving research namely, 1) ultrafast switching time - speed 2) low switching energy - relating to efficiency 3) high endurance - relating to reliability and 4) smaller dimensions relating to increasing data densities. With the development and implementation of MRAM, STT-MRAM [4] and SOT-MRAM concepts [5] there is a drive to develop tools to aid in the understanding of the magnetisation dynamics which will be applicable in these magnetic based memories. The research presented in this work aims to develop a device structure which may act as a tool to study magnetisation changes in micro and nanoscale magnetic structures that will ultimately aid the development of the next generation magnetic storage and technology.

To understand the motivation behind this study it is crucial to understand the importance of why research in the field of spintronics is important. The unique property which gives an advantage to spintronics lies in the fact that unlike electronics where only charge of an electron is exploited in conventional electronic processes both in memory and logic operations, in spintronics the spin of the electron is also harnessed and used to store information or process logic operations [6]. Hard disk read heads and applications such as the magnetic field sensor for sensing rotations invented by E. Shoemaker [7] serve as examples of the capability of spintronic based devices. Due to the rapid development of novel magnetic memories and spin logic devices [8] there is a need to engineer structures which are capable of studying fast magnetisation reversals dynamically in magnetic structures.

There already exist various techniques to study magnetisation changes [9]. Although they may be complementary they do not meet the requirements necessary to study modern fast magnetic memory. In order to understand the motivation here one must understand the existing techniques and their short comings. To aid with the understanding some existing techniques to study magnetisation dynamics are therefore described briefly below.

Magnetic Force Microscopy

This is a surface scanning technique which is a modification of Atomic Force Microscopy. It is based on the magnetic dipole-dipole interactions between a magnetic tip and the sample surface. In the case that the sample being investigated has an extremely low coercive field, the tip can influence the magnetic state of the sample requiring a more intensive analysis to extract meaningful information. It is possible to obtain a resolution of 30 nm using this technique as shown by a comparative study [10]. However the drawback of this technique is that due to the rastering nature of this technique it is a slow technique depending on the quality of the image needed and the number of acquisitions. It can take of the order of a few minutes to obtain an image. It is also not possible to study dynamic

changes in the magnetisation; magnetisation changes via a pulsed magnetic field or current can be recorded after the application of the pulse but not during the excitation pulse. Shown in Fig 1.1 is a typical magnetic force microscopy image for a vortex domain wall in a NiFe ring.
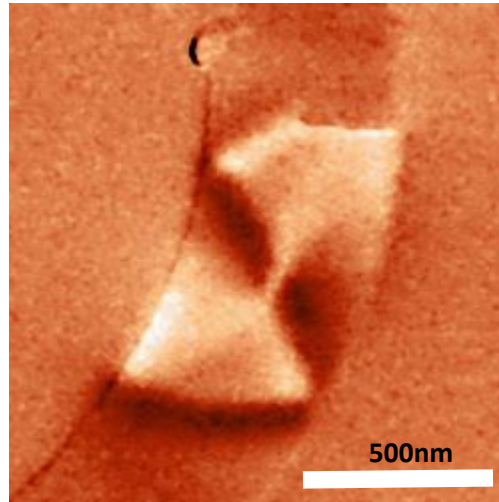
500nm

Figure1.1: An MFM image of a vortex head to head domain wall in a 15 nm thick Permalloy stripe of width 500 nm [11].

Lorentz Force Microscopy

This is a powerful static technique that also provides information of the structural as well as the magnetic configuration of the materials being studied [12]. An example is shown in Fig 1.2. It is well known that many applicable properties of magnetic materials depend on the local microstructure and composition of the material. Thus being able to provide both structural and magnetic configuration of the materials being studied is beneficial. One clear advantage is that in the TEM (Transmission Electron Microscopy) mode, one can apply in-situ magnetic field and image the domain configuration during the application of the field [13]. However a limitation of this technique is the time resolution [14]. Due to the limitations of the image capture short exposure images do not have enough electron dose for acquiring temporally resolved information about the dynamic behaviour of structures [15]. The temporal resolution therefore limits the spatial resolution of the Lorentz TEM. The shortest time interval that can be achieved is of the order of few ms - 1s which is far greater than what is required to be in dynamic range for magnetisation [15].

The Lorentz TEM works on the principle that an electron travelling through a region of uniform magnetisation experiences a Lorentz force and is thereby deflected. It can be operated in two modes, the Fresnel and the Foucault mode with Differential Phase contrast (DPC). The group of S. McVitie from the University of Glasgow are experts in the technique of studying magnetic structure using the Lorentz LTEM [16]. For a more detailed overview the reader is referred to [17]. The Fresnel mode allows one to image domain walls and the ripples in magnetisation. This is done by under focussing or over focussing. Depending on the number of electrons extracted, white or dark contrast represents the presence or absence of a domain wall. In the Foucault mode an aperture is introduced in the back focal plane of the Lorentz lens in order to intercept electrons which have passed through one set of magnetic domains [13]. The aperture is then moved or the incident beam path is tilted slightly and a series of images are obtained. Each magnetic component Bx and By in the two orthogonal directions are computed and a vector map of the remnant state of the magnetic domain configuration is obtained. Shown in Fig 1.2 is a Lorentz TEM image taken of an in plane magnetised 40 nm thick Permalloy wire 1000 x 200 nm^2
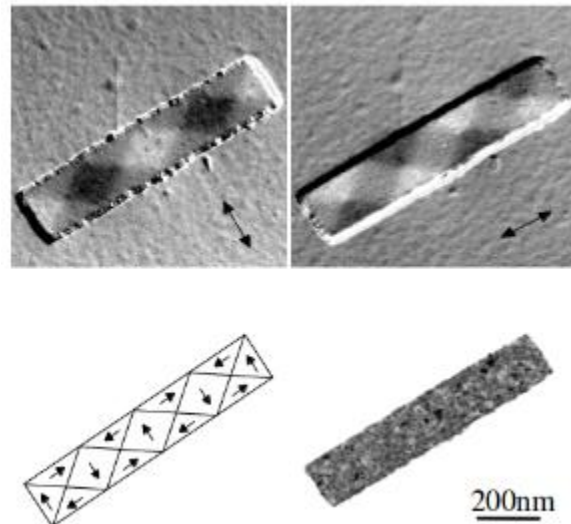
Figure1.2: LTEM image of a Permalloy nanowire 40 nm thick. The difference in the grey contrast shows the magnetic orientation of the wire [18].

Kerr Microscopy

This technique is a relatively easier technique with respect to the instrumentation which comprises of an optical microscope with MOKE integration. The technique involves using the Kerr effect [19], which states that the change in magnetisation is proportional to the relative change in the plane of polarisation of the incident light. This Kerr angle/rotation is detected as a change in the photo-induced current on a receiving diode and the sample is imaged using white light. A Kerr Microscopy image of a magnetic bubble for an unstructured perpendicularly magnetized thin film is shown in Fig 1.3.
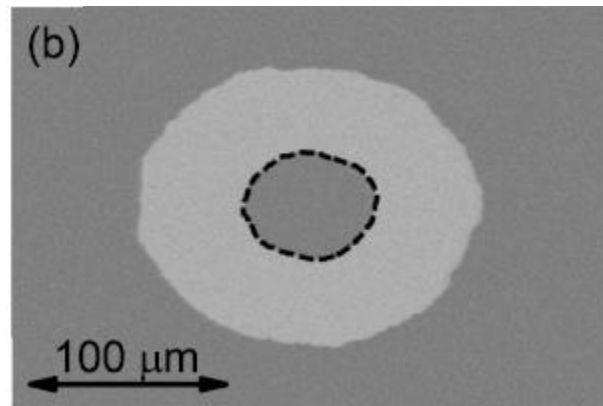
Figure1.3: Kerr Microscopy image taken in differential for contrast enhancement of a magnetic bubble in perpendicularly magnetized multilayer stack. White LED is used as the source. Grey contrast is magnetic contrast [22].

One assumption of this technique is that the Kerr rotation is independent of incident wavelength [20]. Details on Kerr magnetometry can be found in section 2.7 of this thesis. Imaging structures with widths down to 300 nm is possible. Smaller width wires have been measured. However, studying magnetisation switching at such resolution is limited by thermal instabilities which drastically reduces the Kerr contrast. Kerr Microscopy has been the method of choice for multiple research groups studying current and field-induced domain wall motion globally [21][22][23][24]. It uses wide field imaging to sample large areas in a continuous thin film and can be operated in a

differential mode which continuously subtracts the live image with an earlier acquired background image. This along with multiple image acquisitions allows for digitally enhancing the contrast of the domain structures. It is possible to study quasi static domain wall motion by current and field injection in magnetic nanowires [25], however, dynamic measurements are limited by the stroboscopic sources which may be attached to the Kerr microscope. Time resolution of a Kerr microscope limited by stroboscopic techniques available. Scanning Kerr Microscopes have been designed to operate in the femto-second regime using Ti:sapphire pump-probe lasers [26][27]. Another advantage of Kerr microscopy is that it is a non-invasive technique and the observation of magnetic structures does not influence the magnetisation of the sample. This could be an issue with the MFM imaging tip where the tip might cause magnetisation reversal during the measurement. A drawback of the MOKE effect is its probing depth. Due to the attenuation of the laser within the material the MOKE technique is only sensitive up to a certain thickness of magnetic materials. There exists a critical probing depth, the thickness at which the laser intensity decreases to 1/e of its initial value. This is called the skin depth of a material and is discussed further in section 2.7.3.

XMCD PEEM

X-ray Magnetic Circular Dichroism (XMCD) with Photoemission Electron Microscopy (PEEM) is a very versatile technique which can be used to obtain absorption spectra [28] as well as for imagining domain wall motion [29] (see Fig 1.4). X-ray Magnetic Linear Dichroism (XMLD) PEEM has also been used to observe antiferromagnetic domains in NiO [30] and LFO [31] epitaxial thin films. Initially UV light was used in the PEEM microscopes. It is used to study soft magnetic materials. XMCD is the difference in the magnetic signal obtained in the absorptions of left and right circularly polarised X-ray light. The differently absorbed X-ray light by a sample provides the magnetic contrast. Due to the high energy levels of X-rays needed to probe the electronic transitions, this technique is performed at synchrotron X-ray facilities [32]. By tuning the energy

level to the X-ray absorption edge which is characteristic to each element, it is possible to be sensitive to magnetic contrast of a specific element and study its change in magnetisation thereby providing chemical contrast. This is particularly useful when studying multi-layered material stacks consisting of different ferromagnetic materials. L_3 Absorption edges of Fe, Ni and Co are within the soft X-ray regime. It is possible to do Time Resolved PEEM [33] which involves measuring repeatable dynamics of a system using a pump pulse to start the experiment; a laser pulse, in the picosecond regime for example and probing pulse determined by the X-ray beamline. Time resolved PEEM is a relatively new technique with first measurements done in 2003 [34] [35] of vortices with flux closure magnetic patterns [36][37] and domain wall propagation [38]. Time Resolved PEEM is performed in the pump-probe mode and therefore is limited by the temporal resolution of the length of the X-ray bunches as the system is excited by magnetic pulses which are synchronised to the synchrotron X-ray pulses [38] [34] which are between 50-100 picoseconds [39]. A drawback of XMCD PEEM is the technique is time consuming in terms of adjustments required to obtain the desired resolution. Depending on the alignment there is some tilt in the sample plane which drastically reduces the theoretical resolution of the PEEM. Image acquisition is also time consuming depending on the size and the facility it can take a few minutes for the undulators at the beamline to change the polarisation and provide XMCD contrast. Also, since this technique is a very surface sensitive technique, UHV conditions ($>10^{-10}$ mbar) are required to image along with a very large potential difference to extract the secondary electrons generated by the incident x-rays on the sample. Therefore, it is crucial to have an extremely clean surface as there is usually only a few millimetres gap between the sample and the 20KeV imaging lens. An advantage of the PEEM over STXM (Scanning Transmission X-ray Microscopy another beamline microscopy technique) is that it is possible to use relatively cheap oxidized silicon substrates rather than the more delicate and expensive SiN membranes used in transmission microscopy.
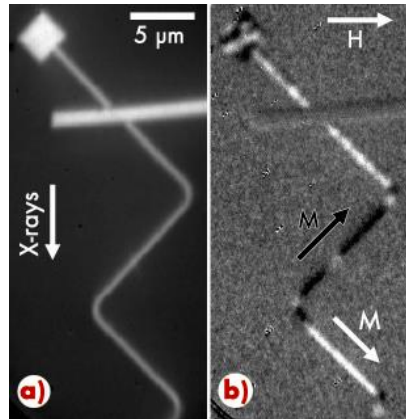
Figure1.4: (a)Topographic and (b)magnetic XMCD PEEM image of a 400 nm wide FeNi(5 nm)/Cu(8 nm)/Co(7 nm)/CoO(3 nm) spin valve taken at the Ni L_3 edge. The sample is magnetised with a static in plane field as indicated [29].

Fast domain wall motion has been imaged in a spin valve by S. Pizzini *et al.* using XMCD PEEM. This is shown in Fig 1.4 . PEEM is a surface sensitive technique, even though the X-rays penetrate deep into the sample as the electrons are extracted only from the top 3-5 nm. This requires capped samples to be etched *in-situ*. Often samples are grown in a growth chamber connected to the PEEM setup to keep the sample in UHV. Due to the X-rays coming at glancing angles (16 or 18 degrees) to the sample surface, materials with magnetisation lying spontaneously out of plane are difficult to study as only sine of the total signal would be observable, which leads to poor contrast of the magnetisation. However this depends on the magnetic material under investigation as the XMCD contrast is different for certain FM materials as compared to others.

1.2 Aim of the Thesis

As discussed there is a need for a magnetic structure/tool which can enable the study of fast magnetisation changes in a magnetic system. Thus the aim of this thesis is to describe the recent work which was to develop a generic scheme which uses Giant Magneto-Resistance (GMR) to study magnetisation processes of a free layer for which the design can be changed in line with research interests. By utilising the magnetic response to current of both the phenomenon Anisotropic Magneto-Resistance (AMR) and GMR a device was conceptualised which can ultimately be used as a handle to investigate magnetisation dynamics which is of crucial importance in the development of next generation magnetic storage. By its nature this work was time limited but its concept has been demonstrated here.

1.3 Thesis outline

The work undertaken towards this challenge is described in the following chapters. Chapter 2 begins with the necessary physical details that are required to understand the experimental results in the chapters that follow. It introduces key concepts of domain wall formation and the energy costs associated with its formation. Anisotropy energies which lead to a given magnetic state of a material are discussed. The theory of Anisotropic Magneto-Resistance and the Giant Magneto-Resistance are outlined along with the process of spin-dependent scattering. A general overview of the conduction mechanisms is included to aid this understanding. This chapter also discusses the physical principles involved in the different experimental methods used in this work. These include, the sample growth and fabrication methods, X-Ray reflectivity for structural analysis and Magneto-Optical Kerr Effect (MOKE) and Magneto-Resistance measurements for magnetic and transport measurements.

Chapter 3 follows from the principles discussed in the previous chapters and details the practicalities of the experimental techniques used. The experimental setup of the sample fabrication is discussed. The MOKE magnetometry, experimental methods, Current In-Plane Transport (CIPT) measurements as well as structural characterisation methods are discussed.

The structural, magnetic and transport results of the measurements are shown and discussed in chapter 4. The investigative results of the MOKE magnetometry on thin films and microwires consisting of the Pseudo Spin-Valve showing the switching of the free layer and the pseudo pinned layer as well as the coercivity and magnetisation reversal of the film are presented in chapter 4. The structural characterisation of the films used along with the Magneto-Resistance data to assist with its interpretation is also discussed within this chapter.

Chapter 5 brings together the concepts developed in chapter 2, the investigative techniques discussed in chapter 3 and the discussion of results and interpretation from chapter 4. The thesis concludes with the summary of key results obtained during this investigation and suggests further work which can be done in the field studied, beyond the limits of this MSc. Investigation.

Chapter 1- References

[1] Wolf,S.A., '*The promice of nanomagnetics and Spintronics for future Logic and Universal Memory*', Proceedings of the IEEE, **98**, (2010) 12 pp2155-2168

[2] Mittal, S., *et al*, '*A Survey of Software Techniques for Using Non-Volatile Memories for Storage and Main Memory Systems in Parallel and Distributed Systems*' IEEE Transactions, **PP**, (2015), 99

[3] Parkin,S.S.P., *et al*, '*Magnetic Domain-Wall Racetrack Memory*', Science **320**, (2008), 190

[4] Dorrance, William., Richard., (2011) '*Modelling and Design of STT-MRAMs*', PhD Thesis, University of California Los Angeles

[5] Weisheng, Z., Prenat, G., '*Spintronics-based Computing*'-'*Beyond STT-MRAM, Spin Orbit Torque RAM SOT-MRAM for High Speed and High Reliability Applications*' Prenat., G. *et al.* Ch.4, Springer, Switzerland(2015)

[6] Allwood, D. A., *et al.*, '*Magnetic domain-wall logic*', Science **309** (2005), 1688–1692

[7] Shoemaker, E., '*Magnetic field sensor for sensing rotation of an object*', U.S. Patent 9182456 B2

[8] Behin-Aein, B., *et al.,* '*Proposal for an all-spin logic device with built-in memory*', Nature Nanotechnology, **5**, (2010), 266-270

[9] Keatley, P.S., *et al.*, '*Ultrafast magnetization dynamics of spintronic nanostructures*', Philosophical Transactions of the Royal Society A: Mathematical, Physical and engineering Sciences, **369**, (2011), 3115-3135

[10] Abelmann, L., '*Comparing the resolution of magnetic force microscopes using the CAMST reference samples*', Journal of Magnetism and Magnetic Materials, **190**, (1998) p135–147

[11] http://neel.cnrs.fr/spip.php?article3289&lang=fr Accessed on 4th February 2016

[12] Hopster, H., Oepen, H.,P., '*Magnetic microscopy of nanostructures*', Springer, Germany (2005)

[13] Masseboeuf, A., '*The use of Lorentz microscopy for the determination of magnetic reversal mechanism of exchange-biased Co30Fe70/NiMn bilayer*', Journal of Magnetism and Magnetic Materials, **321**, (2009), 3080-3083

[14] http://magnetism.eu/esm/2013/slides/heyderman-slides.pdf Accessed on 4th Febreuary 2016

[15]http://www.gla.ac.uk/schools/physics/research/groups/mcmp/researchareas/nanomagnetics/ Accessed 4th February 2016

[16] Benitez, M.J., *et al.*, '*Magnetic Microscopy and topological stability of homochiral Néel domain walls in a Pt/Co/AlO$_x$ trilayer*', Nature Communications, **6**, (2015), 8957

[17] Ngo, Duc-The (2010) '*Lorentz TEM characterisation of magnetic and physical structure of nanostructure magnetic thin films*' PhD thesis, University of Glasgow

[18]http://www.gla.ac.uk/schools/physics/research/groups/mcmp/researchareas/nanomagnetics/ Accessed on 4th February 2016

[19] Kerr, J., '*On rotation of the plane of polarisation by reflection from the pole of a magnet*' Philosophical Magazine 3 (1877) 321-343

[20] Katayama, T., '*Wavelength Dependence of Magneto-Optical Kerr Rotation in Co/Cu, Fe/Cu, Co/Au and Fe/Au Compositionally Modulated Multilayered Films*' Journal of the Physical Society of Japan, **55**, 1986, 2539-2542

[21] Emori, S., *et al.*, '*Current-driven dynamics of chiral ferromagnetic domain walls*', Nature materials, **12**, (2013), 3675

[22] Hrabec, A., *et al.,* '*Measuring and tailoring the Dzyaloshinskii-Moriya interaction in perpendicularly magnetized thin films*', Physical Review B, **90**, (2014), 020402R

[23] Lo Conte, R., *et al.,* '*Role of B diffusion in the interfacial Dzyaloshinskii-Moriya interaction in $Ta/Co_{20}Fe_{60}B_{20}/MgO$ nanowires*', Physical Review B, **91**,(2015), 014433

[24] Ryu, S.K., *et al.*,'*Chiral spin torque at magnetic domain walls*' Nature Nanotechnology, **8**, (2013), 527

[25] Lo Conte, R., *et al.,* 'Spin-orbit torque-driven magnetization switching and thermal effects studied in TaCoFeB/MgO', Applied Physics Letters, **105**, (2014), 122404

[26]http://www-brs.ub.ruhr-uni-bochum.de/netahtml/HSS/Diss/LiJie/diss.pdf   Accessed   on   4th February 2016

[27] http://www.ncbi.nlm.nih.gov/pubmed/19655952 Accessed on 4th February 2016

[28] http://pubs.acs.org/doi/pdf/10.1021/cr9900681 Accessed on 4th February 2016

[29] Pizzini, S., *et al.*, '*High Domain Wall Velocity at Zero Magnetic Field Induced by Low Current Densities in Spin Valve Nanostripes*'Applied Physics Express, 2, (2009), 2

[30] Stöhr, J., *et al.,* '*Images of the Antiferromagnetic Structure of a NiO(100) Surface by Means of X-Ray Magnetic Linear Dichroism Spectromicroscopy*' Physical Review. Letters, **83**, (1999), 1862

[31] Scholl, A., '*Observation of Antiferromagnetic Domains in Epitaxial Thin Films*', *Science, 287, (2000), 5455*

[34] Vogel,J., *et al.*, '*Time-resolved magnetic domain imaging by x-ray photoemission electron microscopy*', Applied Physics Letters, **82**, (2003), 2299

[35] Krasyuk, A., '*Time-resolved photoemission microscopy*', Applied Physics A: Material Science and Processing, **76**, (2003), 863

[36] Schneider, C.M., *et al.*, '*Incoherent magnetization rotation observed in subnanosecond time-resolving x-ray photoemission electron microscopy*', Applied Physical Letters, **85**, (2004), 2562

[37] S.-B. Choe, S-B., *et al.*, '*Vortex Core-Driven Magnetisation Dynamics*', Science, **304**, (2004), 420

[38] Fukumoto, K., *et al.*, '*Dynamics of Magnetic Domain Wall Motion after Nucleation: Dependence on the Wall Energy*' Physical Review Letters, **96**, (2006), 097204

[39] http://neel.cnrs.fr/spip.php?article1008&lang=fr accessed on February 2016

|Chapter 2

Domain energetics, electrical conduction processes and investigative techniques

2.1 Introduction

This chapter introduces the basic principles behind domain structure formation, the formation of domain walls and the energies associated with domain nucleation and propagation. The physical principles governing Giant Magneto-Resistance and Anisotropic Magneto-Resistance are discussed. This is followed by a brief overview of the physics underpinning the deposition technique and the processes of lithography used to produce the materials for this study. The physical basis required to understand the structural characterisation, by X-ray reflectivity as well as the MOKE magnetometry is also discussed within this chapter.

2.2 Domain formation, anisotropies and energies

Any physical system over a given period of time changes its configuration until it achieves the state of lowest energy. For magnetic materials domains form in order to reduce the overall magnetic energy of the system. Magnetic domains exist in both ferromagnetic and antiferromagnetic

materials. However, in this study only the ferromagnetic domain structures are discussed. The domains are separated by domain walls (regions with non-uniform magnetisation direction) that add energy to the system so that infinite domains do not form. The various energy terms associated with domain wall energies are described in this section.

2.2.1 Exchange Energy

In ferromagnetic materials there exist unfilled electronic orbitals which give rise to spontaneous magnetisation due to the presence of unpaired atomic magnetic moments. However, in addition to this there exist strong coupling between the unpaired atomic moments, this coupling is known as an exchange coupling and the energy associated with their alignment relative to each other is the exchange energy.

It is the energy which arises as a result of the Heisenberg's exchange principle [1]. In ferromagnetic materials exchange energy favours parallel alignment of neighbouring spins and according to the Heisenberg Model it is expressed as

$$E_{ex} = -2J_{ex} \sum_{i,j} \boldsymbol{S_i}.\boldsymbol{S_j} \qquad [2.1]$$

where J_{ex} is the exchange constant between two neighbouring spins S_i and S_j. For Ferromagnetic materials J_{ex} is positive and the exchange energy is minimised within domains as the electronic spins are parallel. When J_{ex} is negative, in the case of antiferromagnetic materials, it leads to antiparallel alignment of neighbouring spins. However, in ferromagnetic materials, for the regions between domains i.e. for domain walls there is a competition between anisotropy energies and the exchange energy such that adjacent spins in a domain wall are not parallel. The wall width is governed by the energy considerations, with strong anisotropy favouring narrow walls which have high exchange energy and low anisotropy favouring wide walls with lower exchange energy as the relative angle between each neighbouring spins is smaller. The total domain wall width is defined as the region separating two magnetic domains over which the magnetisation undergoes a 180°

rotation of its spins distributed over N atomic planes. For a lattice parameter a the domain wall width, Δ is given by,

$$\Delta = Na = \pi \sqrt{\frac{A}{K_1}}$$ [2.2]

where K_1 is the anisotropy constant and A is the exchange stiffness of the material.

The highest energy configuration is when the two neighbouring spins align anti-parallel to one another as can be seen from [eq.2.1].

2.2.2 Zeeman Energy

The Zeeman energy contribution arises from the interaction of the magnetic moments with the external magnetic field. This energy is lowered when the magnetic moments align parallel with the external field.

The Zeeman energy is directly proportional to the product of the internal magnetization of the sample and the external magnetic field, H_{ext}. This relation scales with the permeability μ_0 as shown in eq[2.3]:

$$E_{Zeeman} = \mu_0 \int \boldsymbol{M_s}.\boldsymbol{H_{ext}} dv$$ [2.3]

The energy contribution vanishes for zero field.

2.2.3 Magnetocrystalline anisotropy energy

Magnetocrystalline anisotropy energy describes a preferred crystallographic orientation in which the magnetisation of a material will lie to have an energy minimum. It has been found that for single crystals there are certain crystallographic axes along which the magnetisation of a material is aligned in a lowest energy configuration. Such an axis is termed the easy axis. Conversely, if a larger field is required to saturate the sample along a particular axis along the crystal direction, the axis is

termed the magnetic hard axis. For Fe at room temperature it is shown in Fig 2.1(a) that it is easier to magnetise the body centre cubic crystal along the [100] direction compared to the [111] direction [2]. This is the opposite behaviour to that observed in single crystal Nickel [3] at room temperatures shown in Fig 2.1(b).

(a)

b)
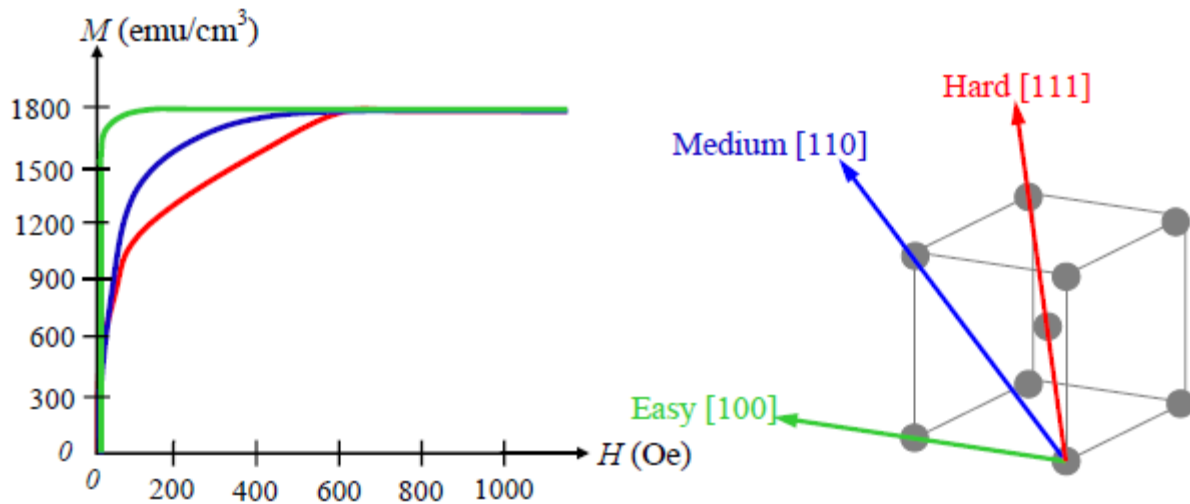
(b)
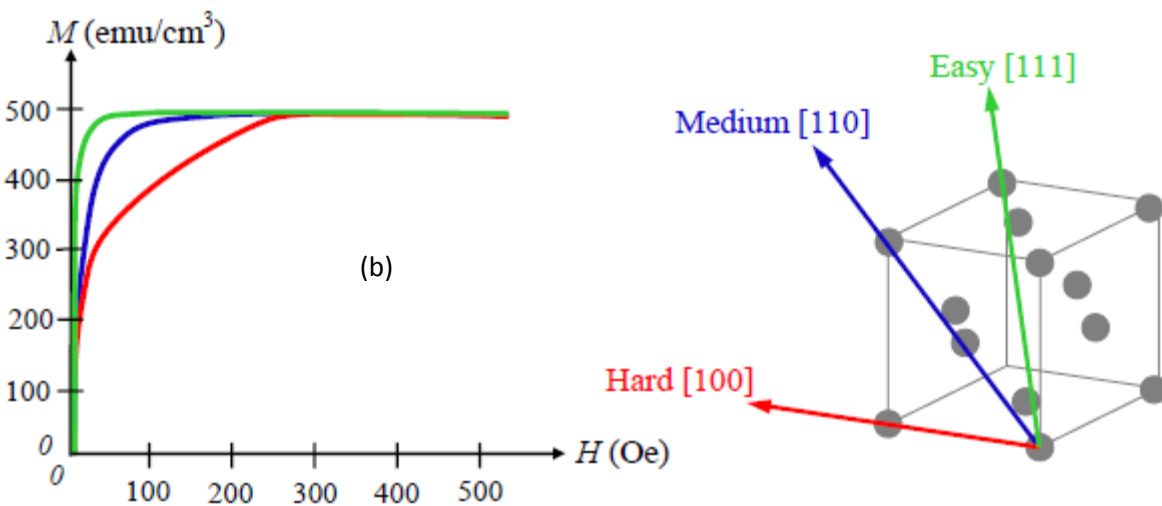
Figure 2.1:Magnetocrystalline Anisotropy relation for single crystal (a)Iron [2] and (b)Nickel [3]. Schematic(Right) indicates the easy and the hard axis crystallographic directions for both Fe and Ni

The magnetocrystalline anisotropy energy is the energy required to align the magnetisation along the hard axis from an easy preferred axis.

The Magnetocrystalline anisotropy (MCA) has a strong influence on the magnetisation configuration for many FM materials, but for materials such as Permalloy it is weak. For single crystal materials its effects are pronounced due to there being a definite anisotropy direction along certain crystal axes. However, for a polycrystalline sample with truly random orientation of the grains, the MCA energy in principle averages along all directions and there is no preferred orientation of the magnetisation [4], although there maybe local variations in magnetisation direction due to MCA. In reality however, an entirely random crystallite orientation may not be possible and polycrystalline material may exhibit small magnetocrystalline anisotropy in a particular direction. This is important to note as the materials discussed within this work are not single crystalline in nature. Anisotropy can be further enhanced by external effects such as the application of a magnetic field during deposition of the material. This leads to a field induced anisotropy associated with atomic pair ordering.

The Magnetocrystalline energy density is for cubic crystals such as Fe and Ni are given by:

$$E_K = K_1(\alpha_1^2\alpha_2^2 + \alpha_2^2\alpha_3^2 + \alpha_3^2\alpha_1^2) + K_2(\alpha_1^2\alpha_2^2\alpha_3^2) \qquad [2.4]$$

where K_1 and K_2 are the anisotropy constants for a particular material and α_1^2, α_2^2, α_3^2 are the direction cosines with respect to the cube edges.

For other materials e.g. cobalt the magnetocrystalline energy is uniaxial and for single crystals is defined by:

$$E_K = K_1 sin^2(\theta) + K_2 sin^4(\theta) \qquad [2.5]$$

Details for the anisotropy constant for Fe, Ni and Co are listed in Table 2.1 [5]. θ is the angle between the easy axis and the magnetisation as shown in Fig 2.2 .
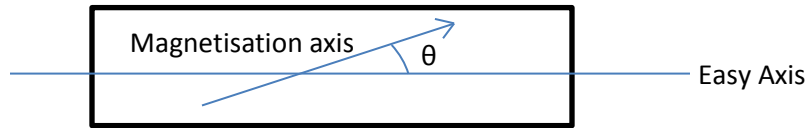
Figure 2.2: Schematic of the Magnetocrystalline axis within a crystalline material.

Various experiments on the anisotropy constants were originally performed by Bozorth in 1937 [6]. He demonstrated that the anisotropy constants are related to the lattice parameter and essentially become zero just before the Curie temperature is reached due to the thermal expansion of the lattice. For alloys such as NiFe which is considered during this study it was shown by Bozorth [7] that the crystalline anisotropy constant K_1 for a 81% Ni content alloy is very small.

	Fe	Ni	Co
K_1	4.8 x 10^4 Jm^{-3}	-4.5 x 10^3 Jm^{-3}	45.3 x 10^4 Jm^{-3}
K_2	1.0 x 10^4 Jm^{-3}	2.5 x 10^3 Jm^{-3}	14.5 x 10^4 Jm^{-3}

Table 2.1: The bulk room temperature magnetocrystalline anisotropy constants for the ferromagnetic elements iron, nickel and cobalt.

2.2.4 Magnetostatic Energy-Shape Anisotropy

The Magnetostatic energy of a material is similar to the Zeeman energy contribution except its origin is from the magnetisation within the sample. This energy arises from self-interaction of the magnetization within the sample where stray fields are created in the sample. A stray field is produced by the moments, this is minimised by the formation of domains as explained here. This

magnetic term is long range compared to the length scale of the exchange interaction. A uniformly magnetised sample develops a magnetic flux which is continuous within and around the sample.

This is shown in the Fig 2.3.
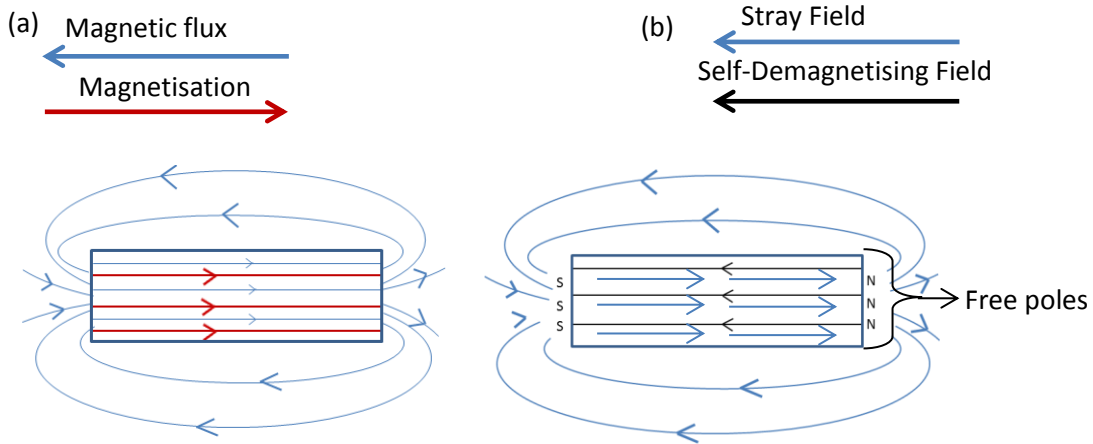
Figure 2.3: Showing the (a)stray magnetic flux outside the sample volume and a (b) net demagnetising field setup inside the sample

The magnetization within the sample leads to the development of free poles at the ends of the sample thereby setting up of an associated field opposing the magnetization within the sample, the demagnetising field, H_d. This demagnetizing field opposes the magnetic flux in the vacuum produced by the magnetization within the sample.

The magnetostatic energy is minimised when the stray field produced by the magnetization is reduced. The formation of domains reduces the stray field and depending upon the material can ultimately lead to complete flux closure in which case, the magnetostatic energy goes approximately to zero.

2.3 Energy Minimisation and Domain formation

The total magnetic energy associated with a magnetic system is given as a net contribution of all the energy terms describing a magnetic system:

$$E_{tot} = E_{magetostatic} + E_{ex} + E_K + E_{zeeman} \qquad [2.6]$$

A change of the alignment of the magnetic moments in the material changes the different energy terms as shown in eq[2.6] and the competition between the various terms controls the magnetisation behaviour. An equilibrium state is obtained when the total energy is minimised. Two key competing energies in domain wall magnetism are E_{ex} and E_K .

The Exchange energy as outlined above is minimised when the angle between a pair of neighbouring spins is zero. This leads to parallel alignment of the spins which ultimately leads to ferromagnetism. However if all the spins within a material are parallel, the magnetostatic energy of the system will be large due to the formation of significant surface magnetic charges near the edge of the sample. This thereby leads to an increase in the total energy. The formation of magnetic domains reduces the magnetostatic energy. The domains are separated by regions known as domain walls. The presence of domains lowers the magnetostatic energy, but the exchange energy of non-aligned spins in the domain walls increases the energy. The competition between the two energies leads to a minimum which is a balance between a reduction of the magnetostatic energy and increase in energy associated with adding more domain walls.

Fig 2.4 shows three different schematics for magnetic domain configurations. In the first case shown in Fig 2.4(a) the exchange energy is minimised. However the magnetostatic energy is high due to the formation of magnetic charges on the edge of the sample as explained in section *2.2.4* . This can be lowered by forming two anti-parallel magnetic domains. Due to the flux closure of the stray field the

magnetostatic energy is reduced. A further reduction in energy is possible for samples with cubic magnetocrystalline anisotropy the flux can be completely closed as shown in Fig 2.4(d). For materials with no crystalline anisotropy the domain landscape [5] is defined by the shape anisotropy.
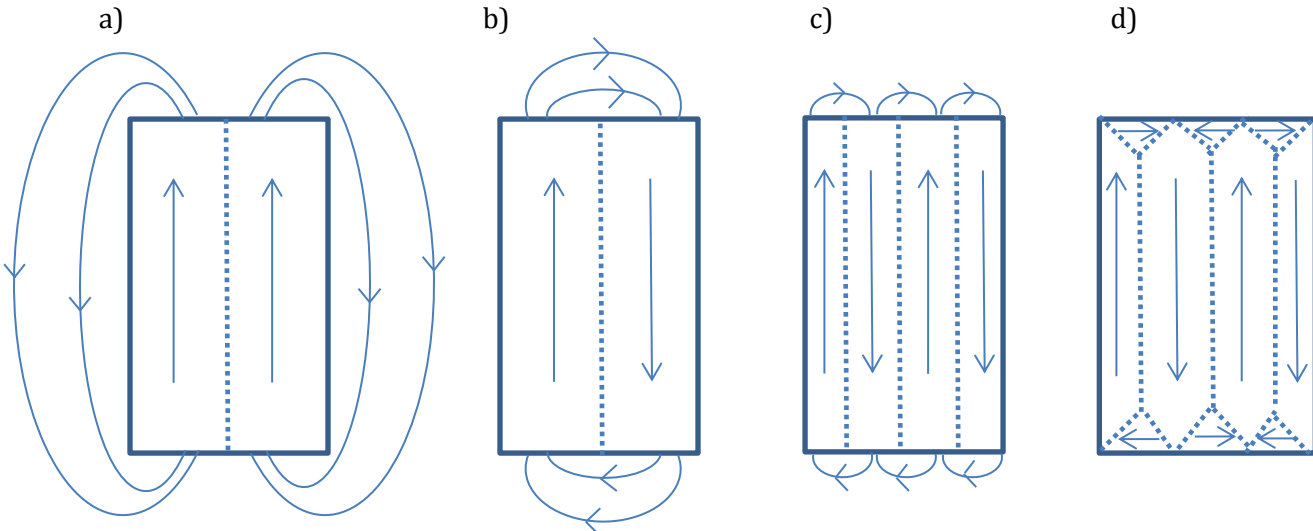
Figure2.4: Schematic of the (a-d) stray fields and the formation of domains. Multiple domains are formed inorder to reduce the magnetostatic energy and hence the stray fields. (d) shows an ideal case where there is complete flux closure of the stray fields and the energy is minimised.

Thus there is a certain amount of energy associated with the introduction of domain walls in the system. The energy considerations can lead to different types of domain walls (Bloch, Neel and a vortex wall) [5]. Apart from the domain wall energy considerations, there are additional energy terms such as the Dzyaloshinskii-Moriya Interaction [45] which can lead to the stabilization of the Neel wall in materials which have structural inversion asymmetry. However, the discussion of this is beyond the scope of this thesis. Domains and domain walls in real systems are more complicated than the simplistic models presented here. Nevertheless, the operating principle behind the final domain structure is such that if the energy of the system can be lowered by domain wall formation, it will reduce its energy from a saturated configuration to that of a lower energy by the process of forming domain walls. For thin continuous films the dipolar and stray fields contribute to the

domain structures. For wide patterned micro-wires the magnetostatic energy would favour flux closure states and therefore reduce the total energy by forming multiple domain walls. As the wire width is reduced, the amount of energy gained by not favouring exchange anisotropy and forming multiple domains to lower the magnetostatic energy is *higher* than favouring exchange interaction. Therefore, the state of lowest energy becomes one favouring a single domain in which magnetisation aligns parallel and along the long axis of the wire due to shape anisotropy.

The above discussion is based purely on magnetic fields that can be either external or internal. However when this is combined with the application of electrical current interesting phenomena arise. The next section outlines the theory behind different Magneto-resistance phenomena specific to this work.

2.4 Electrical resistivity in 3d Transition metals

To understand magneto-resistance one must understand the origin of resistance in these ferromagnetic transition metals and their alloys.

In 3d ferromagnetic (FM) transition metals an intrinsic magnetic moment exists due to a number of unpaired spins in the *d* orbital. The electrical resistivity of FM transition metals is also higher when compared to an alkali metals or non-magnetic transition metals [8][9][10] . In order to understand the origin of Anisotropic Magneto-Resistance (AMR) one must understand the processes giving rise to resistivity in *3d* metals and consider the density of states at the Fermi level for each metallic species as shown in Fig 2.5. Fig 2.5(b) shows the splitting of the *d*-sub band into spin-up and spin-down. There exists a difference in the density of states available for each band at the Fermi level indicated by E_F.
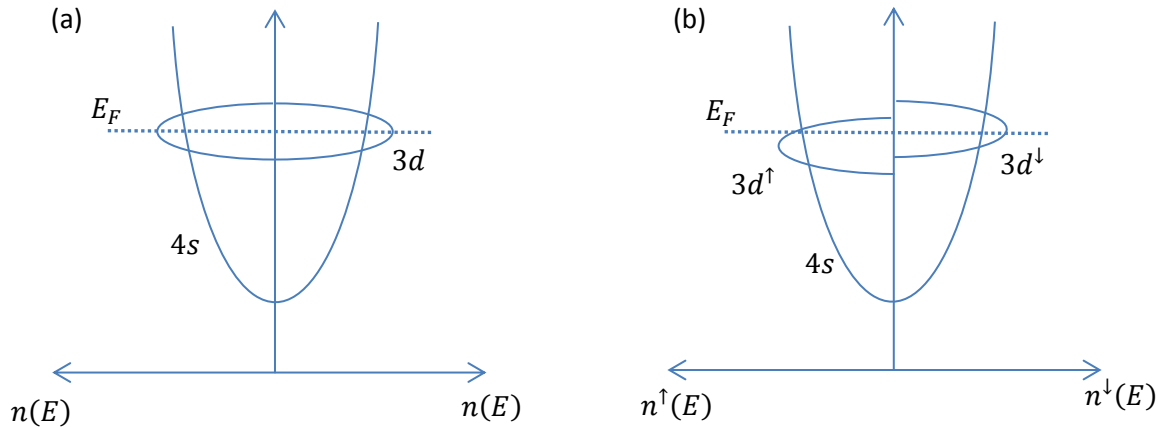
Figure 2.5: Schematic of the *4s* and *3d* band structure and the distribution of the density of states for a non-magnetic metal (a)(left) and a magnetic metal (b)(right). The *3d* band is split in the spin up and the spin down states.

The electrical conductivity at low temperatures is due to the collision between the conduction electrons and impurity atoms or other imperfections in the crystal. At room temperature the conductivity is governed by the collision of the conduction electron with phonons and the crystal lattice. Therefore the resistivity inherently depends on the number of collisions or the scattering probability of a conduction electron. If the mean free path of the conduction electron for a given temperature and given number of scattering sites is small the electrical resistivity will be high. For the scattering process to be completed there must also be a certain number of available states for the conduction electrons to scatter into. At the Fermi level of a FM transition metal the *d* band has a number of available states and there exists an orbital overlap between the *s* and the *d* orbitals. This hybridisation allows the parabolic *s* orbital to take on some characteristics of the flatter *d* orbital and allows for the more delocalised *s* electrons, which have a lower effective mass to conduct and scatter into the available *d* orbital states. Due to the large number of available *d* states and the orbital overlap at the Fermi surface there is a greater probability of scattering into the *d* states (*s-d scattering*) compared to ordinary scattering [10]. As a result of this increased scattering into the *d* orbital the mean free path of the *s* electrons decreases and the electrical resistivity increases.

2.4.1 Exchange splitting and the Mott two current model

Significant developments in understanding of the conduction mechanisms in magnetic metals were made by Slater and Stoner from 1933-1936. One of the motivating factors was to try and answer why theoretically; the effective number of Bohr magnetons has a non-integer value for ferromagnetic atoms? In order to answer this one needs to understand the process of exchange splitting in FM materials.

In FM transition metals the *4s* band is preferentially screened as it is closer to the nucleus as compared to the *3d* band. The *4s* band therefore is of lower energy than that of the *3d* band and begins to fill first. The *3d* band, which is of higher energy, is filled next. The narrow *3d* band, in terms of energy, has a filling capacity of 10 electrons (5 spin-up and 5 spin-down electrons). The *3d* orbital is exchange split implying that there are two sub bands in the *3d* orbital, the spin-up (parallel) and the spin-down (anti-parallel) band. The parallel spins energy configuration is a lower energy state and the electrons with parallel spin orientation are preferentially filled followed by the remaining electrons. The exchange split *3d* band and the preferential filling of electrons in the specific orbitals leads to a spin imbalances which in turn leads to the production of a net magnetic moment.

The effective number of Bohr magnetons n_{eff} gives an estimate of the number of unpaired spins per atom. It is defined as:

$$n_{eff} = \frac{M_S(0)}{n\mu_B}$$

[2.7]

where $M_s(0)$ is the saturation magnetisation at T=0 K, *n* is the number of atoms per unit volume and μ_B is the Bohr Magneton. For Fe, Ni and Co is n_{eff} is 2.22, 1.72 and 0.6 Bohr magneton per atom.

In order to experimentally obtain non-integral values of n_{eff} there must be a difference in the density of states for the spin-up and spin-down electrons in the exchange split bands at the Fermi

level. Therefore for FM metals such as Fe, Ni and Co one observes there to be a difference in the *s to d* scattering rates for the spin-up and spin-down conduction electrons.

For temperatures below the Curie point, T_c, the electron spin flows independently in their respective minority and majority channels and there is very little contribution from spin-flip scattering events in the conduction process i.e. the spin direction of an electronic charge is conserved during a scattering process. As temperatures are increased towards the Curie temperature, the number of magnons in the material increases. This causes the mixing of spin-up and spin-down conduction channels. A spin up conduction electron is scattered to a spin down state by the annihilation of a magnon. This contributes to the increase in the total resistivity as the number of scattering events in the lower resistivity channel is increased.

In 1936 Neville Mott proposed a two current model [11] which is explained schematically in Fig 2.6. The model attempted to explain the resistivity in a Ferromagnetic conductor for temperatures below the Curie temperature. He suggested that current in a FM conductor is carried in two independent channels and the total conductivity of a FM arises as a contribution of the majority and minority conduction electrons.
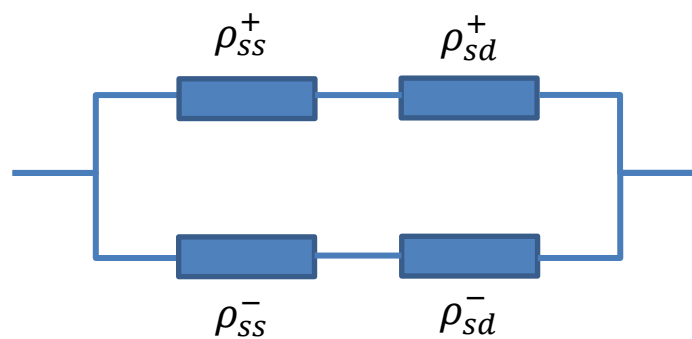
Figure2.6: Schematic of the Mott two current model in which individual resistivity contributions are shown for *s-s* and *s-d* scattering for both the majority (+) and minority (-) spin channels which is equivalent to spin ↑ and spin ↓ .

There were two assumptions in this model which are outlined below:-

1) The spin of each electron is preserved- i.e. there are no spin-flip scattering events occurring on interactions with defects. Spins can be flipped by magnon scattering but at low temperatures there is very low density of magnons and phonons and therefore no spin-flip scattering events occur.

2) Conduction is always mediated by the *s* electrons due to their relatively lower effective mass compared with the *d* electrons.

The scattering probabilities for majority (+) and minority (-) channels in the two current model as shown in Fig 2.6 can be added, this implies,

$$\rho^- = \rho^-_{ss} + \rho^-_{sd} \qquad \rho^+ = \rho^+_{ss} + \rho^+_{sd} \qquad \alpha = \rho^-/\rho^+ \quad [2.8]$$

Even though the two current model explains the resistivities in FM metals it is experimentally difficult to measure individual resistivities. However, Fert and Campbell [12] have measured the residual resistivities and temperature dependence for binary and ternary alloys and deduced the ratio α for dilute alloys of Fe, Co and Ni [13]. The two current model is only valid for temperatures below T_c.

As temperatures rise, one begins to excite magnons (spin waves). It is the magnons which cause the mixing of the two majority and minority conduction channels [14] via electron-magnon scattering and spin-flip scattering events dominate and contribute towards the electrical resistivity. It then becomes increasingly possible for spin-up electrons to scatter into an unoccupied spin-down state. Recently Rowan-Robinson *et al* [15] proposed a modification to the theory behind the breakdown of the Mott two current model and the mixing of the independent current channels.

2.4.2 Anisotropic Magneto-Resistance

The Anisotropic Magneto-Resistance (AMR) is a transport phenomenon which involves the direction of current applied and the magnetisation of the ferromagnetic material. The resistance of a FM material depends on the angle between the direction of applied current density **J** and the magnetisation vector **M** as shown in the Fig 2.7(c).
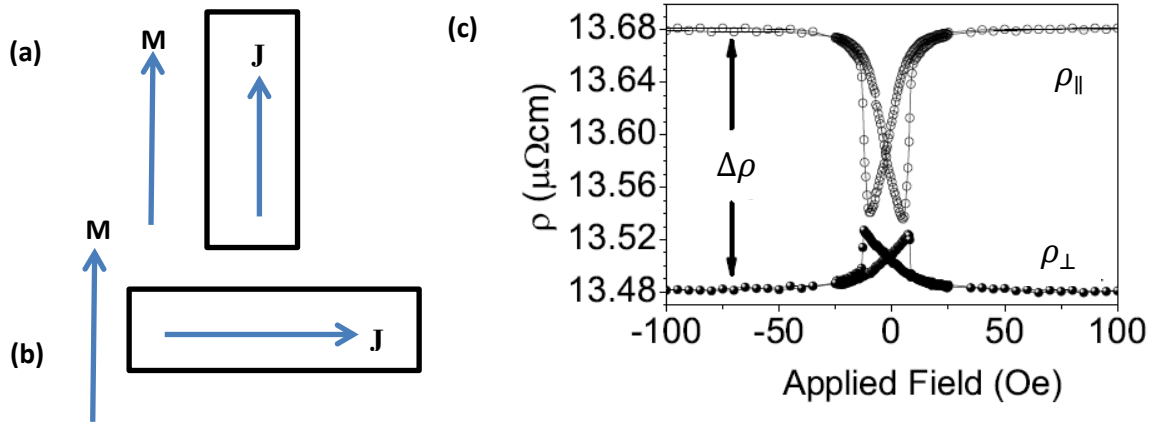
Figure2.7: Schematics for geometry of (a) longitudinal in-plane orientation and (b) transverse in plane orientation showing relative directions of current and magnetisation. (c) Schematic for a typical change in resistivity as a function of the applied in plane field in Oersteds [16].

When the external fields saturates the magnetisation of the material in the plane of the sample and the current applied is parallel to the magnetisation the value of resistance obtained is larger than when the magnetisation and current applied are perpendicular and in the plane of the sample[17] [18]. For the geometry when the magnetisation and current are orthogonal and in-plane the resistivity obtained is defined as transversal resistivity, $\rho_\perp$ and when the angle, θ between the magnetisation is 0° implying that the current and magnetisation are parallel, then the resistivity obtained is defined as longitudinal resistivity, $\rho_\parallel$. AMR is therefore defined as the ratio of the change in resistivity to the resistivity for the transverse orientation as:

$$AMR = \frac{\Delta\rho}{\rho_\perp} \qquad\qquad [2.9]$$

The average resistivity is defined as a contribution of the net resistivity for both transverse and longitudinal orientations,

28

$$\rho_{avg} = \frac{1}{3}(\rho_{\parallel} + 2\rho_{\perp}) \qquad\qquad [2.10]$$

Traditionally in the definition of AMR [17] the transverse resistivity is replaced by resistivity value when external field is 0. However, physically it is more meaningful to use the definition as described in equation[2.9] as the magnetic state i.e. the domain configuration at H=0 is dependent on the history of the sample. It is also valid to use an average resistivity value in the definition of AMR [17] [10]. In an ideal case one would attribute equal contributions to the resistivity value in both transverse and longitudinal directions as well as the out-of-plane directions. However, for the materials studied in this thesis the magnetisation lies inherently in the plane of the sample and therefore the out-of-plane term does not contribute to the AMR. In any definition of the AMR ratio, it is important to have a defined state of the magnetisation. With regard to this study it is important to note that $\rho_{\parallel}$ is identical to the value of resistivity when magnetisation and current are anti-parallel. The reason for this is detailed within the mechanism of AMR as shown in section (2.4.3), $\rho_{\parallel}$ and $\rho_{\perp}$ are the high and low resistance states for this magneto-resistance effect. Since AMR depends on the relative angle between the magnetisation and the current its angular dependence can be defined as:

$$\rho(\theta) = \rho_{\perp} + \Delta\rho cos^2(\theta) \qquad\qquad [2.11]$$

Here it can be seen that when θ = 0° or 180° the resistance is higher compared to when it is 90° or 270°. The microscopic origin for the anisotropy in this Magneto-Resistance effect is explained briefly in the following section for a more detailed review the reader is directed to [19] [17].

2.4.3 Microscopic origin of Anisotropic Magneto-Resistance

The microscopic origin of AMR was proposed by Smit in 1951[20]. He proposed that spin-orbit interaction (SOI) is the origin for AMR. He argued that in order for one to observe AMR ($\rho_{\parallel} \neq \rho_{\perp}$)

spin-flip scattering must occur and the SOI aids this, because AMR tends to approach zero as the temperature rises towards the Curie temperature he argued that SOI causes the inter-mixing of the spin-up and spin-down current channels at the Fermi surface. This allows for *s* electrons to scatter into available unoccupied down states.

The reason for the difference in resistivity values for $\rho_\parallel$ and $\rho_\perp$ and the origin of AMR is explained by Smit as follows. Due to the localised nature of the *d* orbital with respect to the lattice, there is a difference between the number of available states that are present along the lattice and in the direction perpendicular to it. There are fewer hole orbits available for scattering in the direction perpendicular to the magnetisation. Therefore, when the current is applied parallel to the magnetisation there are a large number of orbitals present into which the *s* conduction electrons can be scattered. Consequently the scattering probability and the number of available sites for the *s* electron for the direction perpendicular to the magnetisation plane is high [10]. Since resistivity is proportional to the number of scattering events therefore, $\rho_\parallel > \rho_\perp$.

2.5 Spin-dependent scattering and the Giant Magneto-resistance

The basis for the discovery of GMR which has further led to development of higher sensitivity read heads and spin valves in the magnetic storage industries is based on spin-dependent scattering in FM transition metals.

As highlighted earlier in section 2.4 the electrical resistivity of ferromagnetic transition metals is usually higher than the average resistivity of para- and dia-magnetic transition metals. This is because of the large number of available *d* band states for conduction electrons to scatter into. These partially filled *d* bands contain unpaired spins which lead to ferromagnetism. The *d* orbitals are spin-split, implying that there is a difference in the density of states (DoS) for the spin-up and

spin-down electrons at the Fermi surface. This difference in DoS gives rise to different scattering probabilities for spin-up and spin-down electrons. Therefore, when an electrical current is introduced in a ferromagnetic material it becomes spin polarised allowing a certain channel of spins to dominate the conduction. This is the underlying principle of the Giant Magneto-Resistance phenomenon described below.

2.5.1 Microscopic origin of GMR

When an electron charge current is incident on a ferromagnetic material it undergoes spin-dependent scattering, the FM acts as a spin filter, in which certain spin orientations scatter more and are reflected, than others that undergo minimum spin scattering. Exhaustive studies involving spin-dependent scattering were conducted by Ian Campbell and Albert Fert [21][22]. They proved that spin-up and spin-down electrons conduct in separate channels and demonstrated that mixing Ni with impurities of different spin asymmetries leads to different spin-dependent scattering [23]. This ultimately led to the discovery of the GMR effect in 1988 by Fert [23] and Grünberg independently [24].

When two FM layers are placed in close proximity to each other, separated by a non-magnetic transition metal, then depending on the direction of the magnetisation of each of the layer their spin-dependent scattering for incoming electron spins will be different and together they can act as a spin-valve. Depending on the relative orientation of the magnetisation between the two ferromagnetic materials their coupling may be ferromagnetic (parallel) or antiferromagnetic (antiparallel) thereby giving different resistance values when a current is injected. This effect is termed as the Giant Magneto-Resistance [25]. Peter Grunberg obtained antiferromagnetic coupling in Fe/Cr/Fe thin films in 1986 [24]. Electrons, when injected into a FM material undergo spin-dependent scattering. Electrons with their spins parallel to the magnetisation of the FM undergo less scattering compared to electrons with spins anti-parallel to the bulk of the FM material.

Therefore the resistance contributions from each of these spin-dependent channels can be considered as a resistor network as shown in Fig 2.8.
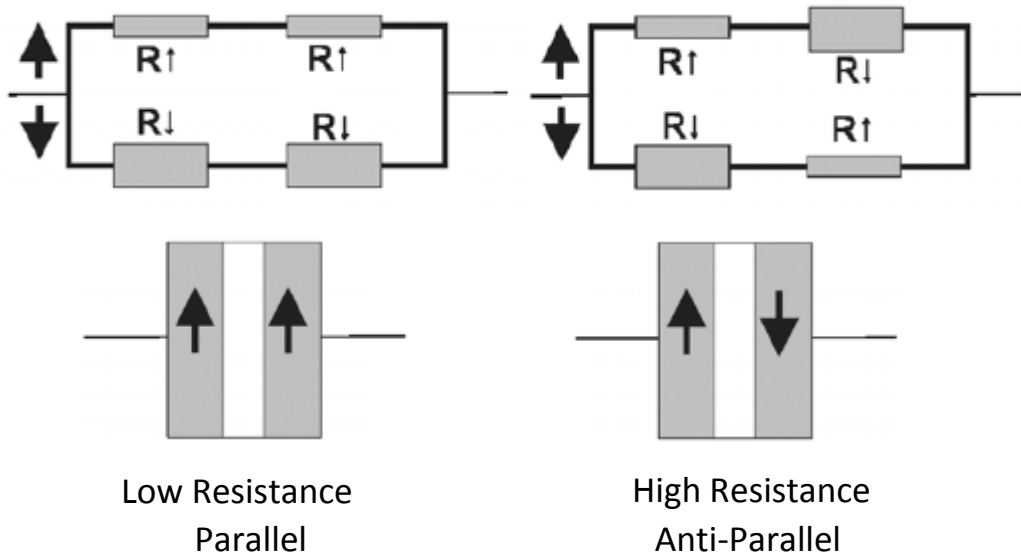
Figure2.8: Line diagram showing the individual spin channel resistance contributions for (a) parallel and (b) anti-parallel alignment of two coupled FM layers [23].

Consider the case when the magnetisation of both FM layers are parallel to each other, the spin-up electron with its spin orientation parallel to the magnetisation **M** will undergo minimum scattering and contribute least to the resistance. The spin-down minority electron will undergo heavy scattering and will give a higher resistance contribution to this current channel. Therefore, the current will pass through the majority channel due to the lower net resistance. For the case when the magnetisation of each layer is anti-parallel both the spin orientations will undergo scattering and will contribute to high resistance values as shown in Fig 2.9. Therefore for anti-ferromagnetically coupled state of the two layers the total resistance is higher than for the ferromagnetically coupled state of the GMR stack.
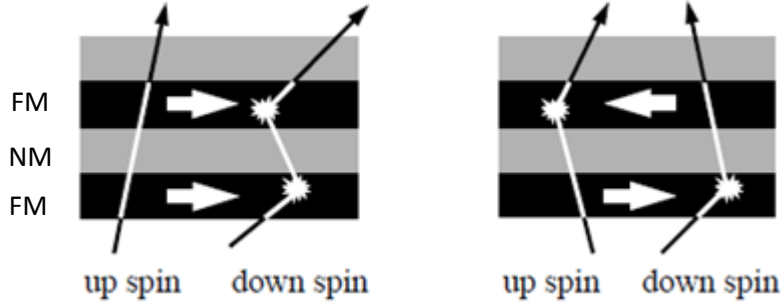
Figure 2.9: spin-dependent scattering probabilities for spin-up and spin-down electrons. Parallel magnetisation (a) allows low resistance in 1 spin channel and high resistance in another. For the antiparallel case(b) both spin channels experience scattering and therefore give rise to a high resistance [23].

From Fig 2.8 the resistances for each spin channel can be computed for both the parallel R_P and the anti-parallel state R_{AP} [23].

$$R_P = \frac{R_\uparrow R_\downarrow}{R_\uparrow + R_\downarrow} \qquad\qquad [2.12]$$

$$R_{AP} = \frac{R_\uparrow + R_\downarrow}{2} \qquad\qquad [2.13]$$

The total GMR effect is defined as the fractional change in resistance to the resistance in the saturated state as,

$$\frac{\Delta R}{R} = \frac{R_{AP} - R_P}{R_P} = \frac{(R_\downarrow - R_\uparrow)^2}{4R_\downarrow R_\uparrow} \qquad\qquad [2.14]$$

It is assumed that there is little or no spin-flip scattering for the above formula to be valid.

Indirect exchange coupling may lead to antiparallel alignment of magnetic moments in the two FM layers, this will lead to a significantly higher resistance due to the spin-dependent scattering. On application of a saturating field the two magnetic layers' magnetic moments will align parallel and a lower resistance will be achieved, more importantly, this is *independent* of the direction of the applied field. As described earlier in section 2.2.1 the exchange interaction takes place between two

neighbouring electron spins and is a localized interaction. The indirect exchange interaction, as the name suggests, allows two separate magnetic layers to essentially interact over larger distances via a nonmagnetic spacer layer, which acts as a medium to link the two FM layers. The spin of one FM layer is coupled via this indirect exchange coupling through itinerant electrons present in the NM spacer layer to the spin in the second FM layer. This type of indirect coupling is oscillatory in nature and depends on the thickness of the non-magnetic spacer. The indirect exchange interaction may be treated as a *superexchange* interaction. A detailed description involving the indirect exchange coupling through the spacer layer is given by C. Marrows in his PhD [26]. A phenomenal series of experiments conducted on oscillatory coupling through various transition metals was done by S.S.P. Parkin [27] [28].

2.6 Thin film deposition and lithography

The initial concept of spin-dependent scattering asymmetries was laid by Fert and Campbell as early as 1971 [29] where they tested Mott's two current idea. Whilst this was the precursor to a working GMR spin valve, technology was yet to reach a *certain level of sophistication* in terms of thin film growth and optimisation of the various steps in processing and patterning of films into devices. The two basic techniques used here for thin film deposition and lithography are discussed within this section along with the relevant theory required to understand the experimental background which follows. The growth and lithography techniques described here as an overview and the reader is directed to comprehensive texts for a complete description of different deposition techniques used for depositing various powdered, bulk and thin films [30][31].

2.6.1 Sputter Deposition

Of all the growth techniques available the one that has delivered with regard to the industrialisation of GMR devices is sputtering. Sputtering is a type of Physical Vapour Deposition (PVD) technique. It is a molecular mechanical process in which gaseous ions are used to knock out atoms from a target surface. A schematic of the processes involved at the atomic level is illustrated in Fig 2.10.
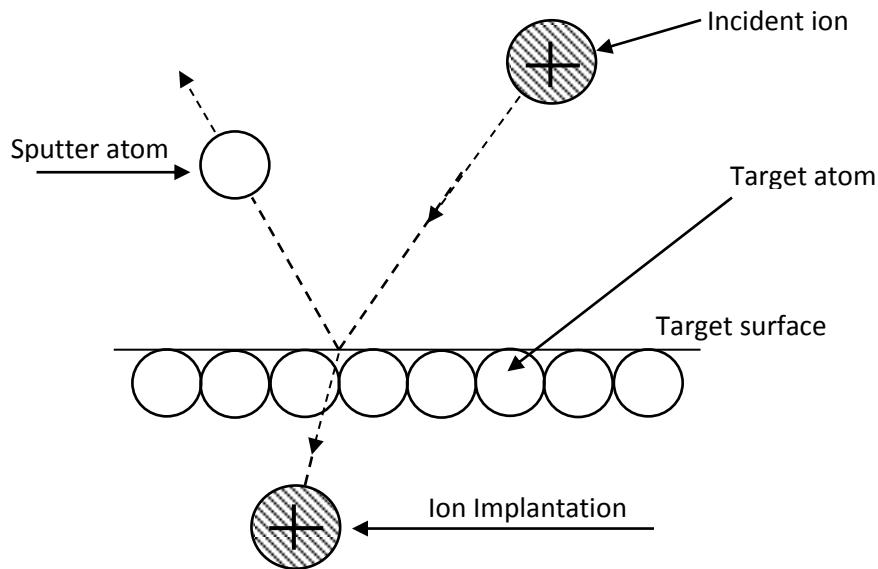
Figure 2.10: Simplified mechanical processes involved during sputtering of a target material.

Sputtering is the favoured method of choice because of its excellent throughput, high scalability and excellent film quality. It is possible to deposit vast number of elemental species as well as oxides and alloys. One of the major advantages of sputter deposition is its ability to maintain stoichiometry during the deposition of alloys and allow for uniform film deposition over 300mm wafers used in the storage industry [51].

Sputter deposition is performed in Ultra High Vacuum stainless steel chambers in the presence of a precursor gas which is usually a noble gas and most often argon. In D.C sputtering of metals a potential difference is created between the target cathode and the substrate. This high voltage causes the breakdown of the injected gas species to ions which are accelerated towards the target material. These ions bombard the target which causes the release of target atoms, these atoms then disperse throughout the chamber and subsequently, adhere to a substrate which is placed directly opposite the target. A schematic detailing the chamber and the various components involved in the process of sputtering is shown in Fig 2.11. In addition to the deposition of the material on the substrate one might also obtain Ar implantations within the deposited film. The high applied potential causes the cathode to emit electrons and leads to the breakdown of the gas atoms to ions forming a plasma. Once the gaseous atoms are initially ionised recombination of the electrons with the ionic species present in the chamber causes a glow discharge. In the process of erosion of the target material and also secondary electrons are released, which help in the sustaining the plasma and therefore the process of sputtering. Conventionally D.C. Diode sputtering is an inefficient process due to the large amounts of heat that is generated at high deposition rates. In order to reduce the high voltages required for high deposition rates and yet keep the high sputter rates, one must increase the number of bombardments at the target surface. This is done by confining the plasma near the target surface using magnets underneath the target in a process called magnetron sputtering. The magnets are oriented such that they form closed field loops through the target surface. This magnetic field confines electrons to ionise Ar atoms near the surface of the sputter target thereby leading to higher deposition rates. Due to the increased plasma near the surface the process can be carried out at a lower pressure. A schematic showing the chamber and the process of sputtering is shown in Fig 2.11.
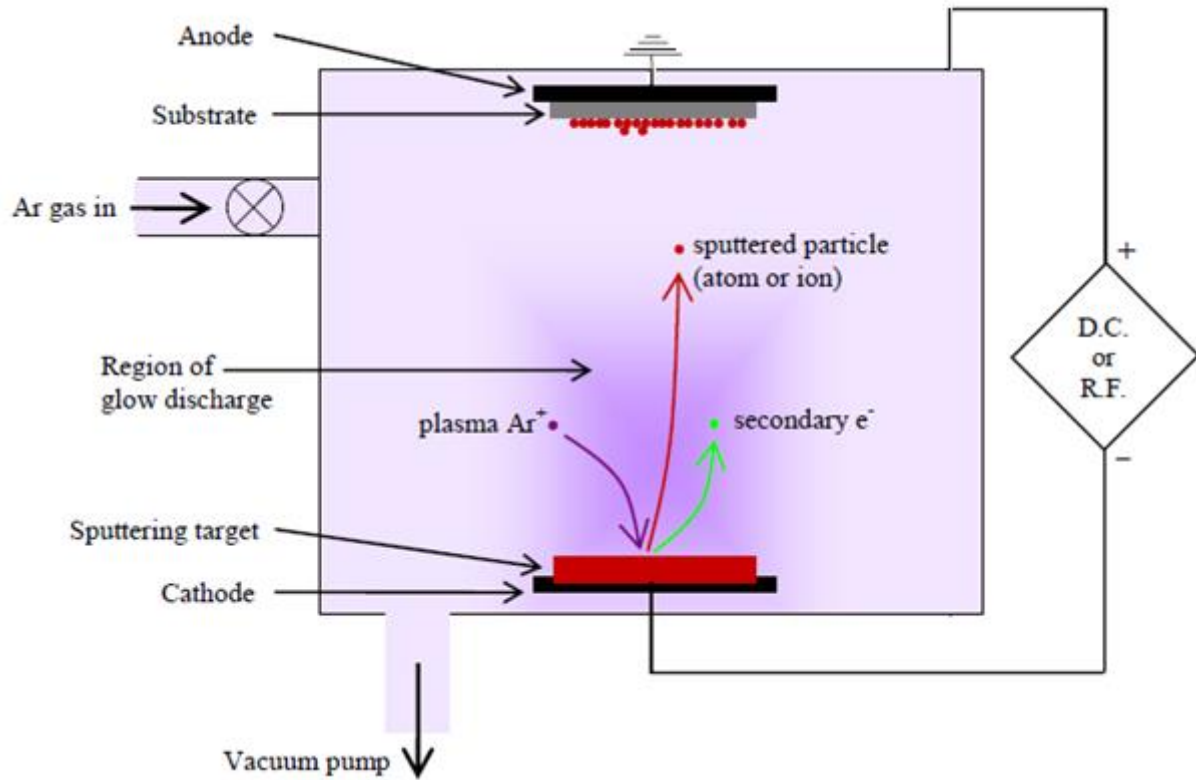
Figure 2.11: Schematic of the process of sputter deposition with Ar gas in a UHV chamber illustrating the glow discharge [32].

For the deposition of magnetic insulators one must employ R.F. sputtering. D.C magnetron sputtering causes a build-up of positive charges on the surface of the electrically insulating materials (Al_2O_3, MgO) which repels the incoming ion bombardment. By applying an alternating current these charges are dissolved and the deposition process can continue. The growth of MRAM-type devices and GMR or TMR read heads often requires a combination of different sputtering processes for different layers used within the stack.

2.6.2 Nanopatterning

The process of producing GMR sensors requires not just deposition of thin films but structuring them into nanoscale devices. Reducing the dimensions of the thin films allows one to have control over the path of current flow and confine the magnetisation to lie along a particular direction due to the contributions of shape anisotropy.

Due to the rapid growth of the storage industry and storage capacities of Hard Disk Drives [33] the memory cell sizes are gradually approaching the super-paramagnetic limit in which only due to thermal fluctuations the magnetisation stored in a single bit can be reversed by overcoming the bit switching field and the information is lost [34]. One method of preventing this and increasing bit density per unit area is to increase the magnetic anisotropy of the bit and by scaling down the bit size one may enhance the shape anisotropy which will lead to high densities.

There exist two general classes of method for structuring of nanoscale features, the top-down and the bottom-up approach. The former is more scalable and allows for systematic long range order and coverage, but it usually makes use of sequential writing/patterning through a mask or a predefined template to be written on a substrate this is usually a slow process. The bottom up or "self-assembly" approach refers to using short range interactions between two atomic or molecular species to produce large area coverage. Using such a technique high spatial resolution can be obtained however the repeatability of structures over a large range is poor [35]. In this work the top down method of optical lithography was used.

Other methods of lithography also exist, a detailed text describing electron beam lithography and its effects on edge roughness on magnetisation dynamics in planar nanowires can be found by D. Atkinson [36]. For the sizes of the structures used in this study the method of choice of patterning was optical lithography and the process of producing samples using such a method is illustrated in

Fig 2.12. It is possible using a combination of masks, resists and using deep ultraviolet light to produce structures of 200 nm [37]. Optical lithography is a top down patterning process in which the pattern is produced after coating the entire area of interest with a resist layer. UV light is exposed through a mask with the desired structures, this causes a change in the chemical composition of the resist, which when inserted into a developing solution is either removed or remains depending on the tone of the resist. After this the magnetic material is deposited through the resist mask and then the remaining resists is lifted off using an organic solvent.

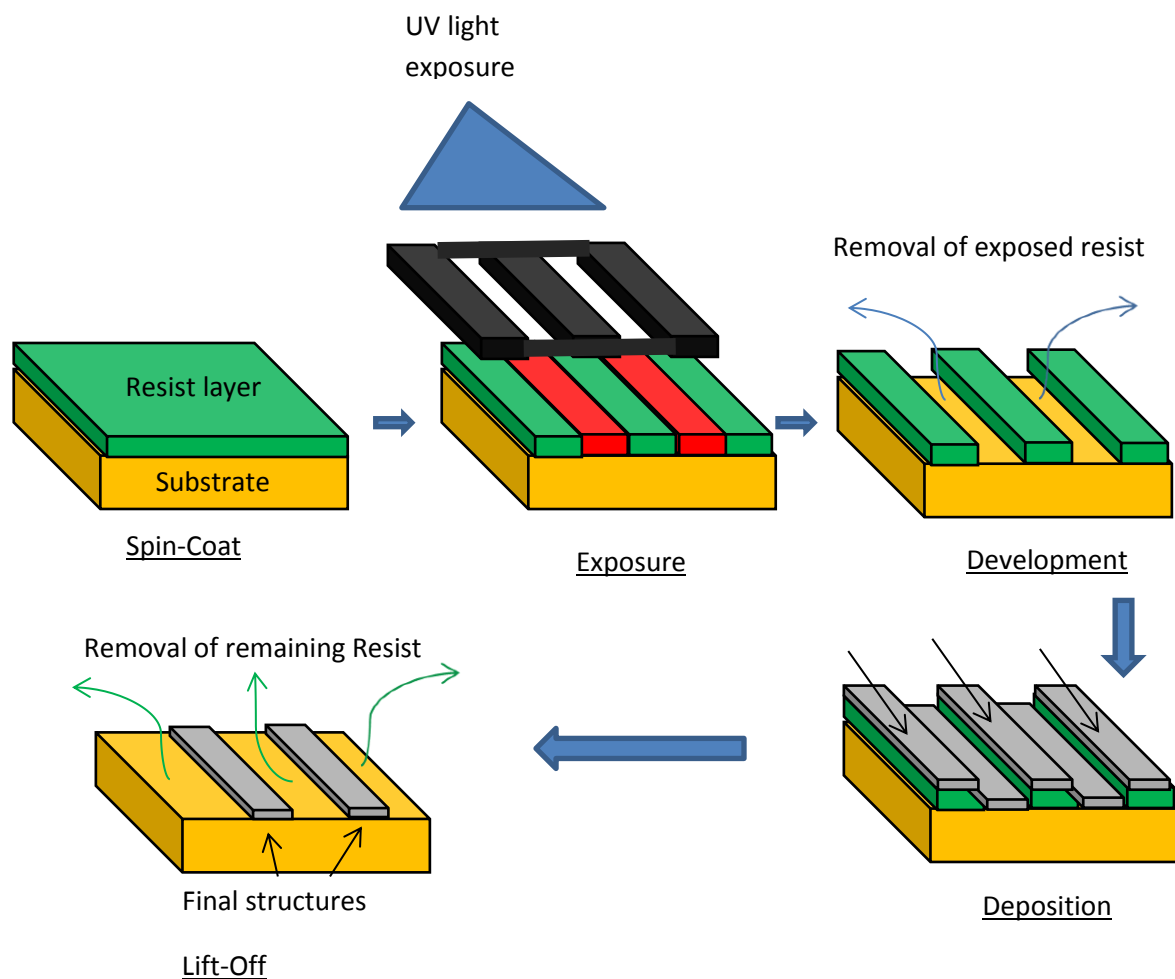

Figure 2.12: The process for device fabrication using optical lithography is outlined, illustrating different steps involved. UV light is exposed on the spin coated resist through a mask this is followed by chemical alterations in the photochemistry of the resist in a developing solution. After which the film is metalised and finally the structures are obtained by lift off usually in acetone.

2.7 Magneto-Optical Kerr Magnetometry

One of the fundamental characteristics of any ferromagnetic material magnetisation reversal is magnetic hysteresis. The Magneto-Optical Kerr Effect (MOKE) is a phenomenon which may be exploited in order to study changes in magnetisation of a magnetic material and particularly thin films and multilayers as a function of an external applied magnetic field. The first magneto-optical effect was observed by Faraday [38] in which polarised light when transmitted through a material shows a change in the plane of polarisation. The degree of change depended on the strength of magnetisation of the studied sample. The MOKE effect is a material dependent property which can be described as the change in polarisation of reflected light and is directly proportional to the change in the magnetisation of the investigated material [39] [40].

Depending on the energetics of the material system as described in section 2.3 the magnetisation can lie within the plane of the material or out of the plane. Depending on which magnetisation configuration is to be probed there exist three different geometries in which MOKE magnetometry may be used. These geometries are outlined below with a brief description of the physical origin of this effect.

2.7.1 Geometries of the MOKE

There are three different geometries in which the MOKE effect is commonly observed. These are defined in relation to the orientation of the magnetisation within the sample and the plane of incident light. These geometries are shown schematically in Fig 2.13.

When the magnetisation of a sample lies in the plane of the sample and is parallel to the plane of incidence and reflection, such geometry is referred to as the longitudinal configuration. The transverse geometry is realised when the magnetisation lies in the plane of the sample but is perpendicular to the polling direction. The third geometry in which one is able to measure the

MOKE effect is used for materials in which the magnetisation lies out of the plane of the sample and is also perpendicular to the plane of incidence and reflection. These three geometric configurations are outlined in Fig 2.13. In longitudinal and polar MOKE the plane of polarisation is rotated by changes of magnetisation. For the transverse effect the light amplitude is changed with magnetisation and not the polarisation.

Due to the energetics of the system investigated in this study the magnetisation of the thin films with nominal thicknesses investigated all lie in the plane of the sample. Therefore, both the longitudinal and the transverse MOKE geometries were used to study the changes in the magnetisation.
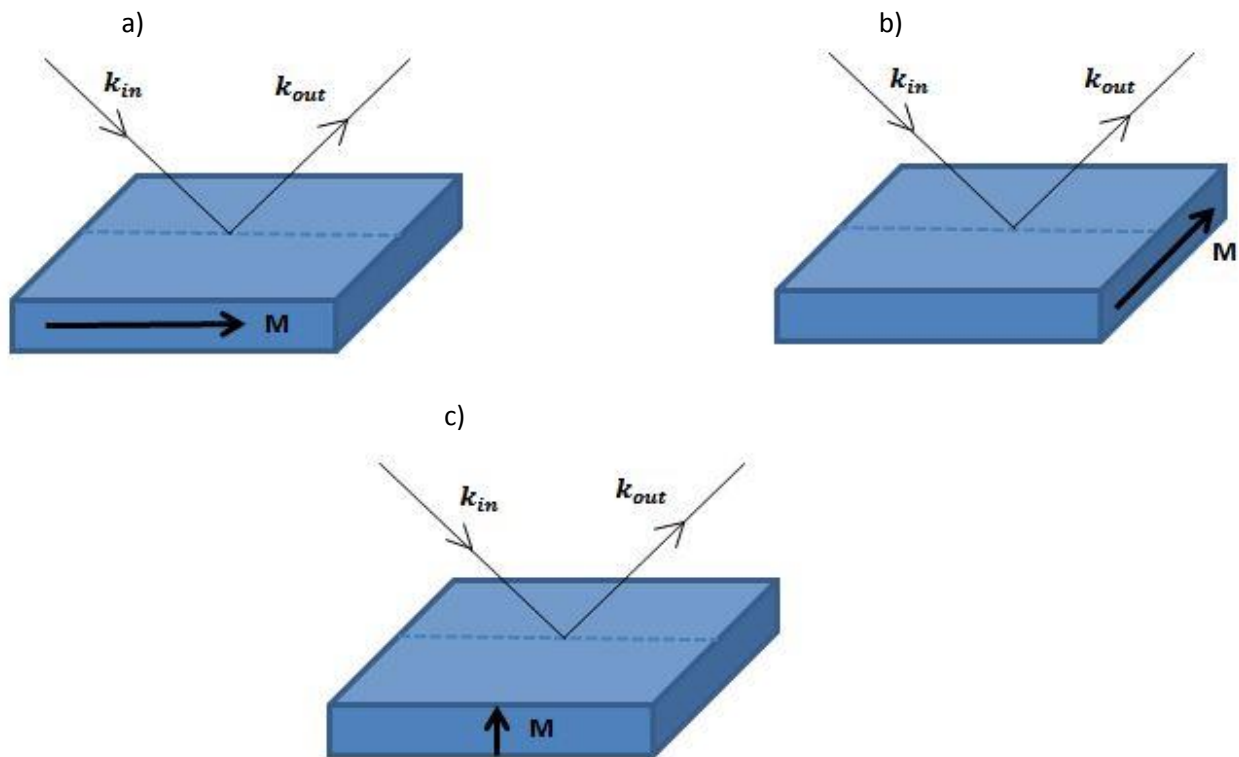
Figure 2.13: Schematics of Magneto-Optical Kerr effect (a) longitudinal, (b) transversal and (c) perpendicular geometries of the MOKE setup.

This effect was first reported by Fowler to study the domain structures of (110) silicon-iron crystals [41]. Recent advances in sensitivity and special resolution have allowed this technique to be used for characterisation of patterned nanostructures [42] [10].

2.7.2 Origin of the Magneto-Optical Kerr Effect

When polarised light of a given source is incident on a material the electric field component of the Electro-Magnetic (EM) radiation causes a motion of electrons, this motion of electrons acts as a source and re-radiates the light with equal wavefronts of the same frequency. However, when linearly polarised light is incident on a magnetic material it causes a change in the angle of the plane of polarisation.

Linearly polarised light consists of a combination of Left, LCP (Left Circularly Polarised) and right, RCP (Right Circularly Polarised) handed circularly polarised light a schematic of which is shown in Fig 2.14. Both these polarisations of light have different refractive indices in a given material. This birefringence causes each component of the polarised light to be absorbed differently in a magnetic material. The theory describing the absorptions with mathematical formulations is the Dielectric Tensor theory [43]. It describes the dielectric response of a material by considering antisymmetric (off diagonal) terms of the tensor which yield a relation between the rotation of the plane of polarisation of light and the refractive index of the material [10]. The analysis of the dielectric response of materials along with the description of the Tensor theory can be found elsewhere [44].

(a) Right and Left circularly polarised light in Phase

RCP   LCP   Linearly Polarised
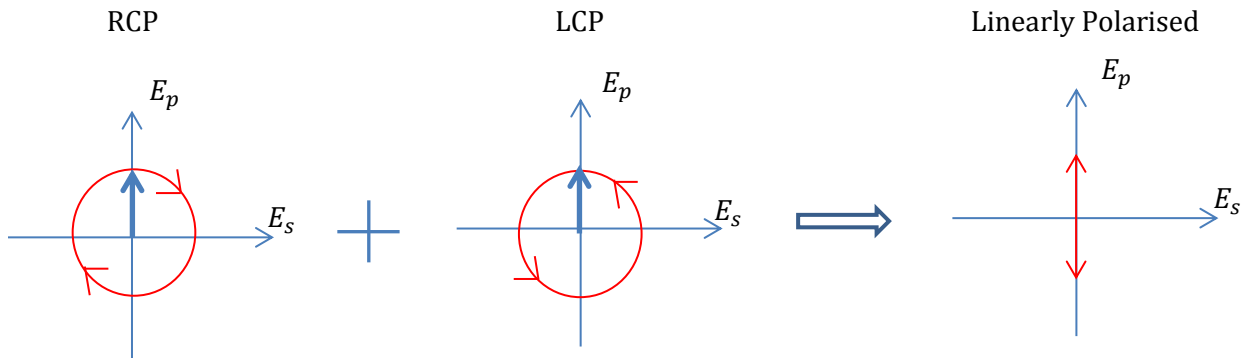
(b) Right and Left circularly polarised light out of Phase   Linearly Polarised at 45°
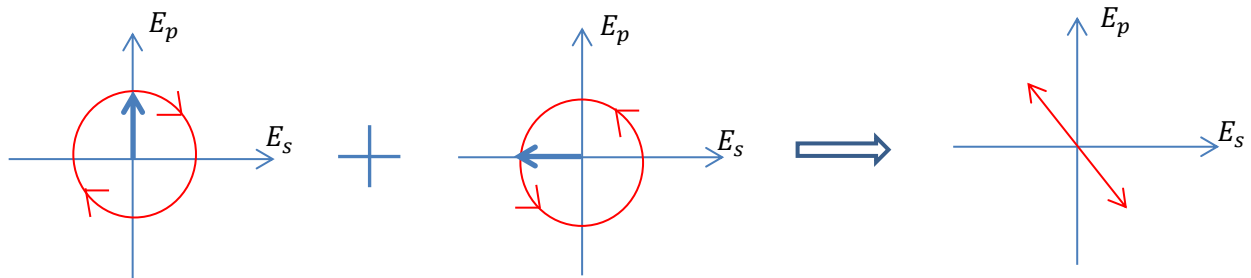
(c) Right and Left circularly polarised light differently absorbed
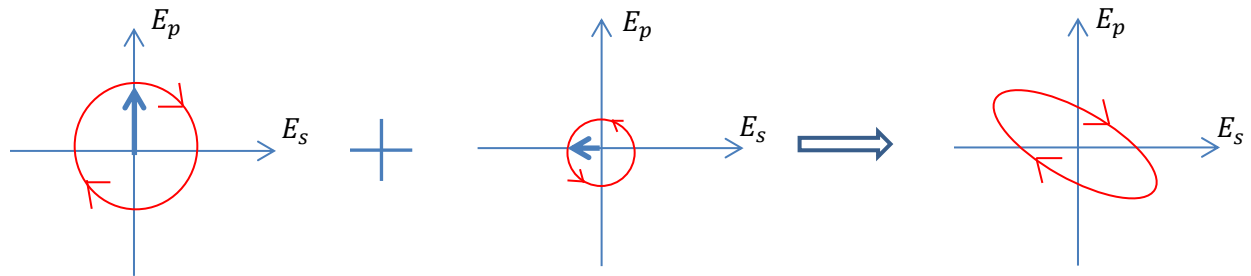
Figure 2.14: Schematic of the relative difference in the LCP and RCP light and their combination in obtaining a linearly polarised light. The elliptically polarised light is corrected using a quarter waveplate.

It can be seen from the schematic in Fig 2.14 that a linear phase offset in either of the polarisations of the incoming light will cause a rotation of the plane of polarisation. A difference in the absorption however gives rise to the ellipticity of the polarised light. The ellipticity can be removed using a $\lambda/4$ waveplate before detection. The details of the experimental setup are outlined in chapter 3 section 4.

In summary, when linearly polarised light is incident on a magnetic material it undergoes a change in its plane of polarisation and develops an orthogonally polarised Kerr component. In a simplistic set-up the polariser and analyser are almost completely crossed such that a photodiode measures a signal very close to extinction. Therefore, the photodiode is sensitive only to the changes of intensity induced by the change in the plane of polarisation. The MOKE signal is hence, only proportional to magnetisation changes and not sensitive to the moment directly. Linearly polarised light consists of *s* and *p* type polarisations. For *s* type polarised light the plane of polarisation is perpendicular to the plane of incidence where as for the *p* type polarisation the two planes are parallel [10]. The electric field vector for the incoming EM radiation is taken to be the direction of polarisation.

When light with *p* polarisation is incident on a magnetic material the interaction with the material causes it to gain a slight *s* component. It is this gain in the *s* component or also the slight change in the phase w.r.t the *p* component that gives rise to a change in the plane of polarisation of the reflected light. An example of a hysteresis curve obtained by MOKE magnetometry for a soft ferromagnetic material is shown in Fig 2.15:

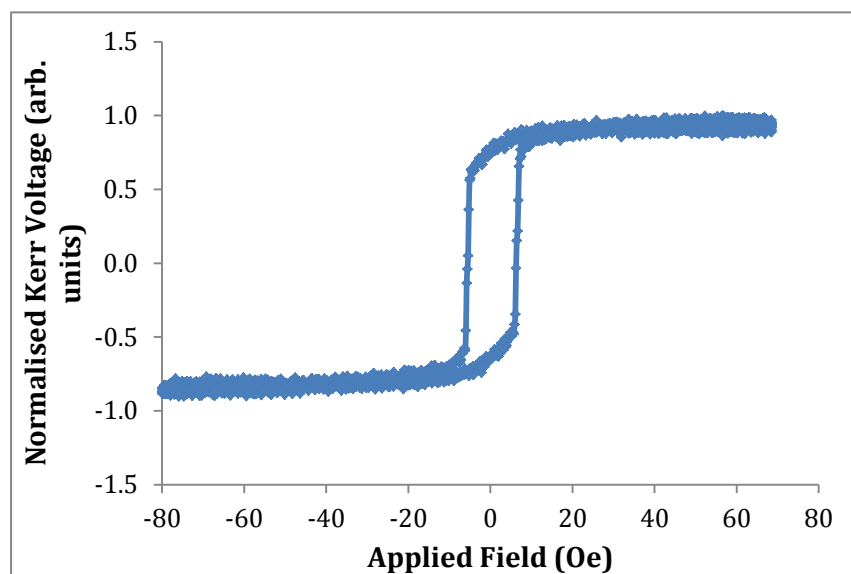Figure 2.15 :An example of a hysteresis curve for a soft ferromagnetic material measured in the plane of the film using MOKE magnetometry.

It can be seen that the change in magnetisation is observed as a change in the Kerr voltage. This response however is limited to a surface effect (skin depth) which is material dependent and is one of the drawbacks of using the MOKE to study magnetisation changes. This effect is described in the following section.

2.7.3 MOKE depth sensitivity-Penetration Depth

The MOKE effect is a surface sensitive technique determined by the electromagnetic penetration depth of the thin film under investigation. The penetration depth quantifies the drop in light penetration and defines the upper limit the MOKE effect. It is defined as the depth at which the laser intensity is attenuated to $1/e$ of its initial value due to absorption effects from the material. The skin depth of NiFe is approximately 10-15 nm [10]. In order to study the changes in magnetisation of multiple layers within in a complex multi-layered system using the MOKE, it is crucial to ensure that the laser light is not entirely absorbed and hence, attenuated at depths less than the total depth of the stack being probed. If this is the case, especially for multi-layered system such as an inverted read head sensor with a thick spacer layer, it is difficult to study the changes in magnetisation using the MOKE of the deeper buried layers such as the fixed layer in a GMR or TMR stack as attenuation means this will not be probed by the laser beam.

Other methods exist which can be used to obtain the hysteresis for a magnetic material which are not sensitive to material depth. Methods such as Vibrating Sample Magnetometry (VSM) and Super Conducting Quantum Interference Device (SQUID) magnetometry allow the study of changes in bulk magnetisation and represent the magnetisation changes within the entire volume of the sample. However, these techniques also measure the diamagnetic contributions arising from the substrate. In this respect, the surface sensitivity of the MOKE is an advantage for thin film analysis as any diamagnetic signal from the substrate can essentially be ignored and the film parameters measured more cleanly. Depending on the laser spot size MOKE allows probing of magnetisation changes over

micron-sized structures by focussing the laser to a spot on the device. However, its limitation is that the MOKE effect relies on the assumption that there is a direct correlation between the Kerr rotation and the magnetisation. The SQUID and VSM techniques provide absolute values for magnetisation which can be used to calculate different anisotropy energies outlined in section 2.2. The MOKE is usually much faster in obtaining a complete hysteresis curve as compared to the two other methods of magnetometry mentioned here.

The advantages of using MOKE magnetometry with regard to the material systems and devices being investigated in this thesis and the goal of the study outweighed its limitations and therefore this magnetometry was used to study magnetisation reversal for thin films and microstructures.

2.8 X-ray Reflectometry

Structural properties of the thin films and multilayers are important in order to understand how the structure affects the magnetisation of the corresponding materials. For example, it is well known that the signal in a GMR read head is critically dependent on obtaining the correct thickness of the spacer layer [27]. Recently it has also been found that a study of the interfaces reveal novel physics such as the Dyzaloshinskii Moriya interaction [45]. The physical operation of a device has been found to be critically dependent on the quality of the interface between two material layers. The structural properties of a material dictate the physics at the interfaces and the bulk as well as the functionality of certain devices. Therefore, it is very important to understand the internal structure of the materials involved due to the immense interest generated both in industry as well as academia. Here X-ray reflectivity was used to study structure. This section describes the theoretical framework involved in understanding the structural properties such as the roughness and thickness of thin films and describes the process of X-ray reflectometry. The experimental details are presented in chapter 3.

2.8.1 Theory of X-ray Reflectivity and Total External Reflection

It has been shown that a precise control of the interfaces can lead to novel physics [46]. Thickness dependent control of anisotropy is very important in Perpendicular Magnetic Anisotropy (PMA) based devices [47]. It therefore has become increasingly crucial to attain a thorough understanding on the thicknesses, the roughness and the densities of the thin films. X-ray reflectivity is a fast and non-invasive method of performing structural characterisation and by doing so developing an understanding of the layered structure of the material stacks being studied. This section briefly outlines the theory required to understand the structural characterisation shown later in section 4.4.

Total External Reflection

When a beam of monochromatic X-rays from a given source are incident onto a material at grazing incidence it experiences a change in the refractive index [10]. If the angle of incidence is less than a certain critical angle the beam of X-rays then undergo total external reflection and are scattered elastically [32]. By studying the scattered distribution of X-rays from the material it is possible to gain an understanding of the different structural parameters of the material under investigation.

In classical theory an electron is forced to oscillate when it encounters an oscillating electric field. Acting as a source it can absorb the X-rays and then re-emits them with the same frequency and equal wavefronts in all directions. This is elastic or Thompson scattering of the X-rays [32].

Theory of X-ray Reflectometry

There exist three assumptions in the theoretical description of the scattering of X-rays [10] [32]. The first assumption is that of the kinematical approximation, which states that once the X-rays are scattered, re-scattering of the X-rays does not occur, implying that the scattering is weak. If the

scattering is strong as is the case of diffracted intensities this approximation breaks down and one must employ dynamical theory of X-ray scattering. The second assumption is a far field approximation, which states that the X-ray detector is at a large distance compared to the depth of the sample probed uniformly. Lastly the scattered X-rays are parallel to each other and can all be described by the same wave vector K_{out}, which is the reflected wave-vector after the process of scattering has taken place.

When X-rays are incident on a material there is a certain degree of refraction which they undergo. X-rays being EM radiation are subject to Snell's laws of refraction which governs the beam path as it moves between two media of different refractive index. Snell's Law relates the angle of incidence and the angle of refraction when a beam of light passes through two mediums with different refractive indices n_0 and n_1 as [10]:

$$n_0 \cos \alpha_i = n_1 \cos \alpha_t \qquad [2.15]$$

The absolute refractive index of a material is defined as the ratio of the phase velocity of electromagnetic radiation in vacuum to the phase velocity of the electromagnetic radiation in the medium;

$$n = \frac{c}{v} \qquad [2.16]$$

The refractive index of a medium is given by

$$n = 1 - \delta + i\beta \qquad [2.17]$$

where δ and β are the dispersion and the absorption coefficients. For X-rays these coefficients are of the order of 10^{-5} [48]. Inserting these values in eq. [2.17] gives a refractive index of approximately 1×10^{-5} less than unity [$n \approx 1$]. Therefore, when X-rays are incident on a material the material appears

to be optically less dense and therefore the X-rays refract away from the surface normal as shown in Fig 2.16.
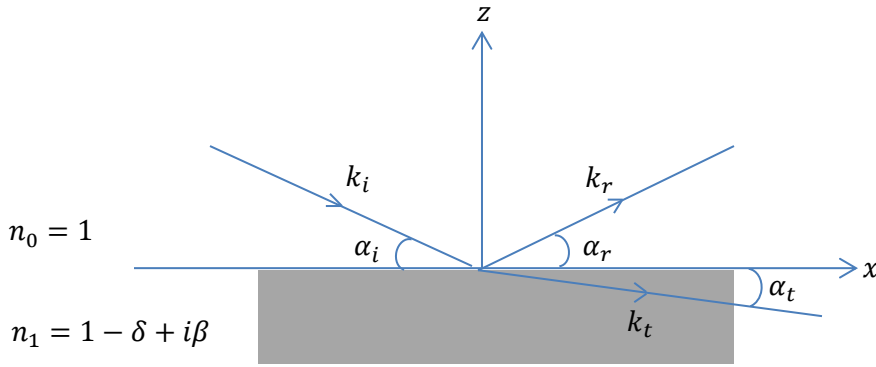
Figure 2.16: Schematic diagram showing the path of incident X-ray beam on a sample. X-rays are totally externally reflected when the angle of incident is less than the critical angle. It is assumed that they undergo elastic scattering.

At a certain incident angle the incident X-ray beam will propagate parallel to the sample surface. This angle of incidence, α_i at which the angle of transmittance α_t is 0 is known as the critical angle. Below this critical angle the transmitted wave is complex. At low grazing incidence angles the incident beam experiences total external reflection; there is only an evanescent surface electric field in the sample and the penetration depth is very low. This penetration depth increases rapidly above the critical angle, reaching a maximum value at normal incidence [32]. Total external reflection occurs when the α_i is such that the transmitted ray is completely reflected out of the sample. This occurs at a finite incident angle since the incident angle is always greater than the transmitted angle.

From Snells law if the X-ray moves from air into the material applying the cosine approximation for small angles, $1 - \frac{\alpha_c^2}{2}$ one obtains

$$\cos \alpha_c = n_1 \approx 1 - \frac{\alpha_c^2}{2} + \cdots \qquad [2.18]$$

Assuming the kinematical approximation is valid then $\beta = 0$ i.e. the absorption coefficient, since in this approximation there is no absorption. Then one can relate the critical angle and the dispersion densities as,

$$\alpha_c = \sqrt{2\delta - 2i\beta} = \sqrt{2\delta} \qquad [2.19]$$

The scattering centre's for the X-rays within the sample are the electrons and therefore δ is a good estimate for the electron density of the material under inspection.

Depending on the roughness of the material X-rays are scattered coherently or diffusively from the surface. There are also reflections from layers present beneath the surface. Each interface gives rise to surface scattering, for a single layer the interface is between the substrate-material and material-vacuum/air gives rise to interference fringes. Consider the case where X-rays penetrate through materials with three different refractive indices n_1, n_2, and n_3 represented as shown in Fig 2.17.
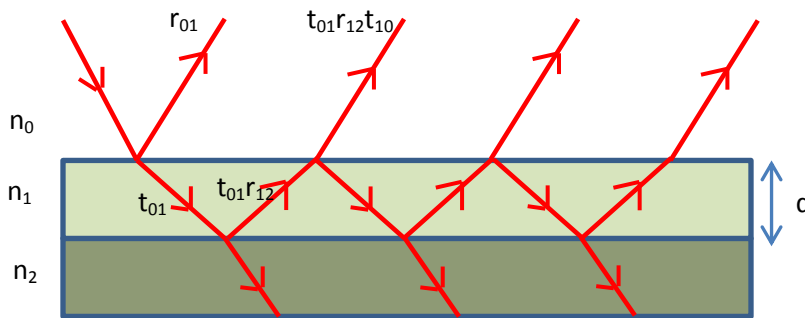
Figure 2.17: Schematic illustrating X-ray scattering from multiple surfaces undergoing transmission or reflection.

The total reflection in this situation is the initial reflection r_{01} along with every successive transmittance from each interface. Therefore the total reflection from the film stack can be written as explained in [49] as

$$r_{stack} = r_{01} + t_{01}r_{12}t_{10}p^2 + t_{01}r_{12}r_{10}r_{12}t_{10}p^4 + \cdots \qquad [2.20]$$

here p is the phase factor added to the reflectivity term to account for the relative path difference given by;

$$p^2 = \exp(iqd) \qquad [2.21]$$

where q contains the incoming wavevector and the angle of incidence. Eq.[2.20] forms a geometric series which can be simplified using Fresnel's equation [49] to obtain the net reflectivity as:

$$r_{stack} = r_{01} + \frac{t_{01}r_{12}t_{10}p^2}{1-r_{10}r_{12}p^2} = \frac{r_{01}+r_{12}p^2}{1+r_{01}r_{12}p^2} \qquad [2.22]$$

A simulated reflectivity measurement for 20 nm of Pt thin film is shown in Fig 2.18.

Figure 2.18: Measured (Blue) and simulated (Red) X-ray Reflectometry for 20 nm Pt on thermally oxidised Si substrate.

As one can observe from the simulation shown in Fig 2.18 it is clear that the intensity drops by a few orders of magnitude after a particular angle and then oscillates with decreasing intensity with every oscillation. These oscillations are called Kiessig fringes [48] and the angle at which the first

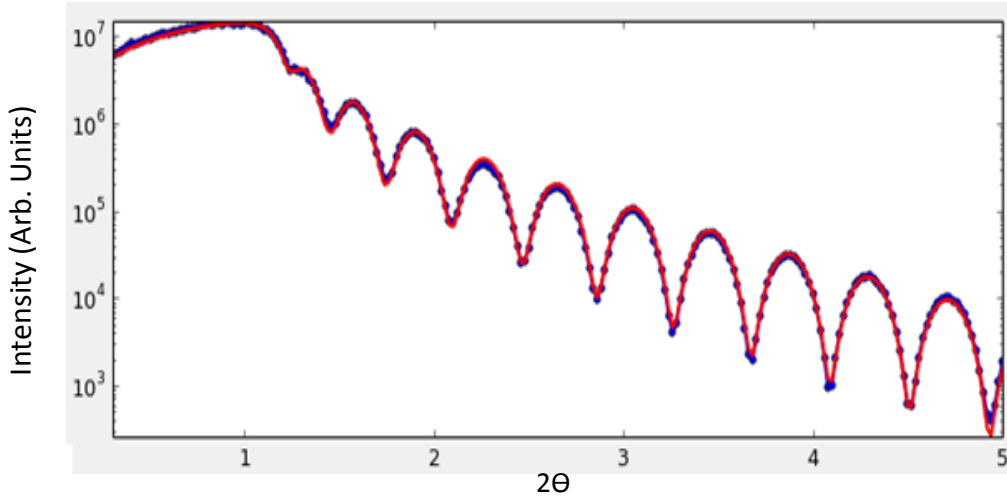drop in intensity is observed is called the critical angle. The Kiessig fringes arise as a result of the interference between the scattered X-rays from each interface. As can be seen from eq. [2.19], the higher the critical angle for a material the higher is the electron density. Using [50] for electron densites of Fe and Ni, for $Ni_{81}Fe_{19}$ with an electron density of 2.4920 electrons/$Å^3$ the Kiessig fringes originate from the scattering of the X-rays from the top and the bottom interface. The larger number of oscillations for a given range of angles the thicker the material being investigated, as more reflections arise with increasing thickness of layers or scattering sites. Grazing Incidence X-ray Reflectometry (GIXR) is an important tool not only for estimating the thicknesses of different thin films but also their roughness. The rate at which the intensity decreases with increasing incident angle provides an estimate on the interface width or the roughness of the film. For an extremely rough surface the scattering would be very diffuse and the specular reflection intensity will drop significantly with a slight change in the angle of incidence. Since the GIXR is sensitive only to the average change in refractive index along the depth z of the sample it is not possible to distinguish between a topologically sharp interface with large undulations or flat, but a chemically graded interface. It is the interface width which is finally obtained from fitting of simulations to the reflectivity.

The two pre-requisites to fully appreciate the experimental results are firstly, an understanding of the theoretical background of the presented work and secondly, a detailed description of the experimental methods used to obtain the results. An outline of the theoretical framework has been described in chapter 2 and the different investigative techniques, are outlined in the following chapter.

Chapter 2- References

[1] Griffiths, D. J., '*Introduction to Quantum Mechanics second edition',* Pearson Education, (2014) pp. 207–210

[2] Honda, K., and Kaya, S., '*On the magnetisation of single crystals of iron*' Scientific Reports of Tohoku University **15** (1926) 721-753

[3] Honda, K., and Kaya, S., '*On the magnetisation of single crystals of iron*' Scientific Reports of Tohoku University **15** (1928) 639-663

[4] Omar, M.A., '*Elementary Solid State* Physics' Addison-Wesley Company, Philippines (1975)

[5] Kronmuller, H., and Fahnle, M., '*Micromagnetisation and the microstructure of ferromagnetic solids*' Cambridge University Press, Cambridge (2003)

[6] Bozorth, R. M., '*Directional ferromagnetic properties of metals*' Journal of Applied Physics **8** (1937) 575-588

[7] Bozorth, R. M., '*Ferromagnetism*', Van Nostrand, London (1951)

[8] Rossiter, P.L., '*The Electrical Resistivity of Metals and Alloys*' Cambridge Solid State Series, pp 213

[9] Chi, T.C., '*The Electrical Resistivity of Alkali Elements*' Journal of Physics and Chemistry Reference Data **8** (1979) 2

[10] Bogart, L.K., (2010) '*An Investigation of the Structure, Pinning and Magnetoresistance of Domain Walls in Ni81Fe19 Planar Nanowires*' , Durham theses, Durham University. Available at Durham E-Theses Online: http://etheses.dur.ac.uk/507/

[11] Mott, N.F., '*The Electrical Conductivity of transition metals*' Proceedings of the Royal Society of London A **153** (1936) pp 699-717

[12] Fert, A., *et al.* '*Electrical Resistivity of Ferromagnetic Ni and Fe based alloys*' Journal of Physics F: Metal Physics **6** (1976) 5

[13] Shinjo, T., '*Nanomagnetism and Spintronics* 'Second Edition, Elsevier B V, London (2014)

[14] O' Handley, R.C., '*Modern Magnetic Materials: Principles and Applications*' John Wiley & Sons, New York (2000)

[15] Rowan-Robinson, R.M, *et al.*, '*Enhanced electron-magnon scattering in ferromagnetic thin films and the breakdown of the Mott two-current model*' Physical Review B **90** (2014) 104401

[16] Tokaç, M., *et al.*, '*Interfacial contribution to thickness dependent in-plane anisotropic magnetoresistance*', AIP Advances, **5**, (2015), 127108

[17] McGuire, T.R., and Potter, R. I., '*Anisotropic magnetoresistance in ferromagnetic 3d alloys*' IEEE Transactions on Magnetics **11** (1975) 1018-1040

[18] Smit, J., '*Magnetoresistance of ferromagnetic metals and alloys at low temperatures*' Physica **16** (1951) 612-627

[19] Shi, D., Aktas, B., Pust, L., Mikailov, F., '*Nanostructured Magnetic Materials and Their Applications*' Springer, Germany (2001)

[20] Smit, J., '*Magnetoresistance of ferromagnetic metals and alloys at low temperatures*' Physica **16** (1951) 612-627

[21] Fert, A., Campbell, I.A., '*Two Current conduction in Nickel*' Physical Review Letters **21** (1968) 1190

[22] Thompson, S.M., '*Topical Review: The discovery, development and future of GMR: The Nobel Prize 2007*' Journal of Physics D: Applied Physics **41**(2008) 093001

[23] Baibich, M. *et al.,* '*Giant Magnetoresistance of (001)Fe/(001)Cr Magnetic Superlattices*' Physical Review Letters **61** (1988) 2472

[24] Grünberg, P. *et al.,* '*Layered Magnetic Structures: Evidence for Antiferromagnetic Coupling of Fe Layers across Cr Interlayers*' Physical Review Letters **57** (1986) 2442

[25] Hirota, E., Sakakima, H., Inomata, I., '*Giant Magneto-Resistance Devices*' Springer, New York (2002)

[26] Marrows, C.H. (1997), '*Indirect Exchange Coupling in Sputtered magnetic multilayers',* The University of Leeds, PhD Thesis

[27] Parkin, S.S.P., '*Systematic variation of the strength and oscillation period of indirect magnetic exchange coupling through the 3d, 4d, and 5d transition metals*', Physical Review Letters, **67**, (1991), 3598

[28] Parkin, S.S.P., *et al.,* '*Oscillations in exchange coupling and magnetoresistance in metallic superlattice structures: Co/Ru, Co/Cr, and Fe/Cr*', Physical Review Letters, **64**, (1990), 2304

[29] Fert, A., and Campbell, I.A., Journal Physique, **32**, (1971), 46, Suppl.C1

[30] Wasa, K., '*Handbook of Sputter Deposition Technology: Fundamentals and Applications for Functional Thin Films, Nano-Materials and MEMS*', Elsevier, U.K. 2012

[31] Frey, H., '*Handbook of Thin Film Technology*', Springer, Germany 2015

[32] Eastwood, D.S., (2009) '*Grazing Incidence X-ray Scattering from Magnetic Thin Films and Nanostructures*', Durham theses, Durham University. Available at Durham E-Theses Online: http://etheses.dur.ac.uk/27/

[33] Gantz, J., and Reinsel, D., '*The Digital Universe Decade-Are you Ready ?*', IDC Analyse the Future: EMC corporation, May (2010)

[34] Rater, D and Ratner., M.A., '*Nanotechnology: A Gentle Introduction to the Next Big Idea*', Pearson Education Inc., New Jersey (2003)

[35] Barth, J.V., *et al.,* '*Review Article Engineering atomic and molecular nanostructures at surfaces*' Nature **437**, (2005), 671-679

[36] Atkinson, D., '*Patterning nanostructures to study magnetization processes*', Journal of Physics: Conference Series, **17**, (2005), 33-39

[37] Rothschild, M., *et al.,* '*Recent Trends in Optical Lithography*', Lincoln Laboratory Journal, **14**, (2003), 2

[38] Faraday, M., '*On the magnetisation of light and the illumination of magnetic lines of force*' Philosophical Transactions of the Royal Society, **136**, (1846), 1-20

[39] Kerr, J., '*On rotation of the plane of polarisation by reflection from the pole of a magnet*' Philosophical Magazine, 3, (1877), 321-343

[40] Kerr, J., '*On reflection of polarised light from the equatorial surface of a magnet*' Philosophical Magazine, **5**, (1877), 161-177

[41] Fowler, Jr., C. A., and Fryer, E. M., '*Magnetic domains on silicon iron by the longitudinal Kerr effect*' Physical Review, **86**, (1953), 426

[42] Allwood, D.A., *et* al., '*Magneto-optical Kerr effect analysis of magnetic nanostructures*' Journal of Physics D: Applied Physics, **36**, (2003), 2175-2182

[43] Hubert, A., and Schäfer, R., '*Magnetic domains: the analysis of magnetic microstructures*' Springer-Verlag, Berlin (2000)

[44] Qiu, Z.Q., and Bader, S.D., '*Surface magneto-optical Kerr effect*' Review of Scientific Instruments, **71**, (2000), 1243-1255

[45] Cho, J., '*Thickness dependence of the interfacial Dzyaloshinskii–Moriya interaction in inversion symmetry broken systems*', Nature Communications, **6**, (2015), 7635

[46] Miron, I.M., *et al.,* '*Fast current-induced domain-wall motion controlled by the Rashba effect*', Nature Materials, **10**, (2011)

[47] Oh, Y-W., *et al.,* '*Interfacial perpendicular magnetic anisotropy in CoFeB/MgO structure with various underlayers*', Journal of Applied Physics, **115**, (2014), 17C724

[48] Kiessig, H., '*Interferenz von Röntgenstrahlen an dünnen Schichten*' (Interference of x-rays in thin layers) Annalen der Physik, **402,** (1931), 715-725 & 769-788

[49] Als-Nielsen, J., and McMorrow, D., '*Elements of modern X-ray physics*' Wiley, Chichester (2001)

[50] http://www.kayelaby.npl.co.uk/chemistry/3_1/3_1_2.html Accessed 4th February 2016

[51] Singulus Technologies AG - Press release 'SINGULUS TECHNOLOGIES will deliver a TIMARIS deposition system to Singapore's Data Storage Institute' 29th September (2010)

|Chapter 3

Experimental and investigative

methods

3.1 Introduction

The various experimental techniques used in this study are described within this chapter. This chapter explains the techniques and investigative methods used to achieve the aim of the thesis. In order to use the GMR as a tool to measure magnetisation dynamics in a nanostructure geometry, it is firstly crucial to be able to prepare multilayer thin films with pseudo-spin valve structure with a significant GMR to demonstrate a proof of concept. In order to characterise the magnetic properties and study switching of the two individual layers MOKE magnetometry was used and is explained in this chapter. Due to the inverse square dependence of the spacer layer [1] thickness on the GMR value as demonstrated in section 2.5.1 the quality of films with regard to interfacial roughness is critical to this study. To that end experimental methods characterising structural properties are outlined herein. Finally the Magneto-Resistance experimental technique is explained.

3.2 Preparation of thin films

As technology progresses there are new and more efficient methods of producing nanoscale thin films and devices [2]. Pseudo spin-valves comprises of multiple material layers stacked together. In order to grow such multi-layer different target materials must be present in the same deposition system. Sputtering is a technique used widely in the industry due to 1) high throughput 2) high reproducibility. It is possible to produce high quality thin films uniformly on 300 mm wafers [3]. The processes can be automated which results in reproducibility and high throughput. For this study the films were grown manually using sputtering in a multi target sputter module which is a very versatile system for research. Various steps taken along with the description of the film growth process are described in the sections below.

3.2.1 Substrate preparation

Each sample used in this work was prepared on thermally oxidised silicon substrates. This substrate had approximately 500 μm of SiO_2 which provided an amorphous substrate for subsequent depositions. Each substrate was cleaved in two geometries used for different experimental investigations. A 10x10 mm substrate was cleaved for MOKE magnetometry and X-ray reflectivity measurements. A 5x22 mm substrate was cleaved for conducting Magneto-Resistance measurements. This was slightly larger than the shadow mask used for the deposition outlined in section 3.2.3. Prior to deposition each substrate underwent sonication in a chemical bath initially with acetone for 5 mins and then in a separate beaker with Isopropan-2-ol (IPA) for further 5mins. The chemical cleaning was used to remove any organic impurities and provide a clean surface for deposition. If the IPA is allowed to evaporate naturally it is possible that a residue of the solvent is left behind to which hydrophilic impurities might attach chemically. To prevent this, IPA was removed from the substrate by dry nitrogen cleaning using a N_2 gun at glancing incidence.

3.2.2 Sputter Deposition

Each film was prepared using D.C. and R.F. magnetron sputter deposition using a newly installed Mantis Qprep™ modular deposition system. The sputter system is shown in Fig 3.1. The sputter system consists of two chambers, a load-lock and the main deposition chamber. The samples were transferred from the load-lock to the main chamber via a magnetically coupled Load Transfer Arm (LTA).

Each substrate underwent the cleaning process described above. The sample transfer to the main chamber was done using an off axis z stage translator which was used to load the sample in the sample housing in the main chamber.
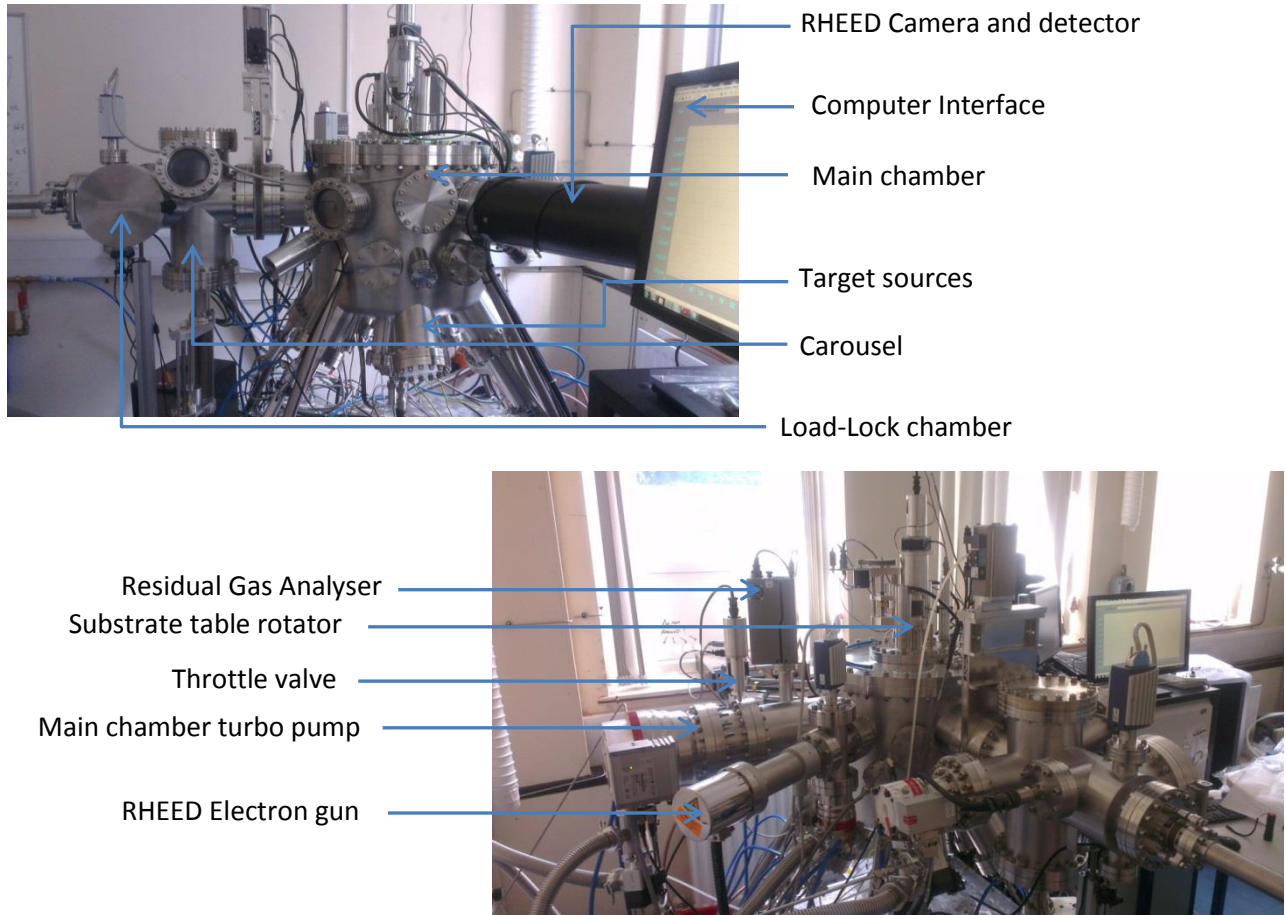

Figure 3.1: Q-prep Mantis deposition system detailing various components

The load-lock housed a cassette carousel which was able to load up to 5 substrates in a single pump down cycle. Once the substrates were loaded they could be transferred into the deposition chamber which, was separated from the load-lock via a UHV gate valve. This drastically increased the throughput of the system and the gate valve allowed sample transfers without venting the main chamber. The main chamber consisted of 5 magnetron sputter guns all positioned at an angle to the substrate. The chamber allowed up to three targets to be co-sputtered simultaneously with the aid of two D.C. and one R.F. power supply. Each magnetron was housed with internal gas inlets and water cooling. The individual gas lines to each magnetron allowed for the formation of a very uniform plasma generated at the target surface. Due to the gas being injected into the chamber from each magnetron source individually, the plasma formed was very uniform due to the high density of Ar flux immediately above the target. This also allowed for each target to be co-sputtered with different individual gas partial pressures. Each target was covered with a shutter to prevent contamination during single cathode sputtering. A separate substrate shutter prevented premature deposition during pre-sputtering of the target and was also used to control the thickness of the sputtered film. The rate of the target was determined in-situ using a Quartz Crystal Monitor (QCM) prior to deposition of the film. The QCM is attached to a movable arm which records the rate directly below and at the centre of the substrate. For each cathode position the QCM was calibrated with its respective geometrical tooling factors. These factors take into account the basic geometry of all 5 cathodes with respect to the substrate position which affect the deposition rate.

The substrate is housed with a SiC resistive heater capable of reaching 700 °C. Attached to the main chamber is a Residual Gas Analyser (RGA) and a Reflective High Energy Electron Diffraction system (RHEED) used for checking partial pressures and for monitoring the growth of epitaxial films respectively. The Turbo Molecular Pump has attached a throttle valve which allows for an additional degree of freedom to optimise growths at different pressures without changing the gas flows. This UHV sputter system when baked out with an internal heater is able to achieve pressures below

2x10^{-9} mtorr and therefore along with the above mentioned tools it is well suited for deposition of complex layered systems. Thus all films grown in this study were deposited using the above mentioned system. Sample substrates were scribed from a 525 μm thick single side polished silicon substrates with 1kÅ thermal oxide coating and special masks were used as shadow masks, in the deposition of the films studied in this work.

3.2.3 Substrate holders and deposition Masks

In order to perform accurate Magneto-Resistance (MR) measurements outlined in the following section 3.3 a defined current path with known current densities was needed. To achieve this, a shadow deposition mask as shown in Fig 3.2(b) was developed and used.
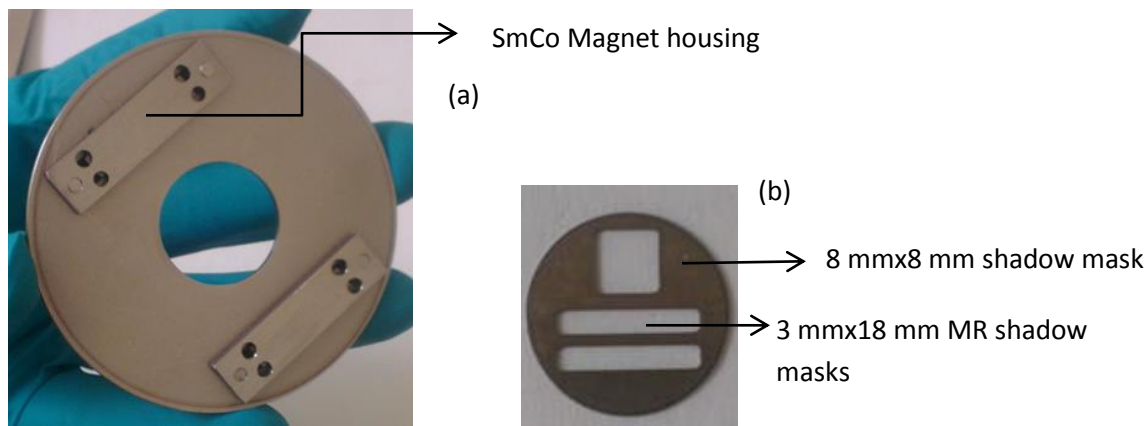
Figure 3.2: (a) Sample holder used for application of in –plane field during deposition (b) Shadow masks used for transport, structural and magnetic characterisation

The mask is a 1 inch stainless steel circular frame which consists of a 3 mm x 18 mm rectangular shaped mask for depositing stripes of material for MR measurements and an 8 mm x 8 mm square shaped mask for MOKE and X-ray reflectivity measurements. Substrates were scribed into 5 mm x 22 mm and 10 mm x 10 mm pieces and secured to the masks using UHV Kapton™ adhesive tape. This 1 inch mask was then mounted on a molybdenum holder and transferred to the load-lock chamber of the sputter deposition system described in 3.2.2.

Another sample holder was designed to be used with the same mask shown in Fig 3.2. This holder was designed with two cavities which housed two permanent magnets, Fig 3.2(a). This allowed for application of field during depositions of materials to create field-induced anisotropy during film deposition.

3.2.4 Nanostructure Design & Lithographic Patterning

Both thin films and microstructure devices were investigated in this study. After developing and characterising the thin films and understanding the effects of structure on the measured Magneto-Resistance behaviour. The thin films were patterned into microstructured devices of certain geometry. The design of the microstructures is shown in Fig 3.3.
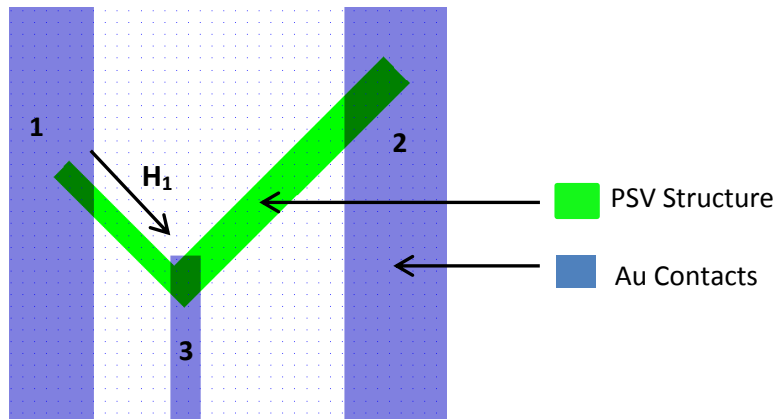
Figure 3.3: Schematic of the 3 point L shaped microstructure (Green) with 3 Au contacts (Blue). The three terminals allows current to be passed through each wire individually or through the entire structure, by tuning the material properties and the direction of field. The three terminal device is designed to study DW dynamics.

Initially the material configuration and then microstructures were designed such that they would facilitate the use of both GMR and AMR to study magnetisation dynamics. The microstructures themselves were designed to have three vertices. Each vertex was connected to a gold contact pad This L-shaped device geometry allowed the study of current flow with respect to field applied along different directions. As it is elaborated in chapter 2, the anisotropic change in resistance which

manifests as the AMR depends solely on the angle between the current flow direction and the magnetisation of the material. The GMR effect on the contrary does not depend on the current direction, it depends on the relative magnetisation between the indirectly coupled magnetic materials. The L-shaped, three vertex device was used to study both these effects. For example, when current is allowed to pass between contact pads 1 and 3 and a saturating field H_1 is applied along the direction of wire 1 this would result in a high resistance value with respect to the AMR contribution to the Magneto-Resistance change in wire 1 and a low resistance value due to the perpendicular orientation of the current direction with respect to the magnetisation in wire 2. The field H_1 is the saturating field required to align the magnetic moments parallel to external field in wire 1. The shape anisotropy present in wire 2 will prevent the magnetisation from aligning parallel to the field applied along wire 1. Also depending on the indirect exchange coupling between the two ferromagnetic layers it is possible to obtain a difference in resistance contribution from the Giant Magneto-Resistance effect. Together these Magneto-Resistance effects and the changes in resistances could be used to study the dynamics of the magnetic free layer. Another contact pad is connected to the device which allows the measurement of Magneto-Resistance of individual wires.

3.3 Magneto-Resistance of thin films

In order to study the magnetisation dynamics of microstructures using Magneto-Resistance effects, it is important to understand the GMR and AMR contributions and their dependence on individual material properties of the associated layers. The Magneto-Resistance of thin films was measured using a room temperature D.C. 4 point probe technique. The 4-point technique was used to avoid problems with contact resistance, which can have a significant contribution when used in a 2-point contact approach. The thin films were prepared as described in section 3.2. A schematic of the experimental set-up and the sample holder are shown in Fig 3.4.
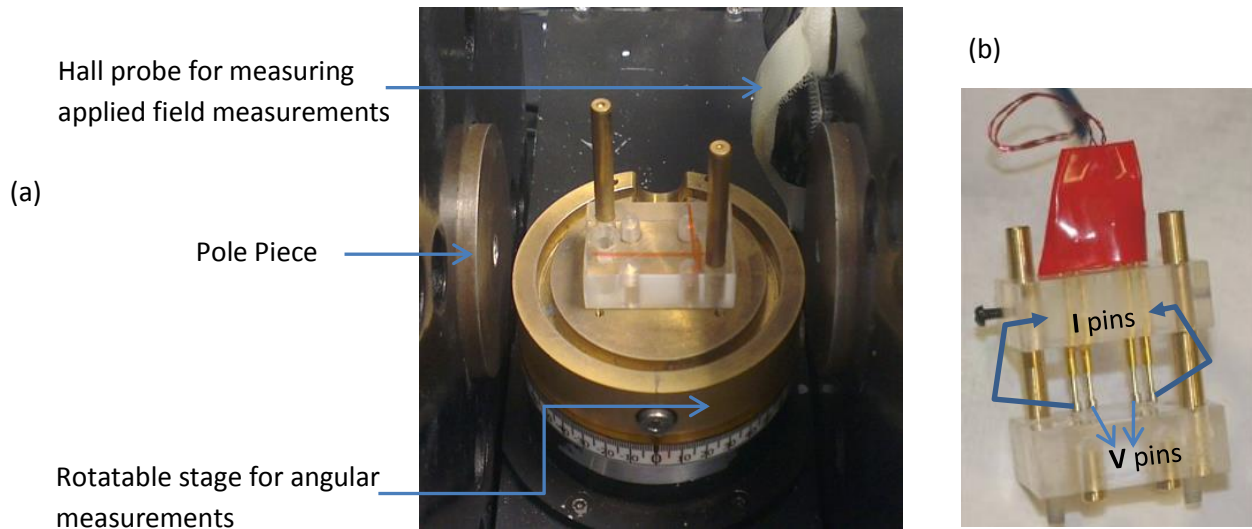
Figure 3.4:Room temperature Magnetoresistance shown. (a) The experimental setup used for the Magneto-Resistance measurements performed during this study. (b) The thin film sample holder used to measure the Magneto-Resistance shown with the 4 point spring probes

The four contacts were gold plated and spring loaded. Once the sample was placed on the holder, the contacts were secured in place using a ceramic screw. As described in section 2.5.1 for a GMR device three effective layers are needed. Two ferromagnetic layers and a medium through which the spin-polarised conduction electrons propagate are needed, which results in the indirect exchange coupling [4-7] i.e. a spacer layer. However, the aim of this study is not to realise a high GMR ratio but to study the magnetisation dynamics of the free layer using the GMR and AMR effects in combination. A Synthetic Anti-Ferromagnet (SAF) or an antiferromagnetic pinning increases the complexity of the material stack which in a proof of concept is not required. Therefore, a Pseudo Spin-valve (PSV) was engineered [8]. In a PSV, the FM pinned layer is not strongly pinned [9]. The GMR effect is created by a pseudo-pinned layer. This can be done by choosing a free layer and a pseudo-pinned layer of materials which have different coercivities. Therefore cobalt was used as a pinned layer and NiFe (Permalloy) used as a free layer for the two FM materials required in a GMR device. One may also use the same material for both the pseudo-pinned and the free layer, as done by M. Jergel *et al* [10].There still exists a difference in the relative coercive fields due to the different

thicknesses used. The pinned layer in this case is thicker than the free layer. The different coercivities imply different switching fields.

For this study a pseudo-spin valve with Co as the pinned layer and a $Ni_{81}Fe_{19}$ free layer was used. The two FM materials are separated by a copper spacer layer. The Cu layer thickness was varied to adjust the coupling strength between the free and pinned layers. Cu was chosen because of the strong coupling strength exhibited, and a minimum strain at the Co/Cu interface due to the low lattice mismatch (approx. 2%) [11-13]. The Co/Cu interface, has a low lattice mismatch which facilitates the growth of Cu on Co [12]. The PSV used is visualised in the schematic shown in Fig 3.5:
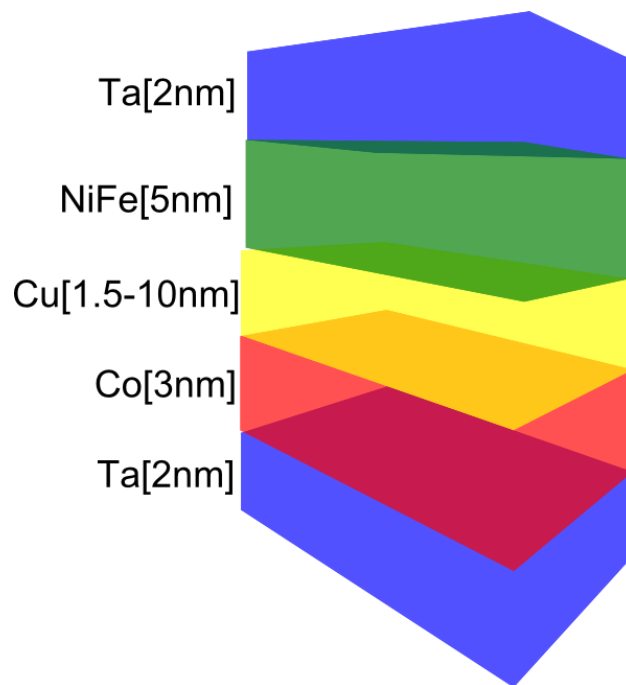
Figure 3.5: Schematic of the pseudo-spin valve developed here to study magnetisation dynamics in the NiFe free layer.

Ta was used as a buffer layer which promoted fcc(111)[hcp(0001)] textured growth in Co [14]. The film was also capped with 2 nm of Ta to prevent oxidation.

The Magneto-Resistance was measured in the Current In-plane (CIP) geometry for thin films of Ta/Co/Cu(t)/NiFe/Ta. The D.C. in line four probe technique shown in Fig 3.4(b) was used to apply

in-plane current using the outer probes and measure the voltage along the inner probes. Current was applied using a Keithley sourcemeter and a Keithley Nano-Voltmeter was installed to get more precise voltage readings. The sample stage was connected to a stepper motor which allowed for angular scans by rotating the sample 360 degrees. The sample was placed between two electromagnet pole pieces capable of generating fields up to 800 Oe connected to a Kepco power supply. A Hall probe was used to measure the applied field. The sample was initially saturated in a high positive magnetic field and the field was gradually reduced at regular intervals until it reached negative saturation value at which point the field was reversed and the measurements were repeated until positive saturation, this constituted a full-field constant-angle scan. The magnet was controlled by National Instruments Lab-View software developed in-house. The Magneto-Resistance software was designed to perform the following steps. At each user defined field value, the Kepco applied a current to the electromagnet which was followed by the Hall probe detecting the true field value, if this detected field value was within a tolerance level (defined in the software code) the field was set for the measurement and current was applied. The resistance was calculated via the voltage measurement for the particular current. However, if the field was not within the defined tolerance a calibrating current was requested from the Kepco to set the desired field value which was checked again. This process was repeated for each field step and was implemented in the software especially for lower field values. For lower fields of a few Oersteds it becomes difficult to apply the set field value as these fields are within the remanence of the electromagnet. The applied field values recorded were fields detected by the Hall probe.

Such field scans were performed with the current applied along the sample and parallel to the external field in the plane of the sample. The sample was then rotated by 90° and the Magneto-Resistance was measured with the current now applied perpendicular to the external field also in the plane of the sample. Thus the transport properties for each thin film with different spacer layers were evaluated.

3.4 Magneto-Optical Kerr effect Magnetometry

In order to understand the independent switching of each layer of the pseudo spin-valve stack it is necessary to perform magnetometry on the full film samples. This allows us to obtain an understanding on how the magnetisation of each layer changes with respect to external applied field. There exist different methods to understand magnetic properties of thin films. Some examples are the Superconducting Quantum Interference Device (SQUID), the Vibrating Sample Magnetometer (VSM) and MOKE magnetometer. Extraordinary Hall Effect measurements can also be used to obtain the anisotropy field values along the hard axis [15]. For the material system studied here MOKE was the preferred method of choice for several reasons. MOKE magnetometry is fastest in magnetic characterisation of films compared with SQUID and the VSM. It is possible to use a focussed laser spot approximately 5 µm in diameter which allows the study of switching individual regions of the device.

The MOKE setup used for this study is an integrated system which allows for optical and magnetic characterisation without repositioning of the sample. A schematic of the optics involved in the MOKE setup is shown in Fig 3.6.
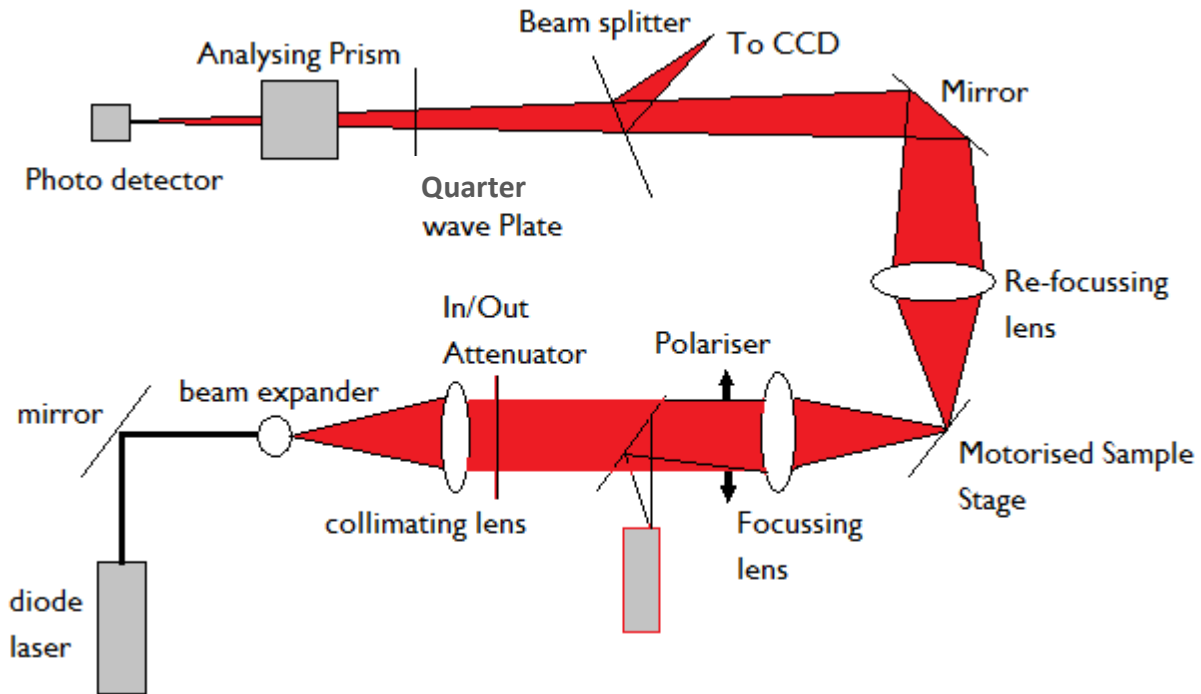
Figure 3.6: A schematic setup for the Magneto-Optical Kerr Effect set-up used in this study for magnetic characterisation

A diode laser was used at 643 nm with an attenuated output of 5 mW (class 3R) as a source. The beam passed through a beam expander and then through a collimator that produced parallel beams at the sample. The beam is polarised using a Glan-Taylor polarising prism with a small extinction ratio in order to enhance the beam polarisation ratio. The sample is mounted on an XY translational stage at 45° to the incoming beam. The spot size is therefore, elliptical along the surface of the sample. The reflected light is then focussed using the refocussing lens. The beam path is split using a beam splitter, in order to allow for optical imaging of the nanostructures a CCD camera is placed in the beam path. The laser light is focused so that the central intensity of the beam spot is high and the higher order modes are not significantly visible. In order to remove any elipticity of the linearly polarised light and any phase difference between the orthogonally reflected amplitudes, a quarter-wave retardation plate is inserted in the beam path. After this a Glan-Taylor analysing prism and a photodiode are used to obtain the Kerr signal from the reflected light. White light was introduced into the beam path using a pellicle between the collimator and the polariser. This was used to

initially locate the microstructures and focus the laser spot on the structures. A dichroic partial mirror was used to protect the CCD camera from over exposure from the laser light. The white light was switched off when the magnetic measurements were performed.

The sample was prepared as described in section 3.2.1. The 10 x 10 mm^2 sample was loaded on the sample holder and mounted on the XY stage. The measurement was performed by first adjusting the quarter wave plate and the analyser so as to obtain the best extinction of the Kerr signal which was detected by reading the photo-voltage from the photo diode. Then the analyser was adjusted by a small amount away from extinction to detect polarisation changes in the intensity of the light at the photodiode. The magnetic field was applied using an in-plane iron core air spaced electro-magnet powered by a Kepco BOP205M. A waveform generator was connected to the Kepco to produce sinusoidal waveforms. The laser spot for each sample was focused at 4 different locations for full film samples to obtain hysteresis curves from different regions of each sample. Once the magnetic characterisation was completed, X-ray reflectivity was performed on the sample to understand the structural properties. The experimental set-up used for the same is outlined below

3.5 X-ray reflectivity and structural characterisation

The periodicity of the oscillatory coupling through Co/Cu multilayers has been found to be 12 Å [16]. This requires precise control over structural properties of the pseudo spin-valves studied here to ensure the desired transport and magnetic properties in the devices. There are different methods used for structural characterisation such as Transmission Electron Microscopy (TEM), X-ray Diffraction (XRD), and X-ray reflectivity (XRR) each method provides a range of different information on the structural properties of the sample. For example TEM allows atomic scale resolution to image the atomic layers [17]. Diffraction provides information on in-plane or out-of-

plane crystal ordering on the material stack and what are the phases of the materials present in the stack. Reflectivity provides information on the roughness and estimates the thickness of each layer. There also exist related characterisation tools such as X-ray florescence used to provide element specific information about the depth of the sample. These facilities require high intensity X-ray sources with a high brilliance and therefore are available at beamline facilities spread globally [18]. The method used to perform structural characterisation for this work was X-ray reflectivity. XRR provides information on the thickness, roughness and the electron density of the different layers in a material system.

XRR was performed using a Bede D1, 2-circle diffractometer at room temperature. The X-rays were produced using a sealed tube containing a water-cooled copper cathode using an X-ray generating power of 1.6 kW. Copper K_α X-ray radiation was produced at 1.54 Å. A 10x10 mm² substrate was prepared and multilayer films were deposited as outlined in section 3.2.1. A schematic of the experimental setup is shown in Fig 3.7.
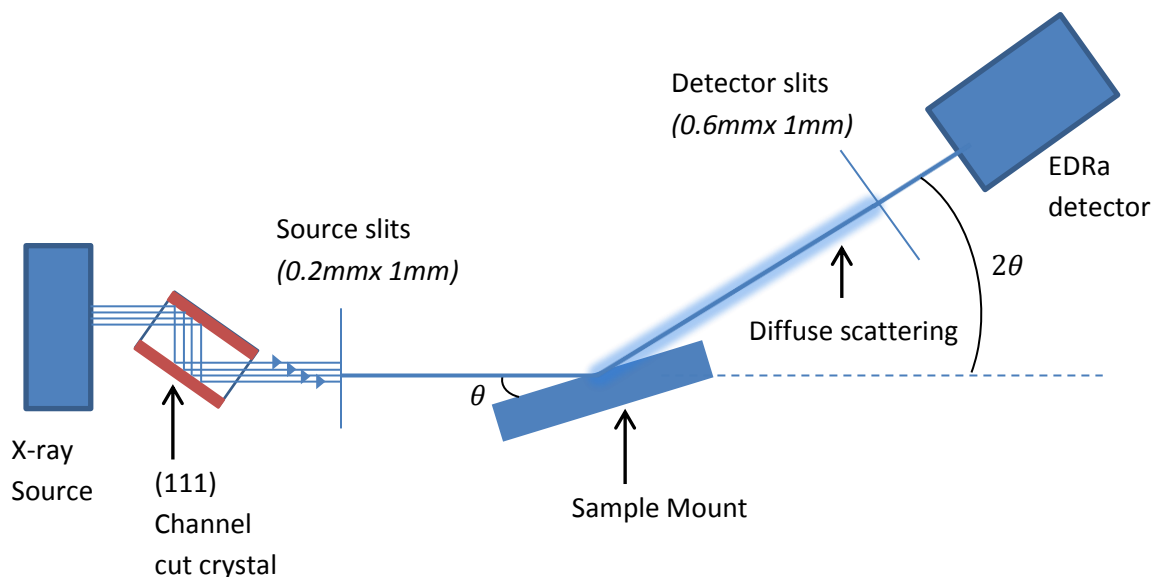

Figure3.7: X-ray geometry plan schematic of the BEDE D1 X-ray diffractometer used for reflectivity measurements.

The sample was secured using double sided tape on a stainless steel backing plate (sample mount) which is mounted on the rotating axis, magnetically. The X-rays produced pass through a Si [220] channel cut crystal and a set of slits to produce a narrow monochromatic beam of Cu-K$_\alpha$1 radiation [19-20]. A metal slit placed in front of the source provides an X-ray spot size of 0.2 mm x 1 mm with a divergence of 0.01°. This large footprint on the sample allows for a larger area averaged and sampled during a particular scan. A slit is inserted after the sample to collimate the reflected beam. The detector used is of scintillation type. The sample was mounted such that the X-rays were incident at an angle θ with respect to the sample surface, and the EDRa detector used to measure the intensity was placed at 2θ.

The generator current and voltage was set to 40 mA and 40 kV respectively and the power was allowed to stabilize for 30 minutes before the measurement. Prior to performing reflectivity measurements, two alignment processes were done to establish strong intensity at the detector and to check for specular conditions for reflection. The source and the detector were aligned in the absence of the sample and with only the slits in the path of the X-ray beam. This was done by recording a 2θ scan for given θ=0°. The 2θ angle corresponding to the peak of the intensity of the resulting scan was selected and was recalibrated to 0°. This was done for each sample to ensure that the optics of the X-ray diffractometer were aligned without the sample in the beam path for maximum intensity. The sample was then inserted in the beam path by moving the sample holder. The sample was moved along this direction until it half cuts the beam i.e. when the intensity count rate approaches half its maximum value. This was done to ensure the entire beam either is blocked by the substrate or reaches the detector after reflecting from the sample surface. The second stage of alignment aimed at establishing the sample surface to be placed completely flat and parallel to the beam. This was done to obtain an accurate value for the critical angle as this is crucial in determining the electron density of the material under investigation. The detector was placed at a small 2θ= 2° and the sample tilted to half that value i.e. θ=1°. This condition is the Bragg condition

for specular reflection and if the sample is perfectly aligned, a peak in intensity is expected for a θ scan at $\theta = {}^1\!/_2 \cdot (2\theta)$. If the sample is slightly misaligned this would accordingly result in a shift of the peak by a certain value of θ and this is recalibrated to be half the angle of the detector with respect to the sample. Following the θ alignment, another half cut scan was performed and the sample is placed at half the maximum beam intensity. A θ scan was done for larger 2θ values (e.g. 2.2 degrees) as well. In order to ensure that the sample is placed in the centre of the beam an intensity scan was performed along the vertical x direction. For a perfect alignment this results in a curve with a minimum in intensity at x=0 mm. The entire process as described above is repeated until the sample is aligned with the beam. It is important to ensure that θ and 2θ remain aligned throughout the reflectivity measurement as even a slight misalignment will result in a drastic decrease in intensity. Therefore, θ was calibrated for increasing values of 2θ during the alignment of the detector. Since in a specular scan the forward diffuse scatter of X-rays can contribute to intensities, an off-specular θ-2θ coupled scan was done to measure the background scattering of X-rays [21]. The sample was off-set by 0.5° and the corresponding intensities for the off-specular condition were measured. This was then subtracted from the specular scan in order to obtain the true specular scatter detailing the out of plane structural properties of the films being investigated.

It is important for the reader to understand the limitations of the various experimental methods prior to the discussion of the results obtained in this study. Hence, the results and their discussion of the three experimental methods described in this chapter are outlined in the following chapter.

Chapter 3- References

[1] Parkin, S.S.P., *et al.*, '*Oscillatory Magnetic Exchange Coupling through Thin Copper Layers*', Physical Review Letters, **66**, (1991), 16

[2] Piramanayagam, S.N., and Chong, T.C., '*Developments in Data Storage: Materials Perspective*', Wiley, New Jersey (2012)

[3] Singulus Technologies AG - Press release '*SINGULUS TECHNOLOGIES will deliver a TIMARIS deposition system to Singapore's Data Storage Institute*' 29th September (2010)

[4] Takanashi, K., *et al.*, '*Indirect exchange coupling through nonmagnetic metal spacers in Co/X/Gd multilayers (X = Cu and Y)*' Journal of Magnetism and Magnetic Materials, **126**, (1993), 242-244

[5] Parkin, S.S.P., *et al.*, '*Systematic variation of the strength and oscillation period of indirect magnetic exchange coupling through the 3d, 4d, and 5d transition metals*', Physical Review Letters, **67**, (1991),3598

[6] Parkin, S.S.P., *et al.*, '*Oscillations in exchange coupling and magnetoresistance in metallic superlattice structures: Co/Ru, Co/Cr, and Fe/Cr*', Physical Review Letters, , **64**, (1990), 2304

[7] Beach, R., *et al.*, '*Minimal Thickness Synthetic Antiferromagnetic (SAF) Structure with Perpendicular Magnetic Anisotropy for STT-MRAM*', US 20140070341 A1, (2014)

[8] Jain, S., *et al.*, '*Giant magnetoresistance behavior of pseudo spin valve rings with magnetostatically coupled elements*' Europhysics Letters, 84, (2008), 1

[9] Hirota, E., Sakakima, H., Inomata, K., '*Giant Magneto-Resistance Devices*', Springer, Germany (2002)

[10] Jergel, J., *et al.*, '*Behavior of giant magnetoresistance in Co–Cu–Co pseudo spin-valves after magnetic annealing*', Thin Solid Films, **520**, (2011), 667-673

[11] Bennett, L.H., and Watson, R.E., '*Magnetic Multilayers*' World scientific publishing Co., Singapore (1994)

[12] Pizzini, S., *et al.*, '*Structural and magnetic properties of Cu/Co and Au/Co multilayers*' Journal of Magnetism and Magnetic Materials, **121**, (1993), 208-212

[13] Wuttig, M and Liu, X., '*Ultrathin Metal Films: Magnetic and Structural Properties'* Springer, Germany (2004)

[14]Tokaç, M., *et al.*, '*Interfacial Structure Dependent Spin Mixing Conductance in Cobalt Thin Films*', Physical Review Letters, **115**, (2015), 056601

[15] Fowley, Ciarán, *et al.*, '*Direct measurement of the magnetic anisotropy field in Mn--Ga and Mn--Co--Ga Heusler films*', arXiv: 1501.03973

[16] Mosca, D.H., *et al.*, '*Oscillatory interlayer coupling and giant magnetoresistance in Co/Cu multilayers*', Journal of Magnetism and Magnetic Materials, **94**, (1991), L1-L5

[17] Urban, K.W., '*Is science prepared for atomic-resolution electron microscopy? '*, Nature Materials, **8**, (2009), 260 - 262

[18] http://www.lightsources.org/regions Accessed on 4th February 2016

[19] Kuech, T., '*Handbook of Crystal Growth: Thin Films and Epitaxy*', Elsevier ,U.S.A (2015)

[20] Prince, E., '*International Tables for Crystallography Vol C mathematical, Physical and Chemical Tables'* Kluwer Academic Publishers, London,(2004)

[21] Moore, C.D., *et al., 'Grazing incidence X-ray scattering for the Characterisation of InP Wafers'*, Denver X-ray Conference on Applications of X-ray Analysis, **40**,(1996),113

|Chapter 4

Results and discussion

4.1 Introduction

This chapter outlines experimental results obtained from different methods described in chapter 3. Three categories of complementary techniques were used to obtain information on different properties on the various films studied with the core goal being to use the information to demonstrate the ability to use the GMR and the AMR effects described in chapter 2 as a device to study magnetisation changes. The key operating principle being that the phenomenon of the Giant Magneto-Resistance depends only on the relative orientations of the magnetisation in the two ferromagnetic layers. The Anisotropic Magneto-Resistance however varies as the relative angle of the current and the magnetisation of the material. By tuning the material parameters precisely it is possible to observe both these effects with sufficient magnitude together in order to study the magnetisation changes in the free layer of a pseudo spin-valve structure. To observe both these effects with appreciable amplitude a pseudo spin valve structure was proposed and optimised. The

three categories of investigative techniques used for these PSV's are structural investigations performed using surface scattering of X-rays, magnetisation dynamics under taken by MOKE magnetometry and transport measurements performed using the magneto-resistance techniques. The results and analysis of the samples studied in this work are discussed within this chapter.

4.2 Magneto-Resistance Measurements

In this study both AMR and GMR for the pseudo spin-valve geometrical stack was studied. The functional materials comprising the pseudo spin-valve were Co, Cu and NiFe. Ta was used as a seed and a capping layer. The difference in the coercive fields for Co and NiFe was used to distinguish between the magnetically hard and soft layers. Cu was used as a spacer layer to facilitate the indirect exchange coupling [1] between Co and NiFe because of its high coupling constant and relatively large oscillation period and also because of very similar band structure matching between Co and Cu to facilitate growth [2]. NiFe was used as a free layer due to its very small coercive field and no magneto-crystalline anisotropy [3]. This would allow for magnetic switching to occur at extremely low applied fields. A schematic detailing the material stacks is shown in Fig 4.1 as a reminder.
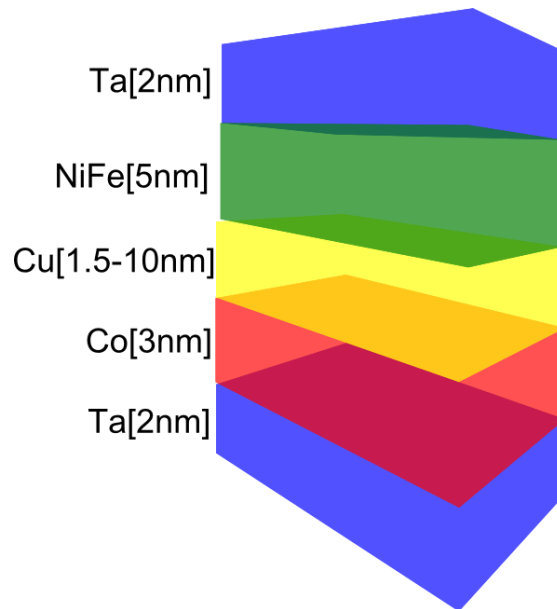

Figure 4.1: A schematic of different material layers comprising the Pseudo Spin-Valve

The Anisotropic Magneto-Resistance of a ferromagnet depends on the relative angle between the direction of current with respect to the magnetisation of the material [4]. When the magnetisation and current are parallel to each other this results in a higher resistance as compared to the orientation when current and magnetisation are perpendicular which results in a lower resistance value. A schematic for the resistance as a function of applied field is shown in the Fig 4.2.
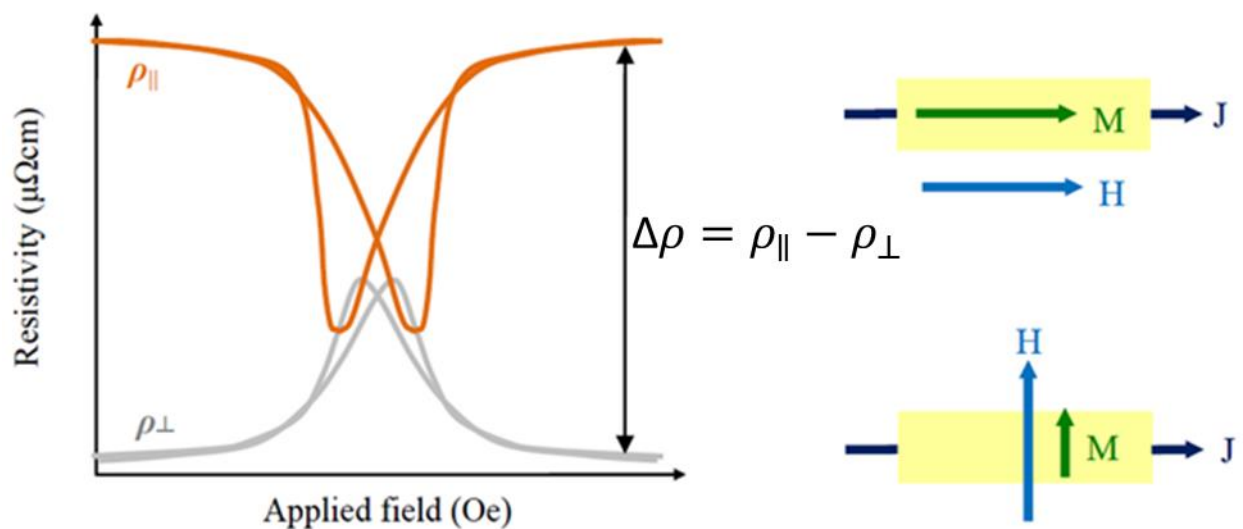

Figure 4.2: Shows a sketch of the anisotropic magneto-resistance signal for an in-plane magnetised Ferromagnet. The current orthogonal to the magnetisation results in a lower resistance value at saturating fields while a higher resistance is obtained when the current and magnetisation are parallel [5].

For a 5 nm Permalloy film the magneto resistance with an underlayer of Cu the Magneto-Resistance curve is shown in Fig 4.3.
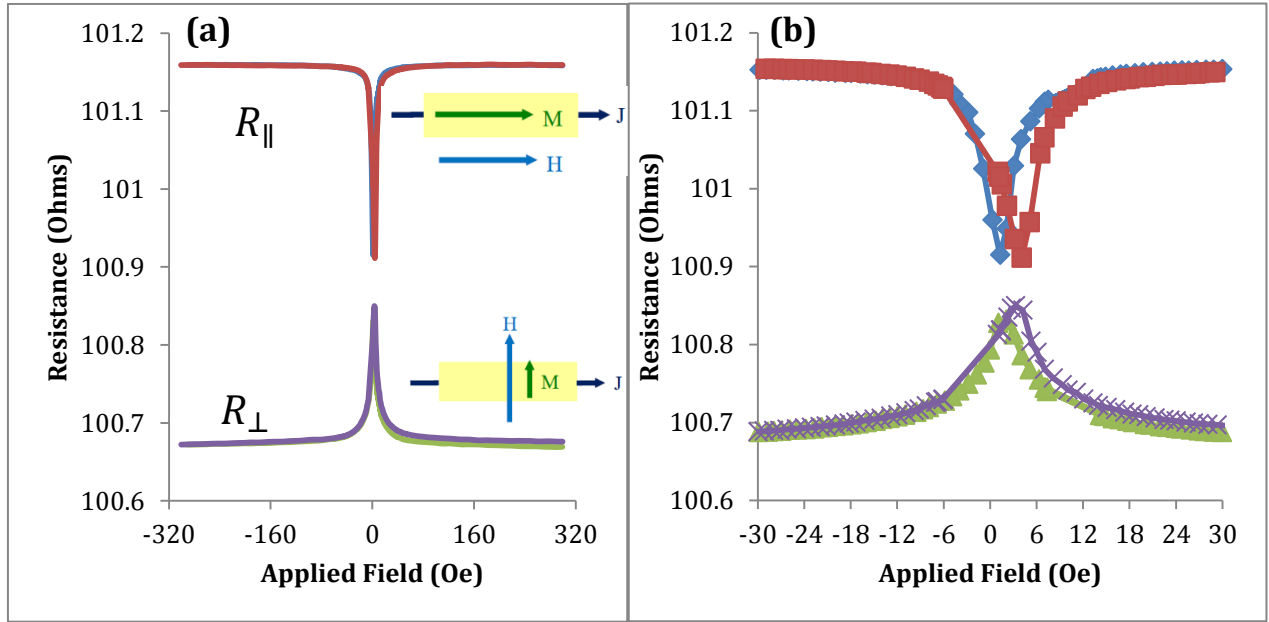
Figure 4.3 : (a) Example of measured Anisotropic Magneto-Resistance response of Sub/Ta(2)/Cu(2)/NiFe(5)/Ta(2) for both increasing and decreasing applied fields with directions in-plane, orthogonal and parallel to the applied current as indicated. (b) An expanded view of (a) with a smaller horizontal scale.

The four point probe method along with the magneto resistance set-up described in chapter 3 was used to obtain the above result. For each in-plane orientation of the magnetisation and the current, $R_{\parallel}$ (resistance obtained when current and magnetisation are parallel to each other) and $R_{\perp}$ (resistance obtained when the current and magnetisation are perpendicular to each other) the sample was initially saturated in fields 800 Oe. The resistance was then measured by changing the external applied fields in large intervals of 10 Oe for higher fields (indicated by the lower density of data points) from 300 Oe to 60 Oe. The field step size was reduced to 1 Oe to avoid under sampling the measurement and the resistance was recorded till zero applied fields, after which the field direction was reversed and the field was changed symmetrically in the negative direction till 300 Oe. For each sample a second measurement was performed in which the sample was saturated initially in high negative fields and the field was reduced to 0 Oe from a high negative value and reversed until resistance saturation in the positive field direction. This constitutes a magneto-

resistance measurement for the perpendicular orientation. The same was repeated with the current direction now parallel to the applied field.

The AMR for a Co film is shown in Fig 4.4. It can be seen that Co too exhibits the typical resistance variation with respect to applied field. The data presented in Fig 4.4 is much noisier due to the compressed resistance scale.
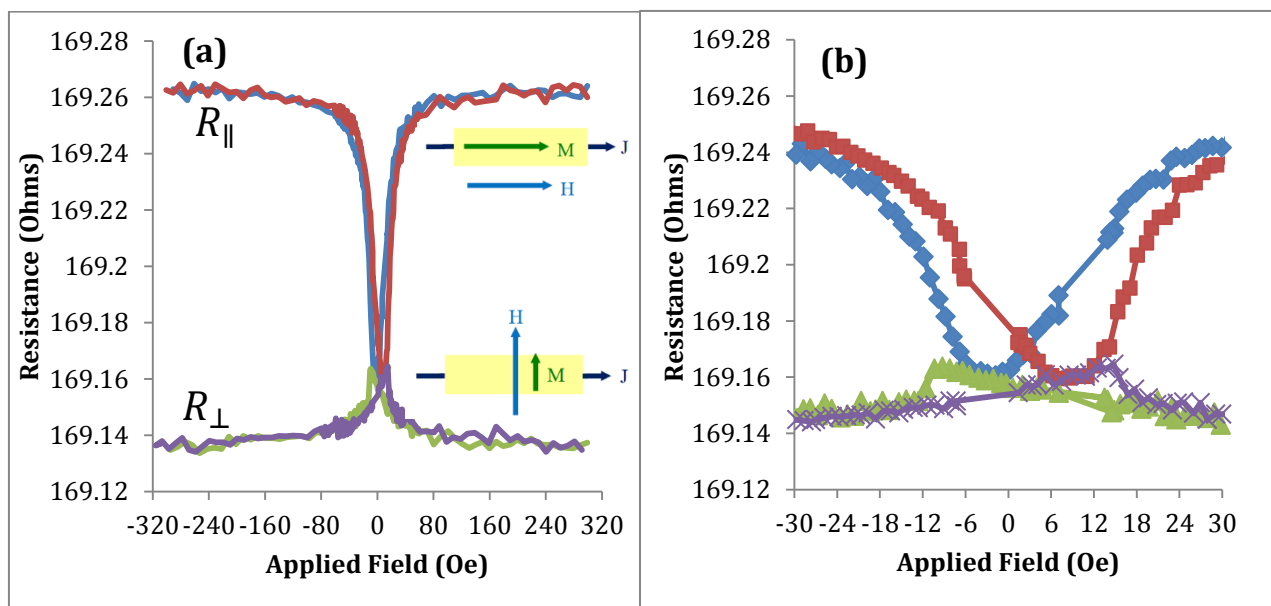

Figure4.4: (a) An example of the Anisotropic Magneto-Resistance response of Sub/Ta(2)/Co(3)/Cu(2)/Ta(2) for both increasing and decreasing applied fields with directions in-plane, orthogonal and parallel to the applied current as indicated. (b) An expanded view of (a) with a smaller horizontal scale.

To confirm the presence of AMR an angular resistance measurement was performed using the rotatable sample stage with respect to a constant applied field. This is shown to be consistent with the eq[2.11] for the angular dependence of AMR modelled in the Fig 4.5 as the dashed curve. The measured angular dependence of the AMR is shown in Fig 4.5.
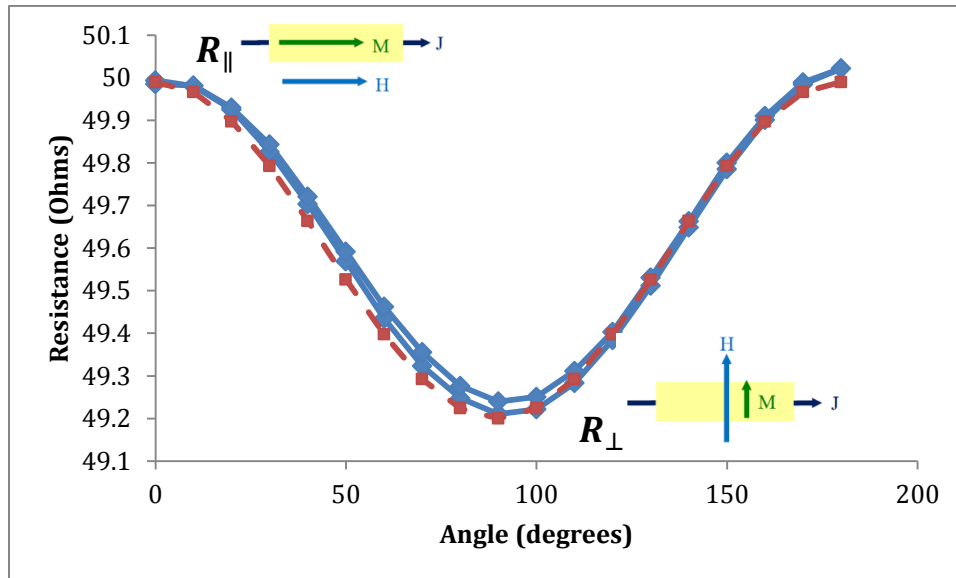
Figure4.5: Angular dependence of the magneto-resistance for a Permalloy film (solid-blue). Indicating a minimum and maximum resistance for 90° and 180°. The horizontal axis indicates the relative angle between the magnetisation and applied current. The angular scan was performed for both increasing (0°-180°) and decreasing (180°-0°). The marginal increase in resistance between the two scan directions is attributed to joule heating due to continuous applied current. A simulation of the expected Magneto-Resistance signal modelled using eq[2.11] (dashed-red).

Both ferromagnetic layers show typical AMR signals independently. However, in order to achieve a strong GMR signal a thin Cu spacer layer was inserted between the cobalt and NiFe layers.

A typical GMR stack with a pinned layer fixed by exchange biasing via an anti-ferromagnet for example IrMn or PtMn show cases a change in magneto-resistance with respect to applied field. A schematic of the typical response curve for a pinned spin-valve device is shown in the Fig 4.6.
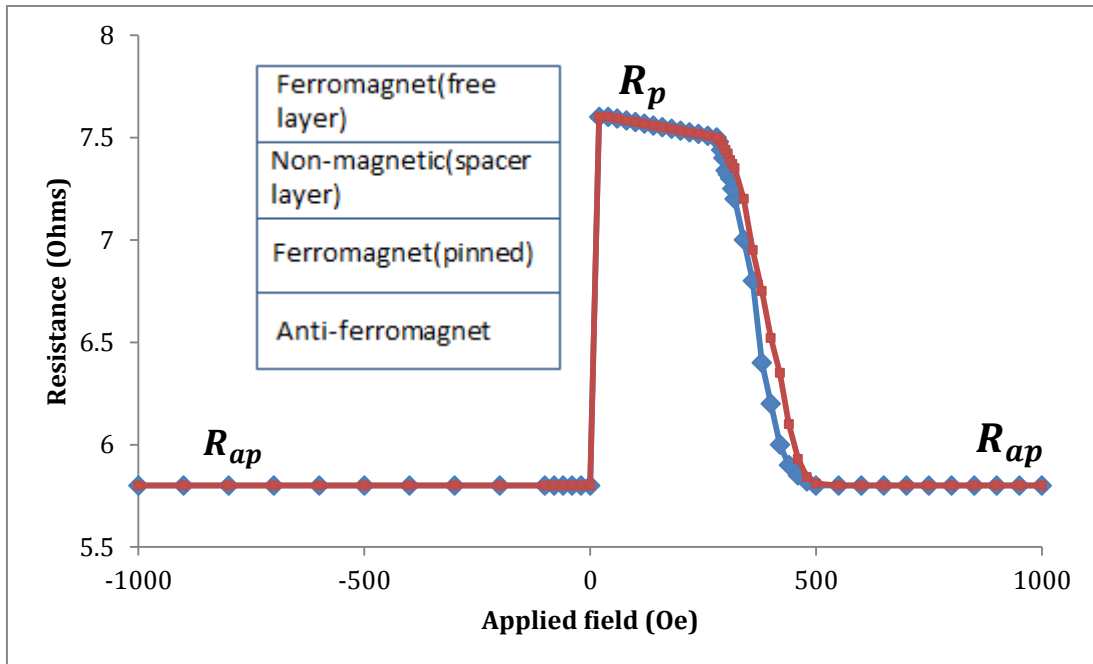
Figure4.6: The typical response curve for a Spin-Valve based on a pinned layer using a SAF or an antiferromagnetic material. A strong antiparallel plateau in the resistance is observed. Increasing the fields leads to a parallel alignment of the moments in each layer and a low resistance value. R_p and R_{ap} denote the parallel and anti-parallel alignment of the individual layers respectively.

A high resistance plateau is observed for both negative and positive field directions, this corresponds to the antiparallel alignment of magnetisation in each FM layer in the material stack. As the field is increased the two layers align in the direction of the field and together contribute to a lower resistance value.

For a Pseudo Spin-Valve, the magnetisation of the pinned layer is not fixed, i.e. there are no antiferromagnets used, this results in a complicated magneto-resistance response. An example for one particular instance is shown in Fig 4.7.
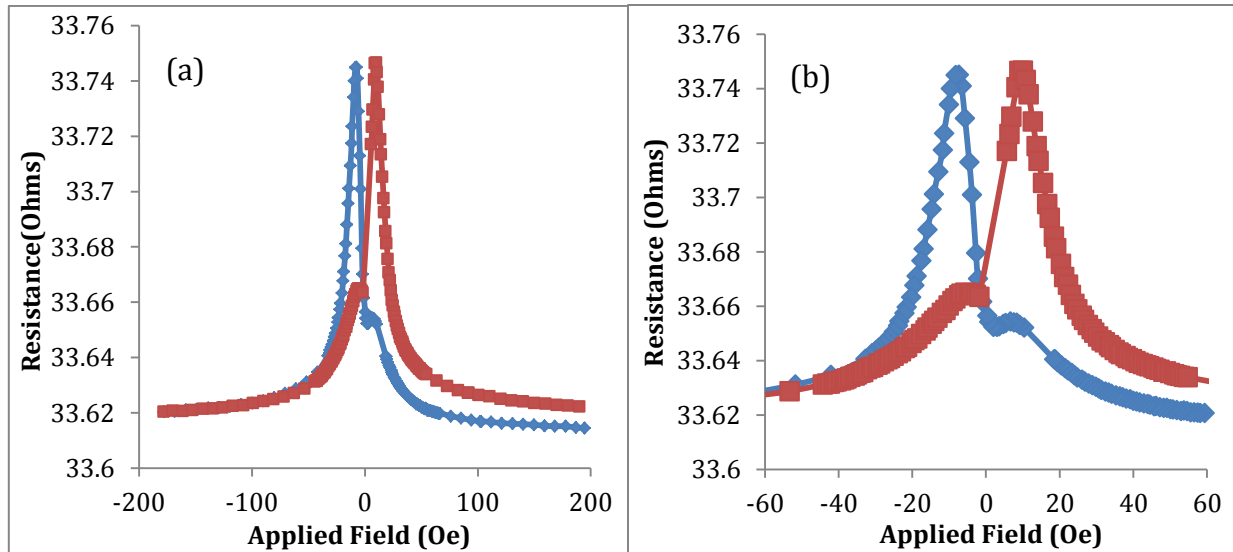
Figure4.7: (a)Magneto-Resistance for magnetic field applied parallel to current in the plane of the sample for Ta(2)/Co(3)/Cu(4)/NiFe(5)/Ta(2) all thicknesses are in nm. Magneto-Resistance field dependent measurement was started at positive saturation fields shown in Blue. The incrementally higher resistance at high positive fields is due to joule heating. (b) An expanded view of (a) with a smaller horizontal scale.

In Fig 4.7 the current was applied parallel to direction of external field. There are two distinguishing features compared to a typical GMR stack consisting of a SAF (shown in Fig 4.6) or an antiferromagnetic material. Firstly there is no antiferromagnetic plateau but a sharp peak, this results due to the weak coupling between the Co and the NiFe layers and because of lack of strong pinning of the fixed layer. The weak coupling does not allow the two layers' magnetisation to attain and hold an anti-parallel geometry which thereby results in a lack of a plateau as observed for the typical GMR case. Secondly one observes a feature close to zero applied field which resembles the AMR for a single FM layer when the direction of applied current and external field are parallel.

This feature strongly depends on the coupling between the two layers as it can be tuned by changing the thickness of the copper layer. It is shown in Fig 4.8 for a copper thickness of 1.5 nm the feature is enhanced.
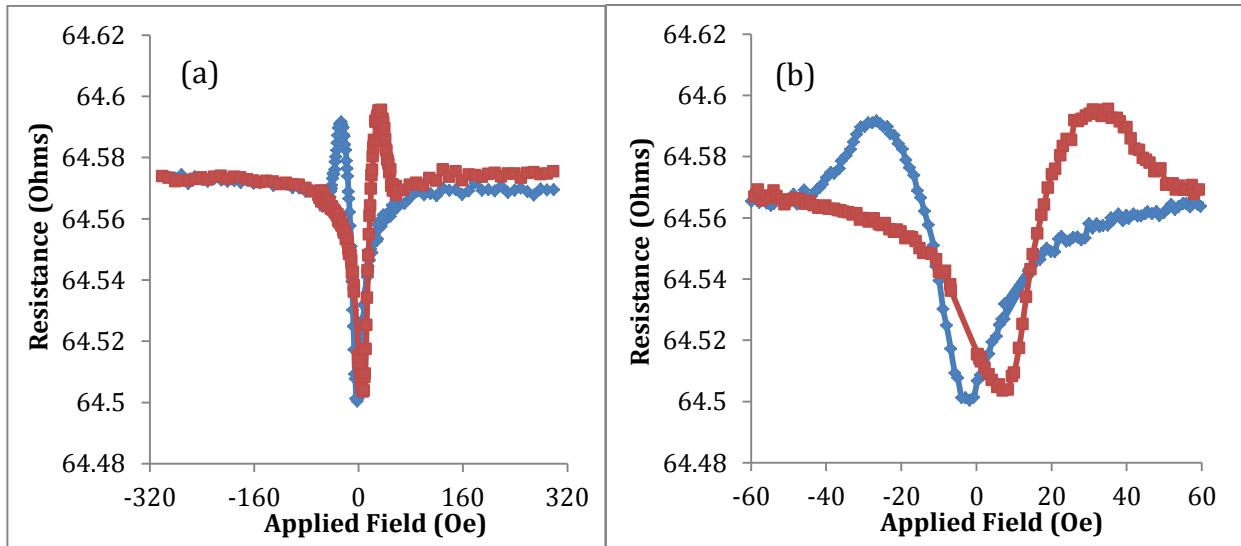
Figure4.8: Magneto-Resistance of Ta(2)/Co(3)/**Cu(1.5)**/NiFe(5)/Ta(2) for applied field parallel to current in the plane of the sample. All thicknesses are in nm. (b) An expanded view of (a) with a smaller horizontal scale.

For the material stack shown in Fig 4.8, both the Anisotropic and the Giant Magneto-Resistances are exhibited. The sharp rise in resistance with decreasing fields is due to the GMR effect and the decrease in resistance symmetrically is attributed to the $R_{\parallel}$ configuration of the AMR. The measurements to study GMR were performed with the current and field parallel as the sign of GMR and AMR are opposite for this geometry. When the MR is measured with the field and current perpendicular it results in an addition of the GMR and AMR contributions and becomes difficult to distinguish one from the other. This is shown in the example (Fig 4.9), for the same material system shown in Fig 4.8 the measurement was performed with current and field perpendicular and in the plane of the film.
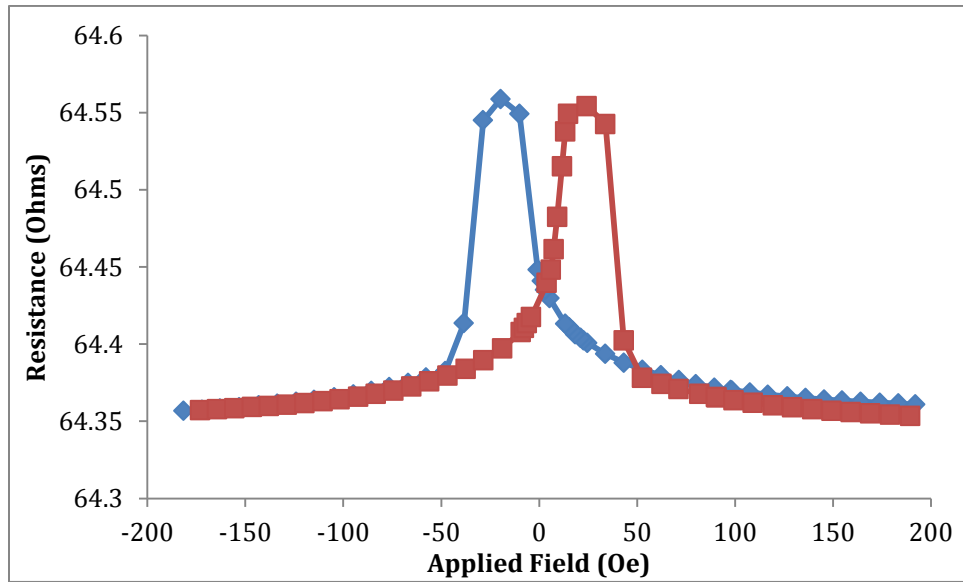
Figure4.9: Magneto-Resistance of Ta(2)/Co(3)/**Cu(1.5)**/NiFe(5)/Ta(2) for applied field orthogonal to current in the plane of the sample. All thicknesses are in nm.

Both signals from the transversal orientation of AMR as shown in Fig 4.4 as well as the GMR signal are combined in the Fig 4.9, and it is difficult to de-convolute them.

Due to the complexity of the magneto-resistances observed it is important to be able to attribute which phenomenon (AMR or GMR) the change in resistance originates from. In order to do this let us consider the magneto-resistance shown in Fig 4.10 for a 2 nm Cu spacer with 3 nm and 5 nm of nominal Co and NiFe as the pseudo pinned and free layer respectively. The film is grown on a seed of 2 nm of Ta and a 2 nm Ta capping layer is used for oxidation protection. The seed and the capping layers are identical for every stack investigated in this study to ensure that there is no change in the microstructure of the three functional layers due to different seed or capping layers.
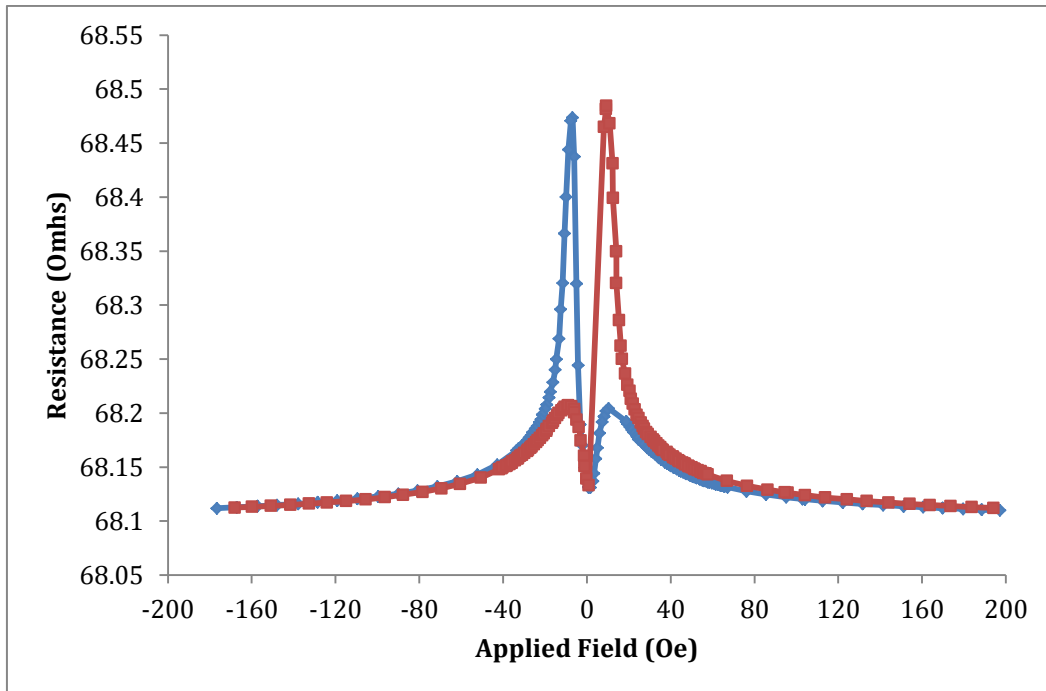
Figure4.10: Magneto-Resistance of Ta(2)/Co(3)/**Cu(2)**/NiFe(5)/Ta(2) for applied field parallel to current in the plane of the sample. All thicknesses are in nm.

A range of Cu thicknesses were investigated and most, exhibited the feature i.e. a sudden decrease in resistance near zero applied field. This feature is exhibited by most films with changing degree of intensity. This film of which the magneto-resistance is shown in Fig 4.10 exhibits a typical convoluted signal which is atypical for a GMR stack. In order to understand the magneto-resistance contributions from all functional ferromagnetic layers, the film can be considered to be composed of two halves which together contribute to the displayed magneto-resistance.

A Co(3)/Cu(2) film and a Cu(2)/PY(5) film were grown (numbers in brackets represent thicknesses in nanometers) with nominal capping layers and seed layers. Their magneto-resistances were studied. The AMR for each of these films is shown in Fig 4.11. As each of these films consist of single ferromagnetic layers, it is possible to use a parallel resistor model to understand how much each of the layers contributes individually to the resistance. To visualise the magnetisation reversal as a function of applied field the resistance change for the longitudinal geometry (current parallel to

applied field) of each individual film consisting of either Co or NiFe as a single ferromagnetic layer is

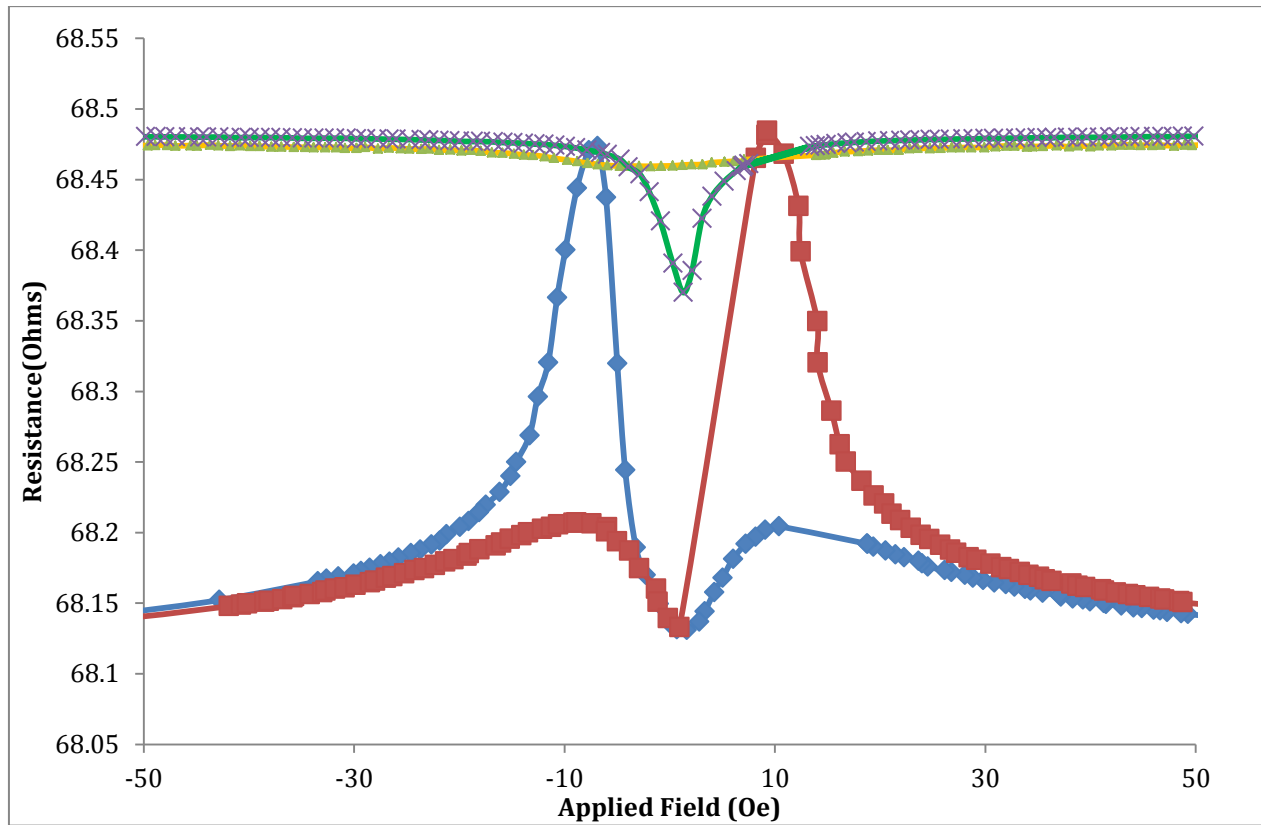plotted along with the magneto-resistance of entire GMR stacked film shown in Fig 4.11.

Figure4.11: The Magneto-Resistance for Ta(2)/Co(3)/Cu(2)/NiFe(5)/Ta(2) for field parallel to current in the plane of the sample. Curve shown (Red) represents the change in resistance with increasing fields from negative to positive saturation. Curve shown (blue) represents the change in resistance with decreasing fields from positive to negative saturation. Variation shown (Green) represents the change in resistance with decreasing fields from positive to negative saturation for NiFe(scaled) and (yellow) for Co(scaled).

There are several features which must be highlighted. For simplicity only the resistance change as a

function of decreasing field amplitude is shown for Permalloy and cobalt in Fig 4.11. It can be seen

that for the NiFe film there is a decrease in resistance at near-zero fields which is consistent with

the decrease in resistance for the entire GMR stack. However on inspecting the magneto-resistance

of the single Co film there is only a slight decrease in resistance compared to the resistance change

for a single NiFe film. Therefore, the feature observed near zero fields in the GMR stack corresponds

to a longitudinal geometry Magneto-Resistance which predominantly emerges from the NiFe free layer.

The Giant Magneto-resistance as described earlier is dependent crucially on the coupling between the two ferromagnetic layers, and this oscillatory coupling is proportional to $1/d^2$ at room temperature [1] where d is the thickness of the spacer layer. There is a gradual decay of the oscillations and the envelop function decays as $1/d^2$ [7]. 6 different samples with increasing nominal Cu thicknesses were grown and their Magneto-Resistance measured as shown in Fig 4.12.
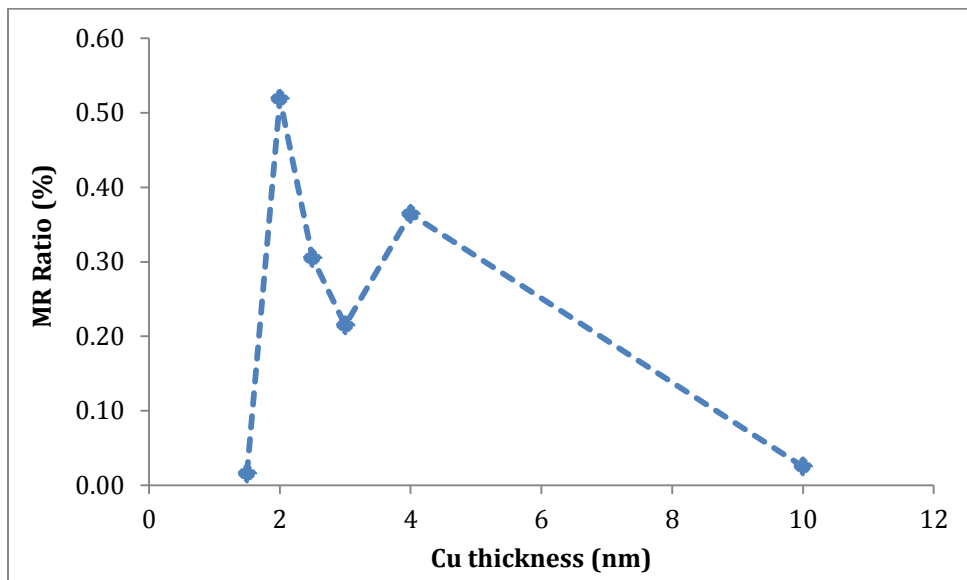

Figure4.12: The change in the measured magneto-resistance as a function of Cu thickness for nominal stack Ta(2)/Co(3)/Cu/NiFe(5)/Ta(2). All thicknesses are in nm. Note the magneto-resistance measured here is for films with **no** cobalt insertion between the spacer and free layer. Error bars are not visible since they are smaller than the data points.

It can be seen from Fig 4.12 that for the 1.5 nm and the 10 nm of Cu thickness the GMR is very low. It is possible that for the 1.5 nm the thickness of the spacer layer is very low which allows both the ferromagnetic layers to couple strongly and essentially the spin reversal for each layer is coherent. However for the 10 nm copper spacer the coupling is extremely weak which gives rise to the lower GMR value. It is also suggested that the magneto-resistance as predicted is oscillatory in nature with a period of approximately 1 nm. This is consistent with the periodicity of the coupling of Cu as

shown by S.S.P Parkin *et al* [1]. The highest GMR percentage obtained using the pseudo spin valve construction is 0.5% as shown for the 2 nm nominal Cu spacer in the Fig 4.12.

Since it is the spin-dependent scattering of the electrons which governs the giant magneto-resistance, it is crucial that there is little interface mismatch i.e. lower band structure mis-match. With regard to the same and to achieve a higher GMR ratio without compromising the anisotropic contribution of the Magneto-Resistance, a 1 nm Co layer was inserted at the interface between the spacer and the Permalloy layers. It was shown by S.S.P Parkin *et al* that interface states which contribute to the enhancement of the GMR for a characteristic length which is extremely small and ranges from 1.5 Å to 3 Å [6]. Cu and Co have very similar band matching and it was postulated that this would assist in the electron transport through to the free layer [6].
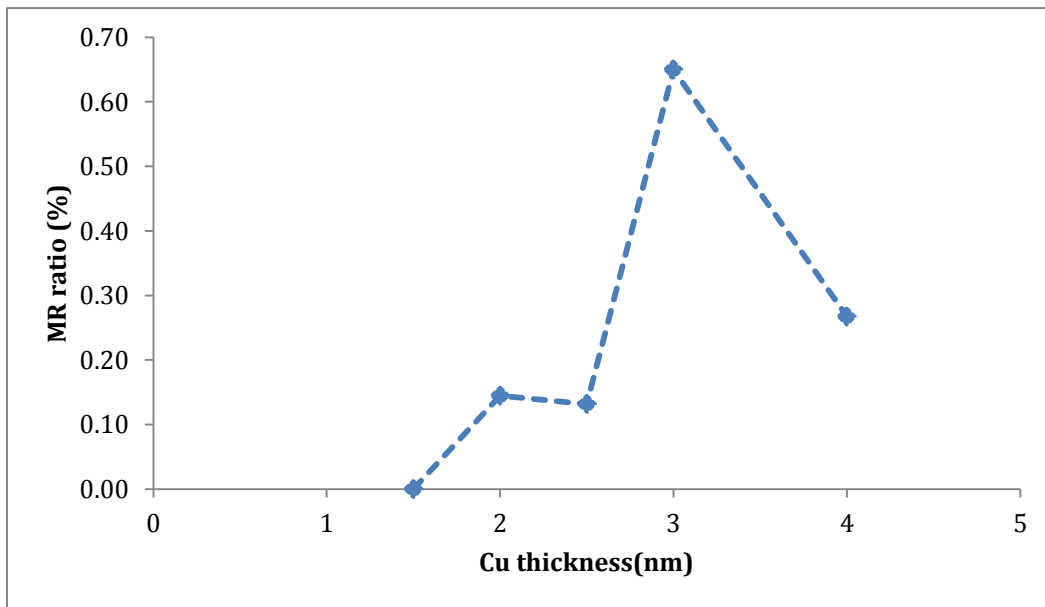

Figure4.13: The change in the measured magneto-resistance as a function of Cu thickness for a nominal 1 nm Co used as an insertion layer at the top interface of Cu i.e between the Cu and the NiFe free layer of the PSV Ta(2)/Co(3)/Cu/NiFe(5)/Ta(2). Error bars are not visible since they are smaller than the data points.

However it can be seen that there is no large increase in the absolute magneto-resistance with the insertion of the cobalt insertion layer. In fact for the nominal 2 nm Cu spacing which showed a large magneto-resistance (see Fig 4.12) after insertion of the Co at the top interface between the spacer

and free layer shows a 50% reduction in the magneto-resistance(see Fig 4.13). However, there may still be an oscillation in the Magneto-Resistance.

Another method to attain a relatively higher GMR without the use of a pinning layer was to apply a magnetic field during deposition. The results and discussion related to measurements done with regard to the same are outlined in section 4.2.1 below.

4.2.1 Magneto-resistance with field induced anisotropy

The magneto-resistance data shown in this section is obtained from material stacks which were deposited in the presence of a uniform directional magnetic field so as the magnetic layers develop field induced anisotropy. 10 samples with the nominal stack consisting of Ta(2)/Co(3)/Cu(t)/NiFe(5)/Ta(2) with t=1.6, 1.8, 2, 2.4, 2.6, 2.8, 3, 3.2, 3.4 and 3.6 nm were grown using the sample holder with permanent magnets as described in section 3.2.3. A 100 Oe magnetic field was applied using the permanent magnets during deposition. The Magneto-Resistance of a subset of samples is shown in Fig 4.14.

The Fig 4.14 shows the magneto-resistance with the field applied parallel to the current direction in the plane of the film for copper thicknesses between (4 nm and 1.6 nm). For the 4 nm Cu thickness film it can be seen that there is a strong anti-parallel coupling.
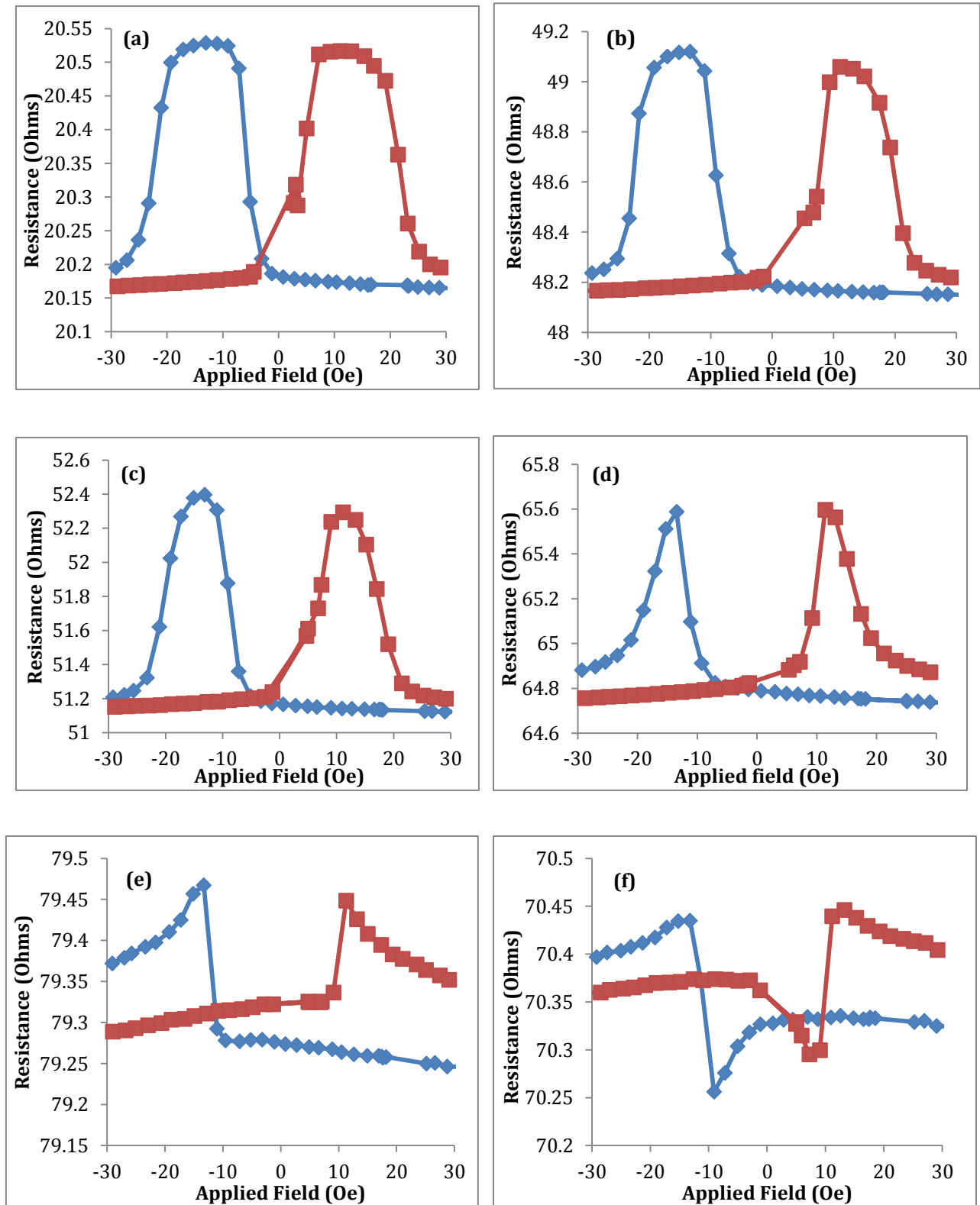
Figure4.14: The Magneto-Resistance of thin films deposited in the presence of a field through a shadow mask of a stripe for the PSV stack comprising of Ta(2)/Co(3)/Cu(t)/NiFe(5)/Ta(2) (a)t=4 nm (b) t=3.6 nm (c)t=3.2 nm (d)t=2.4 nm (e)t=1.8 nm (f)t=1.6 nm.

As the film thickness is varied from 4 nm to 1.6 nm the magneto-resistive response for each film changes. This is especially evident when magneto-resistance of Fig 4.14(a) is compared with Fig 4.14(f), i.e. the thickest and thinnest films. For thicker spacer layers it is observed that there is a broad region in field approximately 20 Oe during which anti-parallel alignment of the magnetisation between the Co and NiFe layers is maintained. As the thickness of the spacer layer decreases the coupling between the two layers changes and this is observed in the change in magneto-resistance shown in Fig 4.15 for different spacer thickness. For thinner spacer layer the high resistance plateau begins to decrease in field size gradually changing from a system in which the magneto-resistance is dominated by the Giant Magneto-Resistance towards a state which exhibits Anisotropic Magneto-Resistance as can be seen for the thinnest copper spacer. For small spacer layer thickness the GMR is greatly reduced. Two possible explanations for this observation exist, firstly that as the spacer layer reduces in thickness there are pin holes which are generated that couple the two ferromagnetic layers through direct exchange, Secondly, as the thickness of the copper was decreased, the effective dipolar coupling between the two ferromagnets would allow the ferromagnets to couple and act effectively as a single entity. This dipolar coupling would increase with decreasing thickness of the spacer layer for fixed thicknesses of the ferromagnets. This is shown as the reduced GMR effect and the presence of the signature longitudinal anisotropic magneto-resistance behaviour for the thinnest spacer layer.

In order to understand if there is indeed RKKY coupling via the spacer layer, the Magneto-Resistance as a function of the copper spacer layer is shown in Fig 4.15.
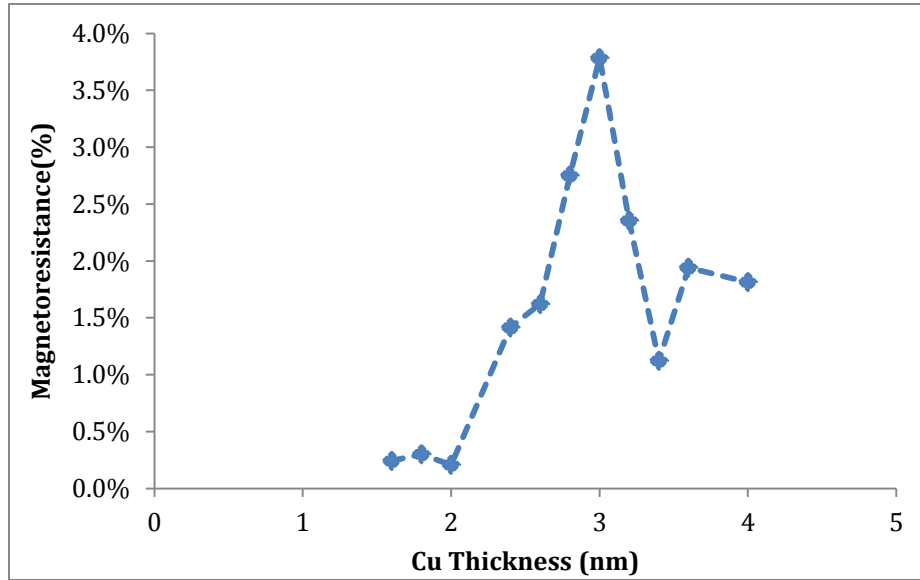
Figure4.15: The Magneto-Resistance as a function of the Cu spacer layer thickness in nanometers for full films of the form Ta(2)/Co(3)/Cu(t)/NiFe(5)/Ta(2) measured with the Current and applied field parallel and in the plane of the sample. Error bars are not visible since they are smaller than the data points.

It can be seen that the magneto-resistance ratio peaks and falls in magnitude as a function of the spacer layer thickness. In order to ensure that there was no aliasing the Magneto-Resistance was measured in intervals of 2 angstroms of the copper thickness. All the films had Co and NiFe with nominal thicknesses of 3 nm and 5 nm. The magneto-resistance is maximum for 3 nm of Cu spacer layer. Assuming an oscillatory behaviour, its period as deduced from Fig 4.15 is approximately 1 nm which is in agreement with [1], [6] and [7].
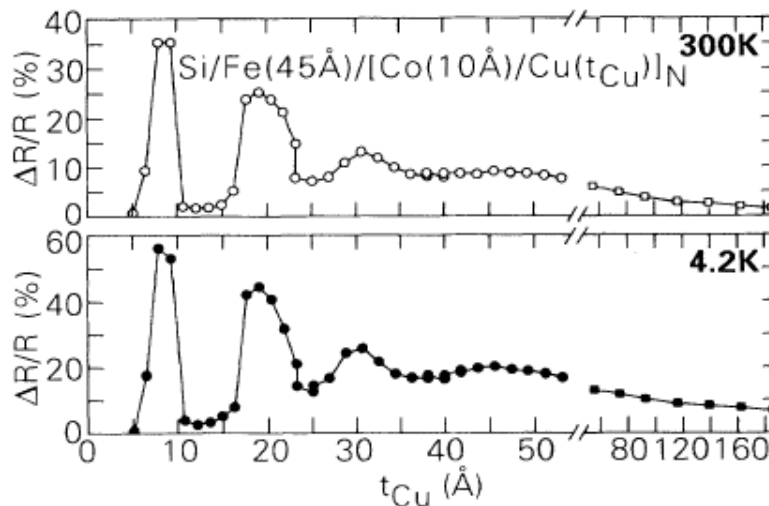

Figure4.16[1]:Oscillatory coupling shown for Co/Cu multilayers at room temperature and 4.2K .

The absolute magnitude of the total magneto-resistance for Fig 4.16 [1] and from Fig 4.15 is different primarily because the author from [1] used a multilayer thin film with repetitions of the layers. This results in higher scattering of the *s* electrons and contributes to a larger resistance. The larger number of repeats leads to an additive effect of the antiparallel coupling which raises the total magneto-resistance. Also, as compared to having a NiFe layer the free layer for [1] consists of Co. Co/Cu and the Cu/Co interface both are transparent to the electrons and do facilitate any spin-flip scattering from occurring which may reduce the GMR.

4.3 MOKE magnetometry and structural properties

In developing a material system to study magnetisation dynamics it is crucial to understand the spin reversal mechanism which govern ultimately not just the magnetisation but also the transport properties of the entire stack. Magnetisation reversal and switching for pseudo-spin-valves was studied using the magneto-optical Kerr effect. The reversal mechanism is used to provide insights into the transport properties described earlier and can be used as a complementary technique along with magneto-resistance measurements. Magneto-optical Kerr effect magnetometry was performed on three categories of samples. (1) As grown full thin films with the nominal pseudo-spin-valve material stack, (2) thin films grown in the presence of *in-situ* applied magnetic fields, (3) Patterned microstructures of the full film grown with *in-situ* magnetic fields. Details with regard to each category of samples are discussed below.

4.3.1 As-deposited thin films

The Kerr signal as a function of external applied field for a pseudo spin-valve thin film is shown in the Fig 4.17. The ferromagnetic layer thicknesses are kept nominally the same but the copper spacer layer thickness was changed from 1.5 nm to 10 nm. The film structure for the hysteresis curve shown in Fig 4.17 is substrate/Ta(2)/Co(3)/Cu(4)/PY(5)/Ta(2) with thicknesses within parenthesis in nanometers.

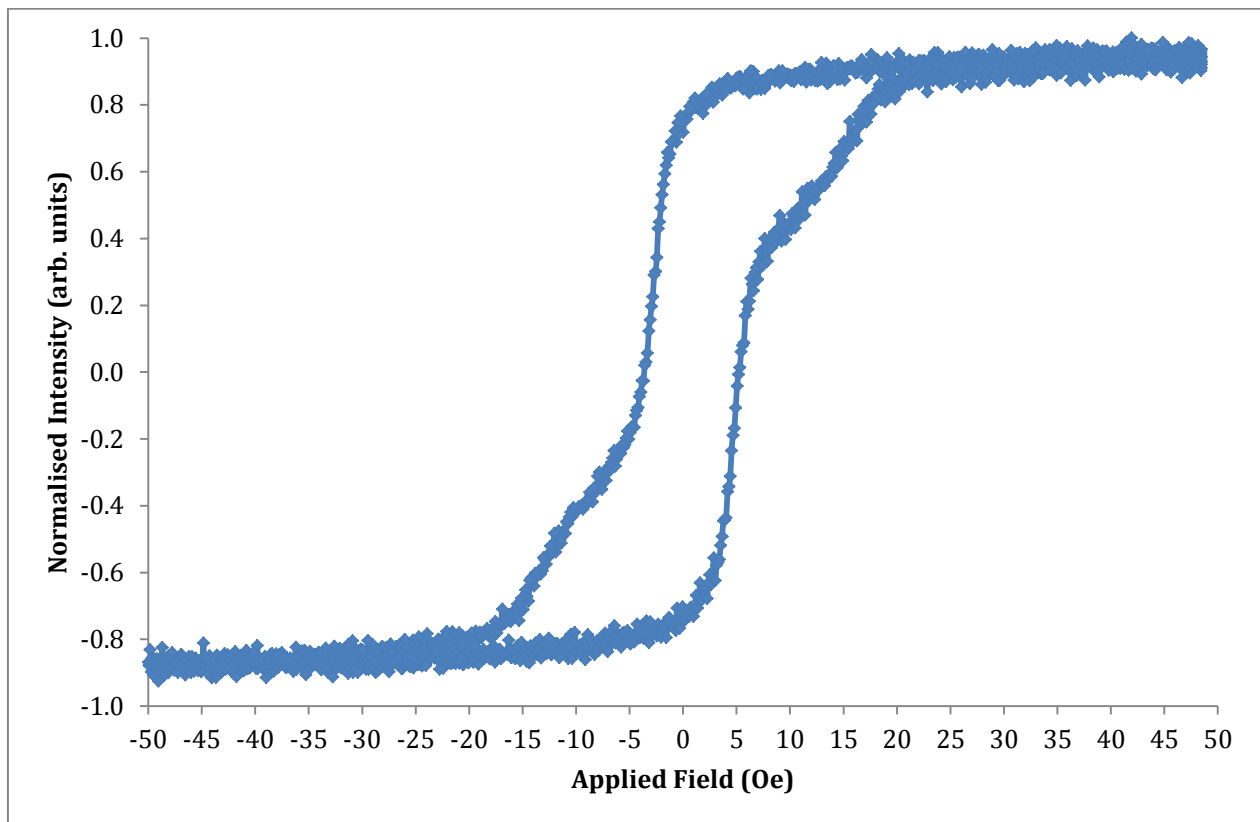Figure4.17: Hysteresis curve obtained using MOKE magnetometry for Ta(2)/Co(3)/Cu(4)/NiFe(5)/Ta(2). Two distinctive regimes are observable which are attributed to the switching of the two ferromagnetic materials comprising the mentioned stack.

The hysteresis curve shown in Fig 4.17 was measured using a longitudinal geometry in-plane MOKE. One can observe two distinct switching behaviours for the magnetization. The two reversal events

occur at different applied fields as well as the field coverage during each reversal is different. Owing to the lower coercive field of Permalloy and the near zero magneto crystalline anisotropy [8], the sharper switching observed is attributed to NiFe and the slower switching observed over a larger field duration is attributed to the pseudo-pinned Co layer. For a pinned layer system in a Magnetic Tunnel Junction (MTJ) or a GMR device using synthetic anti-ferromagnets, the hysteresis curves typically are entirely separated for both free and pinned layer. There are efforts amongst the storage industry sector to create material geometries in which this field gap between two switching events is as large as possible. For a pinned GMR device used in the data storage industry it is called the operating window. However, as mentioned earlier the purpose of this study is to use GMR as a tool to study magnetization dynamics and employ both AMR and GMR effects to understand how the magnetization changes. It is important to find the optimum thickness at which there is significant separation in switching events. For thinner copper spacer layer thickness of 3 nm the magnetization as a function of field for the in-plane longitudinal and transversal MOKE is shown in Fig 4.18.
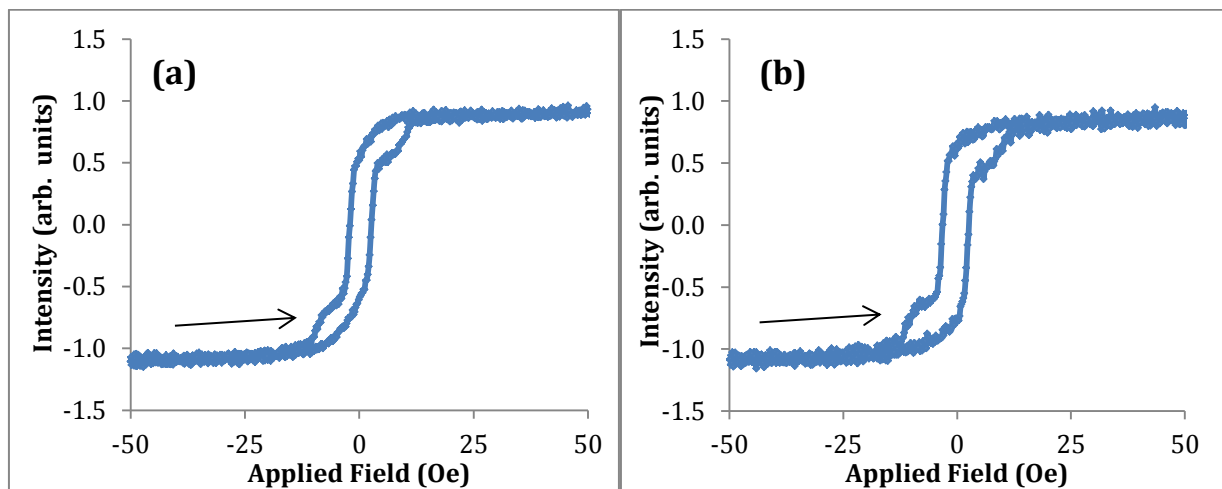
Figure4.18: Hysteretic response to field for Ta(2)/Co(3)/Cu(3)/NiFe(5)/Ta(2) full film sample grown on a 10x10mm scribed Si/SiO$_2$ substrate for two different orientations (a)0° and (b) sample rotated by 90° in the plane of the applied field.

It can be seen from the two hysteresis curves shown in Fig 4.18(a)(b), that the coupling between the two ferromagnetic layers has changed as the copper thickness is decreased from 4 nm to 3 nm as

highlighted in Fig 4.18 and Fig 4.17. There is also a slightly different reversal mechanism when the sample is rotated in the plane of the field. There could be two possibilities for the source of this anisotropy, 1) an intrinsic magnetocrystalline anisotropy arising from the Co layer (textured growth along a particular direction) 2) a stray magnetic field being produced by the different magnetron sources inside the main chamber during the film growth. The anisotropy is enhanced when 1 nm cobalt is inserted at the interface between Cu and NiFe. This was done as it has been shown by other groups that the operating window is enhanced due to a smoother interface between the spacer and the free layer. The magnetization as a function of field for a sample with nominal thickness as Ta(2)/Co(3)/Cu(3)/Co(1)/NiFe(5)/Ta(2) is shown in Fig 4.19.
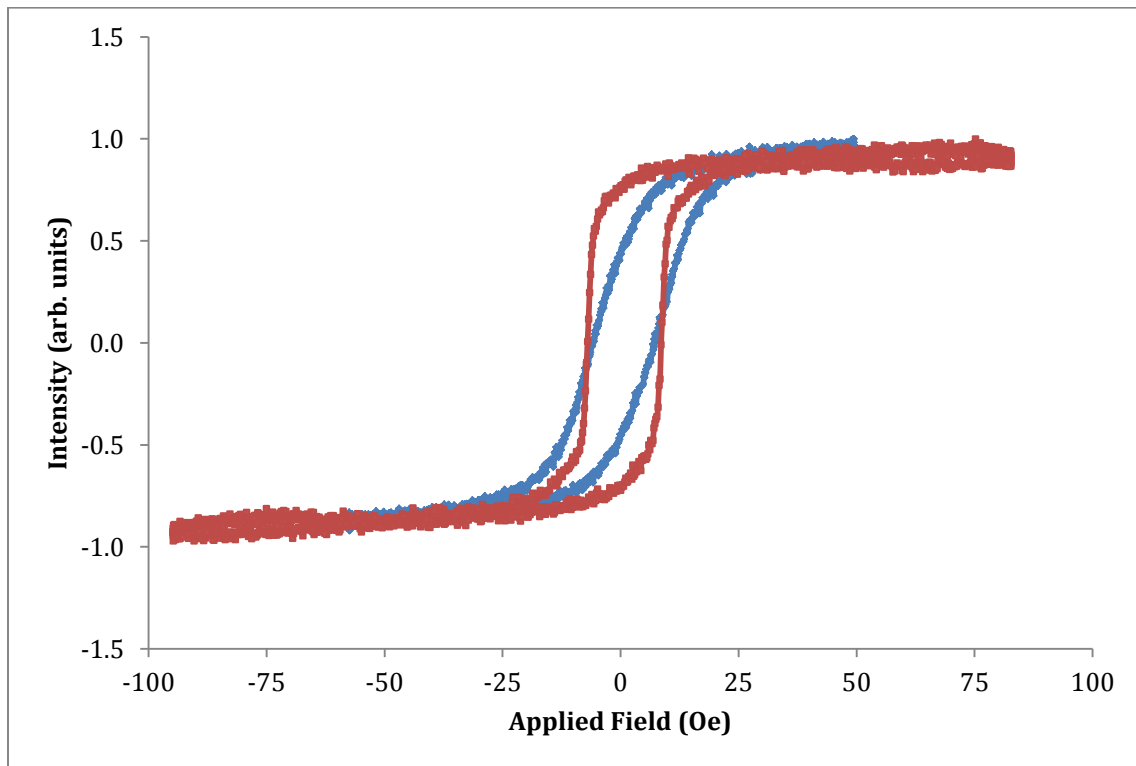

Figure4.19: Hysteresis for Ta(2)/Co(3)/Cu(3)/Co(1)/NiFe(5)/Ta(2) for longitudinal in plane MOKE. Hard axis behavior was observed when the sample was rotated in the plane of the applied field by 90°.

A hysteresis loop with some characteristics of a hard axis is obtained when the sample is rotated by 90 degrees in the film plane. In both the geometries the coercive field is ~7 Oe. No distinguishable switching is observed from the free and pinned layers. A possible reason for this could be due to the skin depth effect of the MOKE described in section 2.7.3. However, the skin depth for Permalloy is ~11 nm, which implies the lack of observable independent switching may be due to small coupling for this spacer thickness. When the copper thickness is reduced to a much thinner nominal 1.5 nm thickness there is distinct switching which is observed as shown in Fig 4.20.
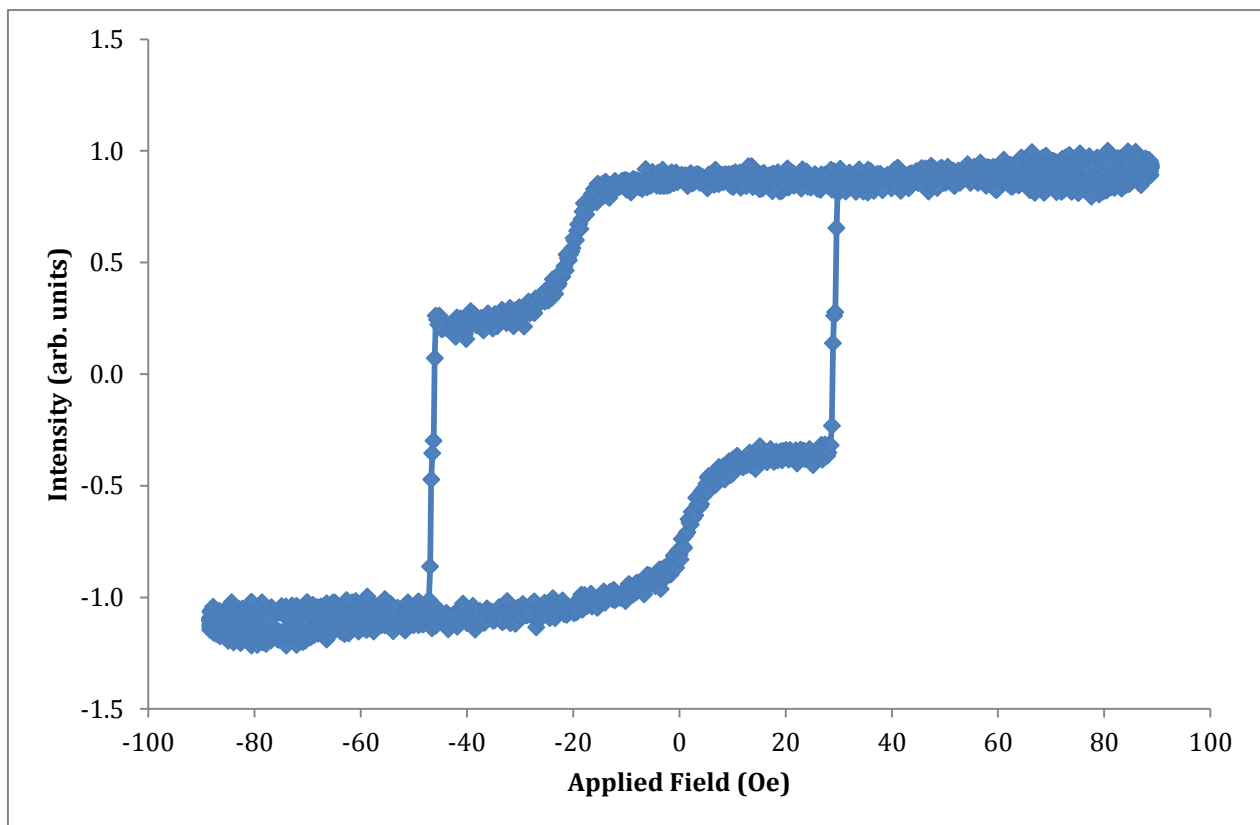
Figure4.20: Shows the hysteresis curve obtained for a 1.5 nm Cu spacer pseudo spin valve full film grown of the structure Ta(2)/Co(3)/Cu(1.5)/NiFe(5)/Ta(2). The sample was grown on a 10x10 mm scribed Si/SiO$_2$ substrate.

When comparing the hysteresis shown in Fig 4.20 with the transport measurements in Fig 4.8, it can be seen that for the 1.5 nm Cu spacer layer film stack displays a distinct GMR effect. The in-plane anisotropy which is observed for the as-deposited thin films is removed when the entire stack is

deposited in the presence of an external applied field during deposition. This is explained in the following section.

4.3.2 *In-situ* field deposited thin films

Magnetic hysteresis loops were measured for thin films with nominal pseudo spin-valve stacks of Ta(2)/Co(3)/Cu(t)/NiFe(5)/Ta(2) where the Cu spacer layer was changed from 1.6 nm to 4 nm. All magnetic films discussed within this section are deposited in the presence of an *in-situ* external in-plane magnetic field. The MOKE as stated earlier in section 4.3 provides a complementary method to understanding magnetization dynamics occurring in the PSV's described in this work. Magnetization reversal occurring as a function of applied magnetic field for certain Cu spacer layer in PSV's are shown in Fig 4.21.
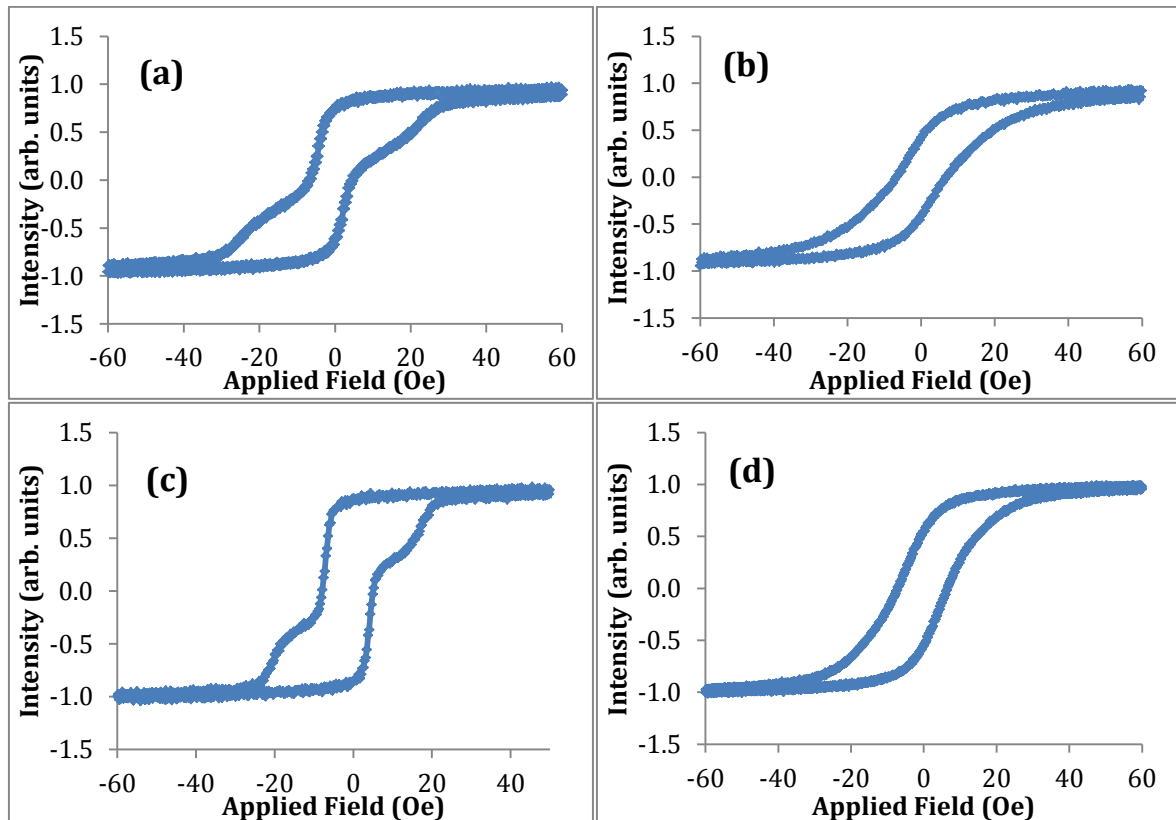

Figure4.21: Examples of hysteresis curves for two orientations of the films (a-b) Ta(2)/Co(3)/Cu(**4**)/NiFe(5)/Ta(2) and for (c-d) Ta(2)/Co(3)/Cu(**3.6**)/NiFe(5)/Ta(2). (a)(c) The field was applied in the plane of the sample; (b)(d)the sample was rotated by 90 degrees in the plane of the applied field.

The films as shown in Fig 4.21 exhibit a two-fold anisotropy in the plane of the film this can be seen from the hard axis loops shown in Fig 4.21(b) and Fig 4.21(d). Distinctive switching can be seen for the easy axis. However, when the sample was rotated by 90° and the field was applied along the hard axis direction the hysteresis curves for both the 3.6 nm and the 4 nm film do not show separate switching. Here the data is only shown up to 50 Oe to highlight the switching events occurring at low fields. However, for each measurement the hysteresis curve was obtained for saturating fields up to 300 Oe. No switching event was recorded for the hard axis orientations for any *in-situ* field deposited sample.

It can be seen from Fig 4.22 that for the 3.2 nm Cu spacer layer full film both the free layer and the pseudo pinned layer switch separately.
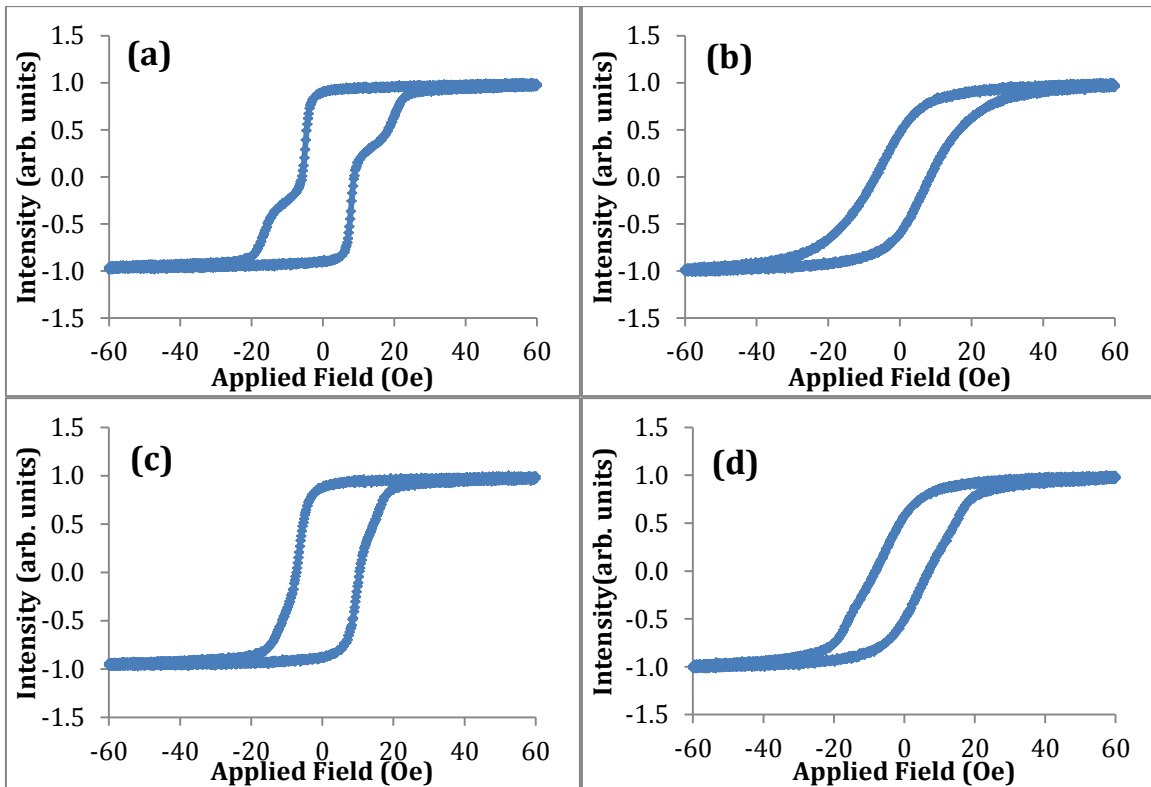

Figure4.22: Shows hysteresis curves for two orientations of the films Ta(2)/Co(3)/Cu(**3.2**)/NiFe(5)/Ta(2) (a) easy axis and (b)hard axis. Also shown are (c) easy axis and (d) hard axis curves for Ta(2)/Co(3)/Cu(**2.4**)/NiFe(5)/Ta(2).

However, as the thickness decreases to 2.4 nm Cu spacer layer the independent switching of the two layers is difficult to observe. This can be related to the magneto-resistance of the same sample evidenced in Fig 4.14(d) where there is no plateau of resistance observed for the anti-parallel orientations of the magnetizations in the two layers.

When the thickness of the spacer layer is reduced further, it is much harder to observe independent switching events as can be seen from Fig 4.23.
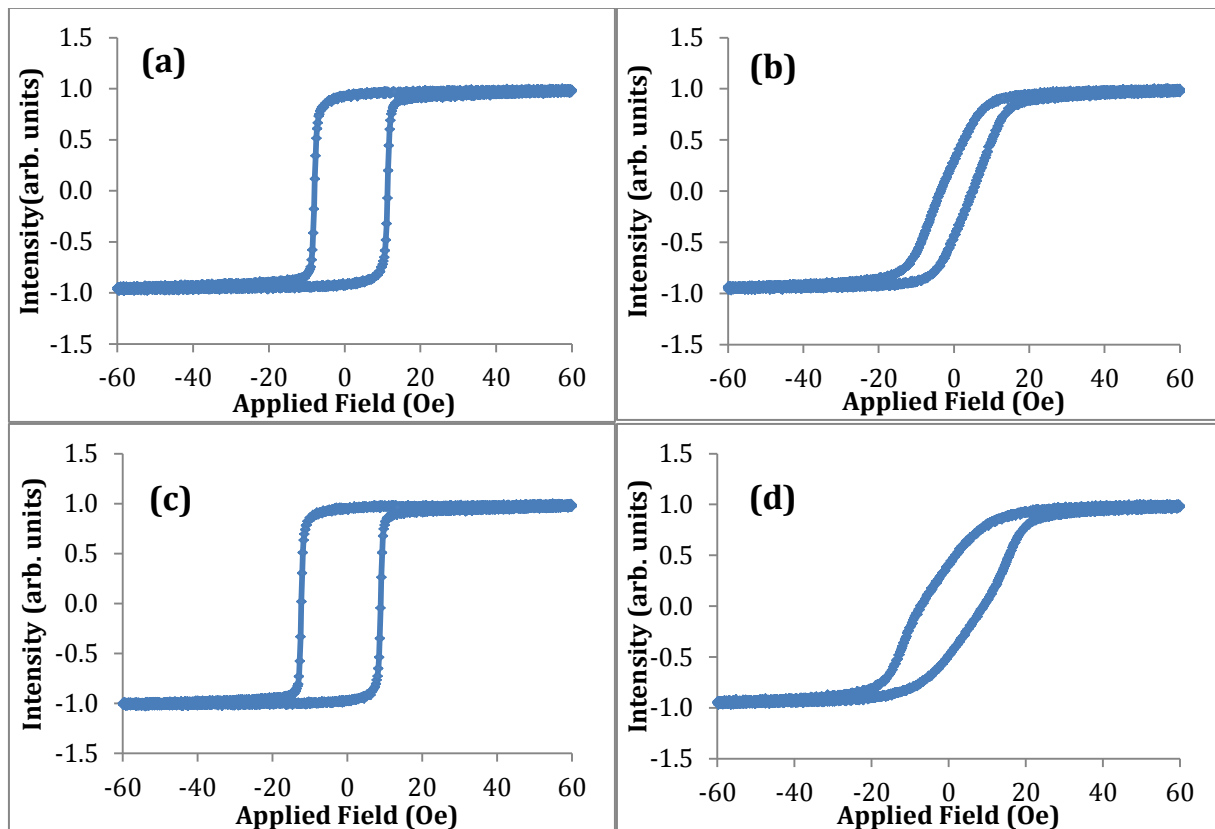
Figure4.23: Hysteresis curves for two orientations of the film Ta(2)/Co(3)/Cu(**1.8**)/NiFe(5)/Ta(2) in the (a)easy axis and (b) hard axis. Hysteresis curves for film Ta(2)/Co(3)/Cu(**1.6**)/NiFe(5)/Ta(2) in the (c) easy axis and for the (d) hard axis.

The hysteresis loops were measured for two orientations 1) field applied along the deposition field direction, easy axis and 2) field applied transverse to the deposition field direction, hard axis. Firstly it can be seen from the examples shown in Fig 4.23 that the hard axis hysteresis curve for different Cu spacer layer remains the same in field response. This demonstrates that field applied during

deposition is inducing an anisotropy along an axis and this is independent of the thickness of the Cu spacer layer. Further the coercive fields for spin-valves with different Cu thicknesses show an oscillatory behavior with respect to the thickness of the spacer layer. This can be seen from Fig 4.24 and could be attributed perhaps to the changing of the coupling strength between the free and pinned layers as the Cu spacer thickness is changed. Since each sample was measured at four different locations of the laser spot on the film plane the standard error was used to determine the error bars in Fig 4.24.
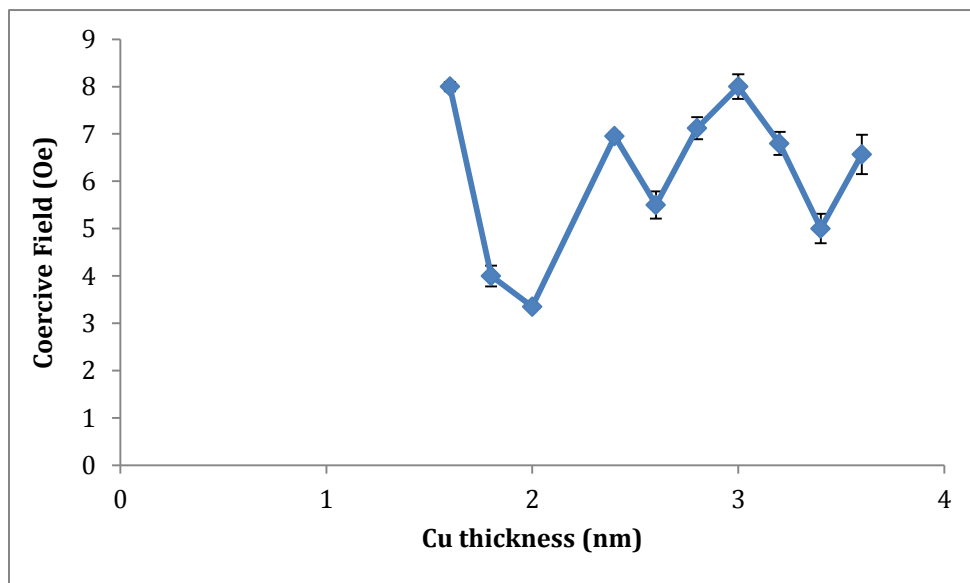
Figure4.24: Shows the variation of the magnetic coercivity as a function of the Cu spacer thickness **t** for 10x10 mm films along the hard axis. The film comprised of Ta(2)/Co(3)/Cu(**t**)/NiFe(5)/Ta(2) with nominal thicknesses given in nanometers.

For the thinnest Cu spacer layer of 1.6 nm shown in Fig 4.23(c) the magnetic response along the easy axis is very similar to a single layered FM material. For comparison the hysteresis for a single layer Co(3 nm) film with identical cap and seed layer is shown in Fig 4.25.

Figure4.25: Shows the hysteresis curve along the easy axis (measured along the axis of applied field during film growth) for a 10x10 mm Si/SiO$_2$/Ta(2)/Co(3)/Ta(2).

The Pseudo Spin-Valve with a Cu spacer layer of 1.6 nm does not show any visible independent switching events for the two FM layers. There could be 3 possible explanations 1) the spacer layer thickness is too small 2) dipolar coupling [10] and 3) orange-peel coupling (Néel) magnetostatic coupling [11] [12]. If the spacer layer thickness is too small this can result in discontinuous fi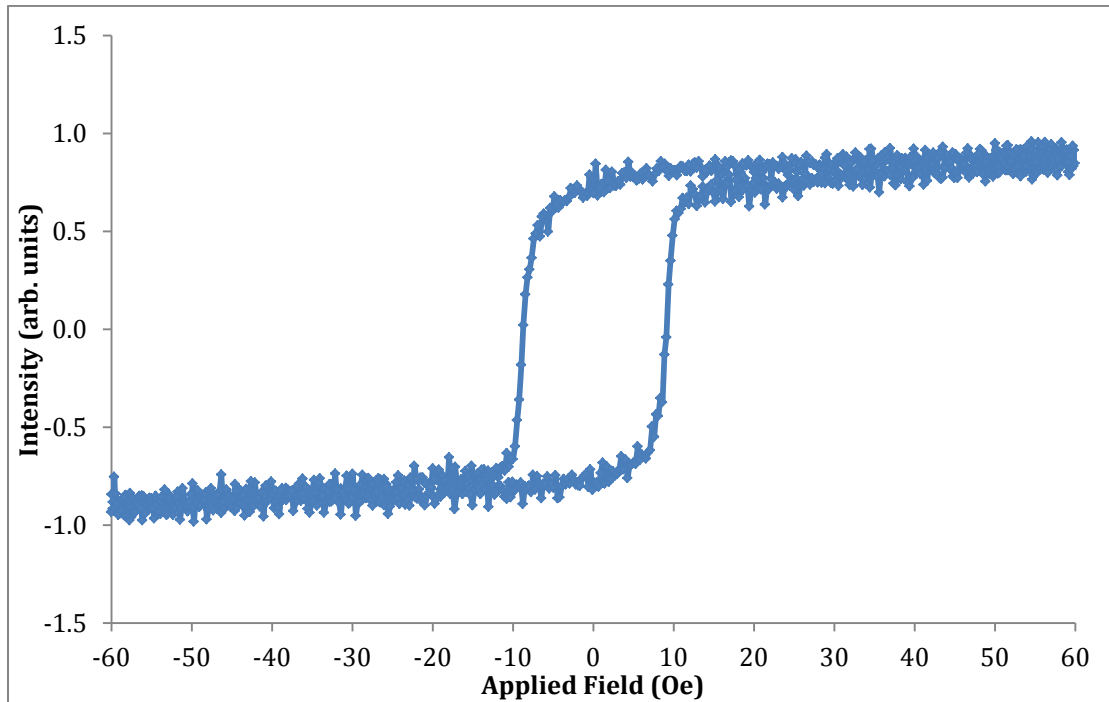lm growth which may lead to the formation of pin holes [9] through which the Co and the NiFe can couple via direct exchange coupling. Another possible reason for not observing any distinct switching of the two FM layers is that for small enough Cu thicknesses the stray fields generated by the cobalt layer could influence the NiFe and the two FM layers could be coupled via dipolar coupling. The third i.e. orange-peel coupling can arise due to correlated roughness at both interfaces and this becomes important when there is a very rough interface between two adjacent layers [13]. The two FM layers are coupled very strongly and essentially behave as a single FM entity thereby exhibiting a similar response compared to a cobalt thin film. When comparing the magnetization

with the transport properties for the 1.6 nm Cu thickness it is observed that the GMR for this thickness is low with respect to thicker Cu spaced spin-valves. The resulting lack of distinguishable switching for each FM layer is complemented by the lower GMR ratio obtained for the 1.6 nm Cu sample. Thicker spacer layer spin-valves, such the 3.6 nm thin film, exhibit two switching events a sharper switching occurring at lower fields and a more gradual reversal occurring at higher fields. By changing the thickness of Cu the hysteretic response of the high field magnetization reversal is altered, while the reversal at low fields remains relatively unchanged. This is indicative of the degree of coupling between the two FM layers. The linear response of the free layer reversal shown for all Cu thicknesses is indicative of coherent rotation which is not the case for the Co layer as evidenced by the non-linear dependence of magnetization on magnetic field.

4.3.3 Micro-wires

Microwires of the form described in section 3.2.4 were patterned using optical lithography and the magnetic hysteresis of these wires were studied. Using the laser MOKE set-up described in section 3.4 the laser spot was focused to 5 µm and fixed on different regions of the micro-wires. This allowed studying the magnetic response of each arm of the L-shaped micro-wire individually and at different angles with respect to the applied field. The micro-wires consisted of the entire GMR stack. Four separate wires were deposited with Cu thicknesses of 2, 3, 4 and 10 nm. It is important to note that these structures were deposited in the absence of any *in-situ* applied magnetic field. The L-shaped wires consisted of two arms. Each arm had the dimensions of 15 µmx100 µm and 25 µmx200 µm. Each wire had 3 Au contacts which were to be used to apply current to each arm individually and study magneto-resistance for different angles between applied current and field. Therefore, all four L-wires were on a single silicon wafer which was larger in 1 dimension than the maximum air gap between the magnetic pole pieces of the longitudinal MOKE set-up. Hence, the

wires weren't able to be rotated along different directions with respect to the field. The coercivity for both 15 μm wide and 25 μm wide wire are shown in Fig 4.26 for different Cu thicknesses.
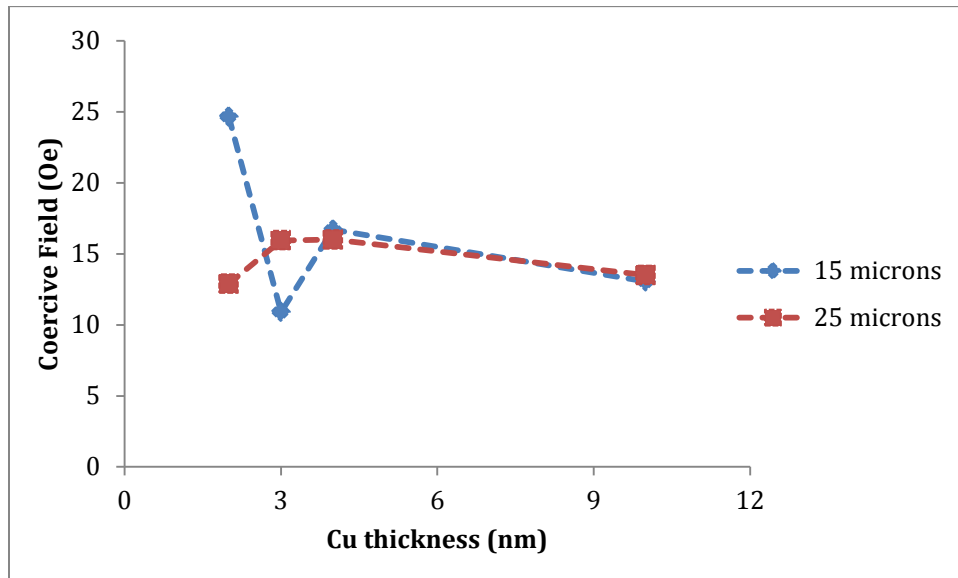
Figure4.26: Variation of the coercivity as a function of the Cu spacer layer thickness for two arms of the L-shaped microwire, 15 μm(blue) and the 25 μm(red).

It can be seen that the effect of Cu thickness for each microwire width is larger for lower Cu thickness. The coercive field for 2 nm nominal spacer layer thickness is larger for the 15 μm wire as compared to the 25 μm as shown in Fig 4.26. This could be due to the increase in edge roughness as the width of the wire decreases. The cumulative coercive field for reversal of both the fixed and the free layer is higher for the more narrow wire. However, when the spacer is increased to 10 nm nominal thickness the coercive fields for both the wires are approximately equal. The hysteretic response to field for both the 15 and 25 micron wire for 4 nm spacer layer thickness is shown in Fig 4.27. The hysteresis is very similar for other thicknesses with only differences in coercivity which has been highlighted in Fig 4.26.

One such hysteresis is shown for the 4 nm Cu spacer for both 15 µm and 25 µm wide wires from the two arms of the L-shaped structures.
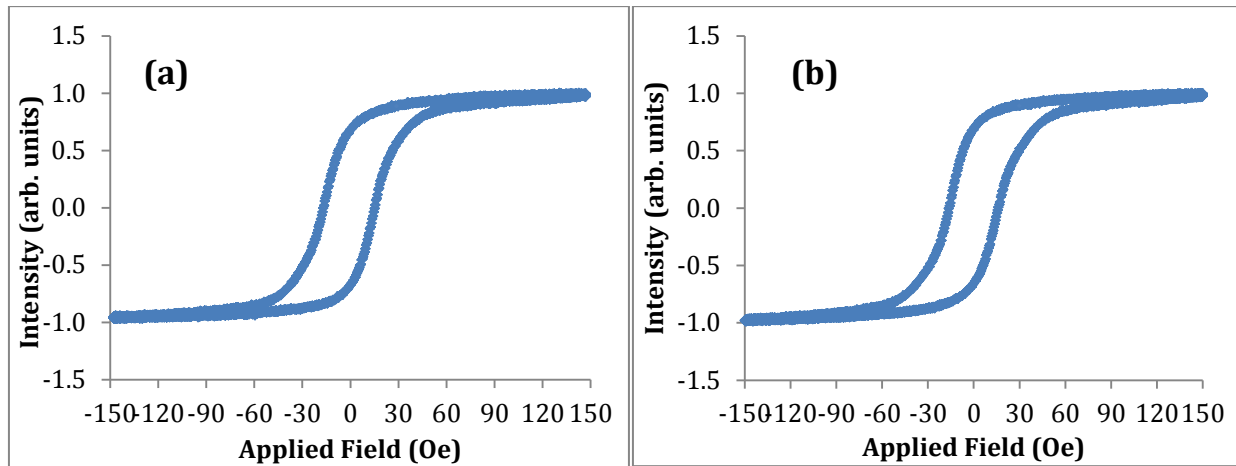
Figure4.27: Shows the magnetic hysteresis for Ta(2)/Co(3)/Cu(4)/NiFe(5)/Ta(2) L-shaped microwires with the MOKE spot focused on both the (a)15 µm and the (b)25 µm arm.

The field is applied at a 45° angle with respect to each wire. Due to there being no magnetic field applied during deposition in terms of energetics, the domain structure and magnetization would be dominated by shape anisotropy in continuous films. However, in patterned structures the stray fields and dipolar fields often result in anti-ferromagnetic alignment of the layers. Since there is no visible distinction in the switching behavior for each individual layer of the GMR stack the magnetization for both the magnetic layers is dominated by the shape anisotropy. The RKKY coupling is not strong enough to overcome the shape anisotropy energy.

In order to attain a deeper understanding of the magnetic properties it is important to structurally characterize the material systems, this is discussed in the following section.

4.4 X-ray Reflectivity

RKKY coupling is strongly dependent on the spacer layer thickness. The coupling strength as shown varies as $1/d^2$. Also with respect to transport properties each interface within the GMR stack, the Co/Cu and Cu/PY can contribute to interfacial scattering of the s electrons and add to net resistance of the stack. Thus it is important to understand the structural properties as these can have a direct influence on the electrical measurements.

X-Ray reflectivity was performed for different samples in order to confirm the thickness and estimate the roughness from each interface. This was done post deposition. X-Ray Reflectivity data was fitted using open source fitting software, GenX [14] which used a Parratt recursive formulism. The reflectivity measurement was done after careful alignment of the D1-X-ray system by removing sample tilt in any axis. A θ-2θ reflectivity curve was measured for the specular condition. Also, in order to obtain a more realistic interpretation of the reflectivity data, an off-axis reflectivity curve was also measured for each sample to obtain the off-specular reflections. This allowed for a better estimation of the background scattering which may occur during the measurement. The final curves which were used for fitting the material stacks was obtained by subtracting the off-specular reflection from the specular reflection to obtain the true reflectivity for each measured stack. Nominal thicknesses were used as initial starting points in the recursive algorithm. Tantalum penta-oxide was used as an oxide layer to model the oxide formation above the capping layer. It was shown that inserting Ta_2O_5 above the capping layer allowed for a better fit and a lower Figure Of Merit (FOM) (Fig 4.30). The FOM provides an estimate of the goodness of the fit [14] the lower the FOM is the closer the simulated reflectivity is to that of the measured data. The roughness was modelled as the inter-diffusion between two adjacent layers. Table 4.1 lists thickness and roughness for each layer along with nominal thickness of different samples obtained after fitting the

reflectivity data. The structural properties of the films detailed in Table 4.1 are for full films deposited in the presence of an *in-situ* in-plane applied magnetic field.

Sample ID	Material	Nominal Thickness(Å)	Fitted Thickness(Å)	Fitted Roughness(Å)
SPM2	Ta_Cap	20	15.54	6.62
	$Ni_{81}Fe_{19}$	50	54.02	11.30
	Cu	20	31.84	8.36
	Co	30	17.62	3.07
	Ta_Seed	20	18.97	6.66
SPM3	Ta_Cap	20	20.56	5.77
	$Ni_{81}Fe_{19}$	50	42.40	10.04
	Cu	15	25.81	4.13
	Co	30	26.12	3.18
	Ta_Seed	20	15.47	6.41
SPM4	Ta_Cap	20	18.29	5.81
	$Ni_{81}Fe_{19}$	50	34.30	11.04
	Cu	25	37.43	5.87
	Co	30	25.20	4.13
	Ta_Seed	20	15.20	9.02
SPM5	Ta_Cap	20	18.84	4.14
	$Ni_{81}Fe_{19}$	50	48.20	13.53
	Cu	30	42.46	8.31
	Co	30	26.61	8.62
	Ta_Seed	20	19.67	5.54
SPM6	Ta_Cap	20	15.89	5.19
	$Ni_{81}Fe_{19}$	50	51.63	13.79
	Cu	40	59.10	7.53
	Co	30	24.98	3.12
	Ta_Seed	20	17.98	7.31
SPM7	Ta_Cap	20	22.97	11.95
	$Ni_{81}Fe_{19}$	50	45.96	14.62
	Cu	100	148.88	8.01
	Co	30	23.29	3.40
	Ta_Seed	20	22.07	6.38

Table4.1: Shows a list of the material stacks detailing their measured thicknesses and roughness values obtained from the X-ray reflectivity shown in Fig 4.28 and Fig 4.29.

It is important to note that the nominal thicknesses are not exactly the same as obtained by the reflectivity fits. However, the relative difference between two film thickness is consistent. Also throughout the course of this study the Sputter system as described in 3.2.2 was in the process of being upgraded, which occasionally resulted in there being a difference in the sputter rates for certain targets. All efforts were made to keep the thicknesses as close to their nominal value as possible. The films on which the MR was measured as shown in section 4.2 were grown with the

same sputter rates for each target for each deposited film. However, it was not possible to obtain Reflectivity measurements on those samples due to the paucity of time.

From Table 4.1 it can be seen that the roughness of NiFe is relatively higher as compared to the other materials for a given stack. The increased roughness in the free layer may add to a reduced magneto-resistance ratio due to spin-flip events occurring at this interface.

The Reflectivity curves measured and fitted curves for the material stacks listed in Table 4.1 are shown in Fig 4.28 and Fig 4.29.
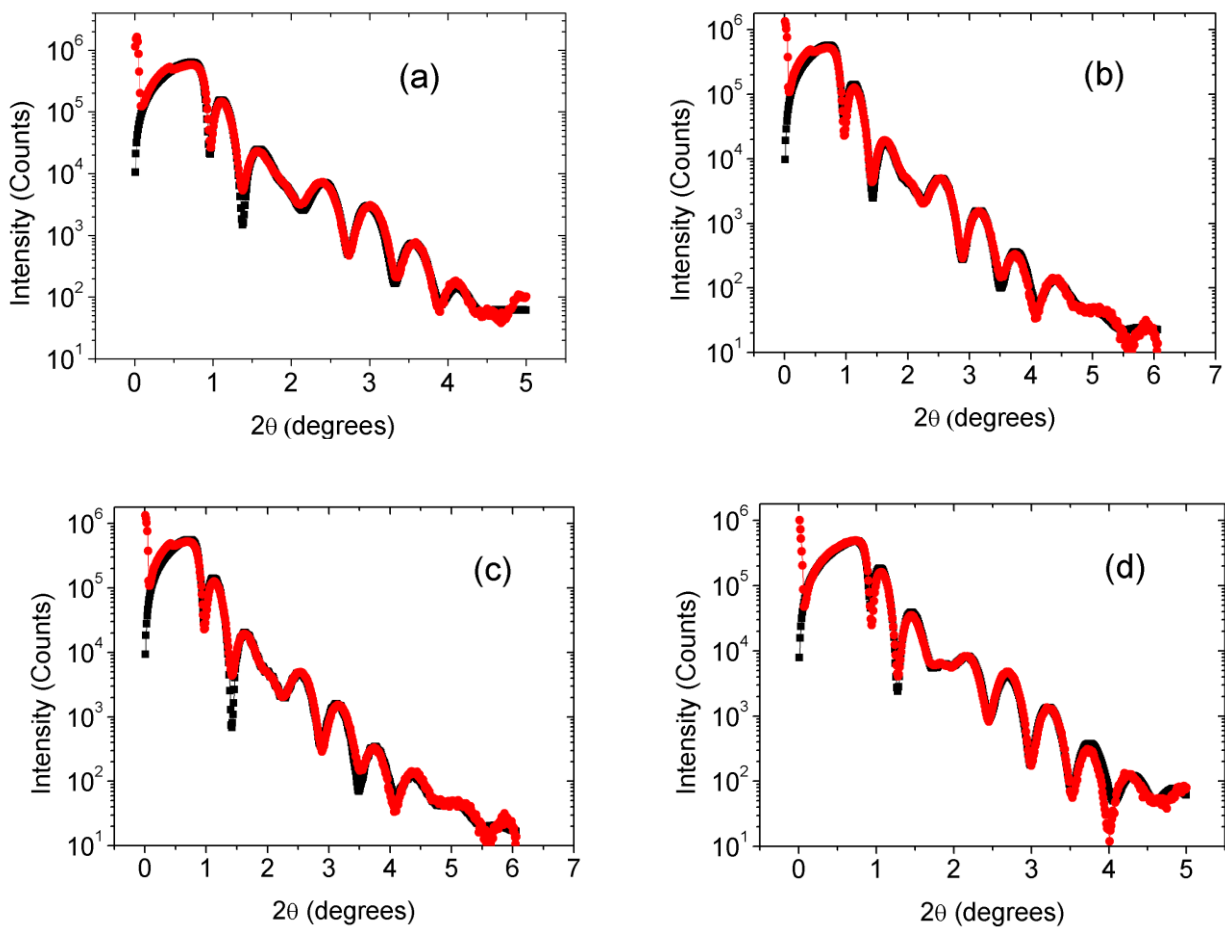

Figure4.28: Shows the measured reflectivity (Red) and the simulated reflectivity (Black) for Ta(2)/Co(3)/Cu(**t**)/NiFe(5)/Ta(2) where (a)t= Cu(2 nm) (b)t= Cu(1.5 nm) (c)t= Cu(2.5 nm) (d)t= Cu(3 nm)
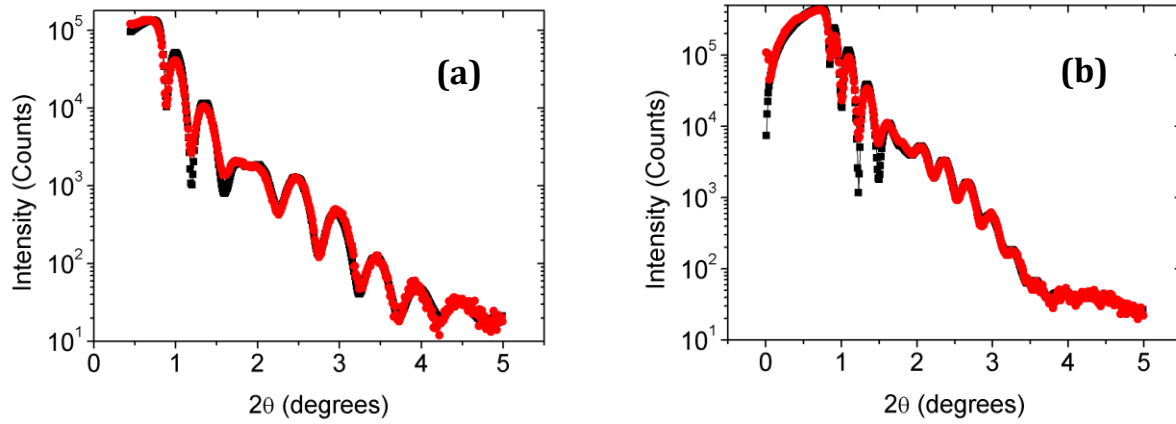
Figure4.29: Shows the measured reflectivity (Red) and the simulated reflectivity (Black) for Ta(2)/Co(3)/Cu(**t**)/NiFe(5)/Ta(2) where (a)t= Cu(4 nm) (b)t= Cu(10 nm)

Each reflectivity measurement was performed until the intensity count rate decreased to a value less than 10 counts per second.

In order to achieve a model that better represents the material stack a Ta_2O_5 layer was included in fitting model as shown in Fig 4.30.

Figure4.30: Shows the difference between the goodness of fit for a Ta(2)/Co(3)/Cu(**2.5**)/NiFe(5)/Ta(2) (a) without using an oxide layer and (b) using an oxide layer in the simulation of the reflectivity the Figure Of Merit are (a) 2.4147×10^{-1} and (b) 8.9099×10^{-2} .

It can be seen that for thin films without a Ta_2O_5 layer, the fit does not match the actual reflectivity data.

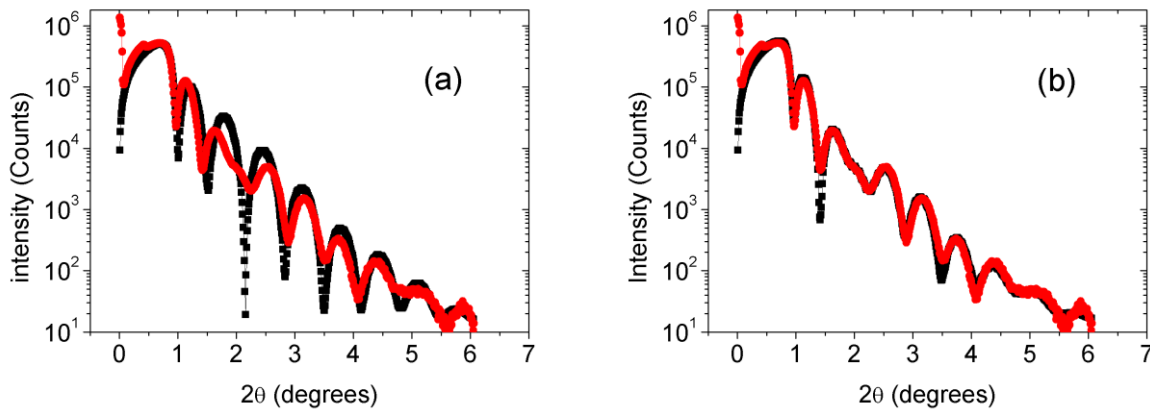XRR fitting revealed that the cobalt thickness was lower than what was estimated. The thickness of Co was approximately 2 nm. This is also the thickness about which Co undergoes a phase transition from fcc to hcp [15]. For most samples also the NiFe roughness was higher than the other layers. The entire stack was modelled including the 100 nm thermally oxidized Si and the silicon substrate. The Thompson scattering factors obtained from [16] are used to model the oscillation in intensity. The scaling of the intensity with respect to the incident angle is indicative of roughness for each layer. The background spectra was recorded and then subtracted from the measured spectra, to obtain the true specular reflection. It is worth noting here that the difference in scattering factors between Co and Cu is low. This results in difficultly in the precise determination of the interface using grazing angle X-ray reflectivity, as explained in [17].

The transport properties via the magnetoresistance measurements, the magnetisation dynamics via MOKE magnetometry and the structural characterization using X-ray reflectivity were measured and the results discussed within this chapter. Further investigations and device engineering could be performed which would allow more insights into the dynamics of the magnetization in the NiFe layer. However, this work was a time limited project and the measurements were performed in the given time frame.

The results of this work are concluded in the following chapter.

Chapter 4- References

[1] Parkin, S.S.P., *et al.,'Oscillatory magnetic exchange coupling through thin copper layers*' S. S. P. Parkin, Physical Review Letters, **66**, (1991), 2152

[2] Pizzini, S., *et al., 'Structural and magnetic properties of Cu/Co and Au/Co multilayers*' Journal of Magnetism and Magnetic Materials, **121**, (1993), 208-212

[3] Tumanski, S., '*Handbook of Magnetic Measurements',* Taylor and Francis, U.S.A (2011)

[4] McGuire, T.R., and Potter, R.I., '*Anisotropic magnetoresistance in ferromagnetic 3d alloys*', IEEE transactions on Magnetics, **11**, (1975), 1018-1040

[5] KATRINA, B. L., (2010) '*An Investigation of the Structure, Pinning and Magnetoresistance of Domain Walls in Ni81Fe19 Planar Nanowires*', Durham theses, Durham University. Available at Durham E-Theses Online: http://etheses.dur.ac.uk/507

[6] Parkin, S.S.P., '*Origin of Enhanced Magnetoresistance of Magnetic Multilayers: Spin-Dependent Scattering from Magnetic Interface* States', Physical Review Letters, **71**, (1993), 10

[7] Parkin, S.S.P., '*Systematic variation of the strength and oscillation period of indirect magnetic exchange coupling through the 3d, 4d, and 5d transition metals*', Physical Review Letters, **67**, (1991), 3598

[8] Bozorth, R. M., 'Ferromagnetism', Van Nostrand, London (1951)

[9] Newell, A.J., *et al.*, '*A generalization of the demagnetizing tensor for non uniform magnetisation*' Journal of Geophysical Research - Solid Earth, **98**, (1993), 9551-9555

[10] Thomson, W., '*On the electro-dynamic qualities of metals: effects of magnetisation on the electric conductivity of nickel and iron*' Proceedings of the Royal Society, **8**, (1857) 546-550

[11] Mott, N. F., '*The electrical conductivity of transition metals*', Proceedings of the Royal Society 153 (1936) 699-717

[12] Campbell, I. A., and Fert, A., 'Transport properties of ferromagnets' in 'Ferromagnetic materials' Vol. 3., Edited by Wohlfarth, E. P., North Holland Publishing Company, Amsterdam (1982)

[13] Armaki, M.M.S., (2012), '*Spin Valves and Spin-Torque Oscillators with Perpendicular Magnetic Anisotropy*',PhD thesis, KTH Information and Communication Technology, Sweden

[14] M. Björck and G. Andersson, '*GenX: an extensible X-ray reflectivity refinement program utilizing differential evolution*', Journal of Applied Crystallography, **40**, (2007), 1174

[15] Tokaç, M. *et al.,* '*Interfacial structural dependent spin mixing conductance in cobalt thin films'*, Physical Review Letters, **115**, (2015), 056601

[16] http://henke.lbl.gov/optical_constants/asf.html Accessed on 4th February 2016

[17] Hase, T. *et al., 'Determination of the Copper layer thickness in Spin Valves by Grazing Incidence X-ray Fluorescence'*, IEEE Transactions on Magnetics, **34**, (1998), 831-833

|Chapter 5

Conclusion

Pseudo spin-valves of the form FM/NM/FM were grown as full films and patterned micro-wire structures with the aim to devise a tool which may utilise both the Anisotropic Magneto-Resistance and the Giant Magneto-Resistance to study domain wall dynamics using the changes in the resistance. The difference in the Magneto-Resistive response for both phenomena was used as a basis for a device concept. For instance the AMR when current and magnetisation are parallel does not distinguish between 0° and 180° of magnetisation with respect to current angle as along as the magnetisation is collinear with current the saturated resistance value is identical. On the contrary however, the Giant Magneto-Resistance depends crucially on the relative directions of magnetisation between the two layers. The RKKY coupling between the two FM layers was changed to tune the GMR signal from the Pseudo Spin-Valve.

Two different ferromagnetic materials were used as a pseudo-pinned, and free layer namely cobalt and Permalloy respectively. These spin valves did not include an antiferromagnetic pinning layer (neither synthetic nor a metallic anti-ferromagnet) as is often the case in spin-valve systems used in memory applications [1]. The absence of this pinning layer prevented the bottom FM layer from

obtaining a completely pinned magnetic spin structure. This was done to prevent the system from achieving a magnetic configuration in which the transport properties are dominated by the GMR effect. In order to achieve the set goal it was crucial to 1) obtain the correct choice of materials and 2) to optimise the entire GMR material stack. Hence, with regard to the materials there are two different methods of producing a PSV structure, one method is using two ferromagnetic materials of different thickness [2], the second method is using two different ferromagnetic materials [3]. The latter approach was taken here with a harder Co layer used as the pseudo-pinned layer and the relatively softer layer NiFe used as the magnetic free layer in the PSV geometry. It has been shown that such a method of devising a PSV would give rise to a larger Magneto-Resistance [4][2]. The films were grown using a shadow mask which consisted of a stripe design with known dimensions of 3x18mm^2. This stripe was used to perform 4-point in line DC measurements in the presence of a directed magnetic field from which the Magneto-Resistance for each film was measured. Thin films of Subs/Ta/Co/Cu(t)/NiFe/Ta were grown using D.C sputtering. Ta was used as the seed and capping layer which was grown using R.F sputtering. The sputtering racetrack was more diffuse for the R.F. sputter power which provided for low deposition rates and a smoother surface of the Ta for a given pressure. The Cu thickness was varied from 1.5 nm to 10 nm while keeping the thickness of the remaining layers constant and the Magneto-Resistance of the entire material stack was measured. There was a range of different Magneto-Resistance responses recorded for differing Cu thicknesses. The resistance ranged from being dominated by either the AMR signal, the GMR signal or possess an intermediate state with a Magneto-Resistance occurring as a result of the combination of both the GMR and AMR effect.

It was found that the Magneto-Resistance response is very strongly dependent on the thickness of the spacer layer, in this case Cu. This is because the degree of indirect exchange coupling, which occurs between the two FM layers via the non-magnetic spacer layer depends on the thickness of the Cu spacer layer. As the Cu thickness is changed the relative magnetisation in each of the two FM

layers present on either side of the Cu layer tend to align preferentially anti-ferromagnetically. The Magneto-Resistance as a function of the Cu spacer layer was measured for the field and current applied parallel to each other. For the Cu thickness in which the MR is given by a combination of the AMR and the GMR signal it is easier to distinguish each magnetoresistive response arising from each phenomenon as compared with the thickness for which the signal is dominated by either Magneto-Resistance. This is possible because of the sign of the MR.

For the geometry in which current and field are parallel to each other the anisotropic contribution to the Magneto-Resistance exhibits a positive MR (increasing resistance with increasing fields) and the MR arising from the GMR effect has a negative MR response (which displays low resistance for high fields) due to saturation of the magnetisation for each layer. Therefore it is easier to distinguish between the individual resistance contributions, however for the geometry in which the current and field are perpendicular to each other this degeneracy of the MR response is not lifted and the two contributions will have an additive effect which proves more difficult to resolve. Varying the Cu thickness allowed the systematic study of the magnetic properties of the pseudo spin-valve thin films. In existing GMR sensors the difference in the relative switching fields of each layer is optimised. In this study, the material stack which exhibited the largest switching fields was the 1.5 nm Cu spaced thin film as shown in Fig 4.2 .It also showed a combination of both AMR and GMR phenomenon with sufficient anti-parallel coupling. Therefore, the optimised material stack which may be used as a device to study magnetisation dynamics using both AMR and GMR as a tool is the thin film pseudo spin valve with 1.5 nm Cu spacer and a nominal 3 nm and 5 nm pseudo pinned Co and free NiFe layer respectively.

The Magneto-Resistance shows an oscillatory behaviour with a period less than 1 nm for Cu as a spacer layer. This is comparable to that found by Parkin [5]. In order to confirm that the Magneto-Resistance does oscillate and that there is no aliasing within the system, full stacks of the GMR

structure was grown with a much smaller change in Cu thickness of 2 Å and the Magneto-Resistance was indeed shown to oscillate.

It was shown in this work that for certain thicknesses of Cu, in which there are contributions from both the AMR and the GMR that, the negative Magneto-Resistance actually arises from the Permalloy free layer rather than the relatively harder cobalt layer. This was measured experimentally by growing two separate films with only a single FM layer and the Magneto-Resistance measured for each film and compared to the complete GMR stack. Prior to designing a GMR based device the material growths for each layer in the GMR stack as well as the Magneto-Resistance had to be optimised and the individual contributions of the Magneto-Resistance measured and separated. The microwire design and structure was developed in this study which comprised of a three terminal L-shaped device which constituted of two arms of different widths with the possibility of current injection at three points along the L structure. The microwire was patterned using photolithography in collaboration with the Department of Engineering, University of Durham. However, due to an error in the process of the lithography the gold contacts were metallised prior to the deposition of the GMR material this led to strain in the structures as they were deposited on a thick 100 nm of Au contact pads. Nonetheless, magnetic characterisation was performed for these structures using the in-plane laser MOKE set-up.

In conclusion, pseudo spin valves of the form Subs/Co/Cu/NiFe were grown using magnetron sputtering. The Magneto-Resistance response exhibited by these structures ranged from AMR, GMR and to a combination of both AMR and GMR phenomenon. It was shown that the contribution of the AMR was largely due to the NiFe. A three terminal microstructure device was conceptualised, designed, patterned and measured which may be used for the study of domain wall dynamics.

5.1 Future work

The field of magneto-resistance phenomena is continuously growing; there exist magnetic tunnel junctions devices which have resonant tunnelling through an insulating barrier as the basis of their workings. It will be very interesting to study the magnetisation dynamics in the free layer of such tunnel junction. Also, magnetisation dynamics in the past few years has moved towards materials which possess a natural out of plane anisotropy [6] i.e. the magnetisation in the lowest energy state points out of the plane of the sample. Such materials have shown to exhibit very fast domain wall velocities [7]. It would be interesting to produce and study Perpendicular Magnetic Anisotropy (PMA) pseudo spin-valves and study the transport properties for such a system. Such systems typically contain a heavy metal and a FM sharing an interface, a phenomenon of SHE-STT (Spin-Hall Effect Spin Transfer Torque) also known as the SOT (Spin-Orbit Torque) [8] is under intense investigations by several groups currently. It will be useful to understand the effects of the different torques (STT and SOT) generated in the material system investigated in this study as this will ultimately have an impact on the magnetisation dynamics in the NiFe free layer. Perhaps an initial step towards that would be to study the out of plane AMR for systems showing PMA.

Finding new methods to study magnetisation dynamics in different systems is very interesting as there is new physics to be discovered which can hopefully lead to more efficient and more environmentally friendly technologies.

Chapter 5-References

[1] Leal, J.L., *et al.*, '*Spin valves exchanges biased by Co/Ru/Co synthetic antiferromagnets*', Journal of Applied Physics, **83**, (1998), 3720-3723

[2] Ono, T., *et al.,* '*Magnetization reversal in submicron magnetic wire studied by using giant magnetoresistance effect*', Applied Physics Letters, **72**, (1998), 9

[3] Shigeto, K., *et al.,* '*Injection of a magnetic domain wall into a submicron magnetic wire*', Applied Physics Letters, **75**, (1999), 18

[4] Castañol, F.J., *et al.,* '*Giant magnetoresistance in 60–150-nm-wide pseudo-spin-valve nanowires*', Applied Physics Letters, **81**, (2002), 15

[5] Parkin, S.S.P., *et al.,* '*Oscillatory magnetic exchange coupling through thin copper layers*', Physical Review Letters, **66**, (1991), 2152

[6] Ikeda, S., '*A perpendicular-anisotropy CoFeB–MgO magnetic tunnel junction*', Nature Materials, **9**, (2010)

[7] Yang,S.H., *et al.,* '*Domain-wall velocities of up to $750ms^{-1}$ driven by exchange-coupling torque in synthetic antiferromagnets* ', Nature Nanotechnology, **10**, (2015)

[8] Prenat, G., *et al.,* '*Beyond STT-MRAM, Spin Orbit Torque RAM SOT-MRAM for High Speed and High Reliability Applications*' Ch. 4, Spintronics-based Computing, Springer, 2015